eman ta zabal zazu

Universidad del País Vasco

Euskal Herriko Unibertsitatea

Characterization of hydrogen based superconductors from first principles

Francesco Belli

Date: 25/11/2022

Resumen

La superconductividad es un fenómeno caracterizado por la pérdida de resistencia dentro de un material. Esta propiedad hace que los materiales superconductores puedan reducir significativamente la pérdida de energía eléctrica en las redes de distribución y el uso de energía eléctrica, además de producir una reducción en el tamaño y peso de los componentes de potencia y maquinaria. Sin embargo, las temperaturas críticas superconductoras son bajas. Este hecho por sí solo dificulta su aplicabilidad práctica a gran escala debido a los desafíos y costes relacionados con el enfriamiento. El objetivo del campo de la superconductividad es intentar encontrar nuevos materiales que muestren superconductividad a alta temperatura y presión ambiental, y los superconductores actuales más útiles son los materiales cerámicos de cuprato-perovskita que exhiben superconductividad a aproximadamente 100 K.

En los últimos años, se han sintetizado superconductores convencionales ricos en hidrógeno en pequeñas muestras a alta presión mediante el uso de celdas de yunque de diamante. Esta configuración es capaz de generar presiones comparables con la del núcleo de la Tierra. En 2015 esta técnica permitió sintetizar el superconductor H_3S a 150 GPa exhibiendo superconductividad a 200 K y en 2019 el LaH_{10} a 170 GPa siendo superconductor a 250 K. Estos materiales representan una alternativa viable con respecto a las cerámicas de cuprato-perovskita, pero su aplicabilidad se ve obstaculizada por la alta presión que conduce a la imposibilidad de sintetizar muestras mayores de unas pocas micras.

Mientras tanto, también se invierte mucho esfuerzo a nivel teórico para predecir nuevos superconductores ricos en hidrógeno a través de métodos de predicción estructural basados en la teoría funcional de la densidad (DFT). A través de estos métodos, ahora hay cientos de superconductores basados en hidrógeno predichos. Además, la investigación sobre sistemas ricos en hidrógeno ahora se está desplazando hacia el intento de predecir sistemas con superconductividad a alta temperatura pero a presión ambiental.

Sin embargo, a pesar de los avances teóricos y las predicciones actuales, todavía falta una comprensión físico-química simple de las propiedades que mejoran las temperaturas críticas en los sistemas basados en hidrógeno. En otras palabras, aún no es posible confiar en variables simples para estimar las temperaturas de los superconductores y, en última instancia, diseñar químicamente mejores superconductores. En este sentido, los cientos de superconductores compuestos predichos a través de métodos de predicción estructural constituyen un rico conjunto de datos de trabajo para extraer conclusiones que podrían guiar el descubrimiento de nuevos superconductores.

Un problema adicional está relacionado con los métodos actuales empleados para realizar las simulaciones teóricas. En la mayoría de los cálculos basados en la teoría funcional de la densidad para superconductores basados en hidrógeno a alta presión, los iones del sistema se tratan como partículas clásicas. Sin embargo, para esta clase de sistemas, compuestos principalmente por átomos ligeros de hidrógeno, es importante tener en cuenta que la naturaleza cuántica de los iones no puede despreciarse y puede alterar significativamente las propiedades estructurales, fonónicas y superconductoras. La mayoría de los cálculos teóricos relacionados con la investigación de compuestos ricos en hidrógeno están incompletos sin la introducción de efectos cuánticos iónicos y conducen a predicciones inexactas, si no completamente erróneas.

En esta tesis, primero se realiza una investigación de las propiedades químicas, estructurales y electrónicas de un gran conjunto de superconductores binarios basados en hidrógeno, a través de métodos *ab initio* basados en teoría funcional de la densidad. Este análisis tiene como objetivo identificar correlaciones o huellas que podrían aclarar las características específicas que dan lugar a buenos superconductores. Como resultado, el análisis conduce a la identificación de un valor observable, el networking value, basado únicamente en la combinación de propiedades estructurales y electrónicas que exhibe una sorprendente correlación con la temperatura crítica superconductora. Los resultados obtenidos de este trabajo abren nuevas vías para el descubrimiento de nuevos sistemas ricos en hidrógeno. La introducción de códigos automatizados para el cálculo del networking value, combinados con métodos de predicción estructural, acelerará la predicción estructural al evitar el cálculo de las propiedades de los fonones de estos compuestos, y permitirá elegir con previsión para qué compuestos merece la pena profundizar en los cálculos computacionales.

En una ruta paralela, mediante el uso del método de Aproximación Armónica Autoconsistente Estocástica, se investiga el comportamiento de la estabilidad estructural para LaH_{10} y $LaBH_8$ con la inclusión de fluctuaciones iónicas cuánticas. Esto se hace para comprender cómo la estabilidad

de fase se ve afectada por la naturaleza cuántica de los átomos de hidrógeno ligero. Para LaH_{10}, los resultados obtenidos muestran que el paisaje de estabilidad de fase se simplifica y la estructura se sostiene a presiones mucho más bajas. En cambio, para $LaBH_8$, las fluctuaciones iónicas cuánticas desestabiliza la estructura a presiones mucho más altas. Estos resultados opuestos despertaron el interés de realizar un análisis adicional sobre el comportamiento de las fluctuaciones iónicas cuánticas en sistemas ricos en hidrógeno. En este sentido, se compararon todos los sistemas para los que se tuvieron en cuenta las fluctuaciones cuánticas con la Aproximación Armónica Autoconsistente Estocástica. Los resultados revelan que los efectos que tienen las fluctuaciones cuánticas en la estructura dependen en gran medida de las características específicas de los patrones de enlace interatómico. Por un lado, las fluctuaciones cuánticas sostienen a los superconductores basados en hidrógeno con patrones de enlace altamente simétricos, hasta presiones bajas y cercanas a la ambiental. Por otro lado, las fluctuaciones cuánticas introducen modificaciones estructurales en los sistemas a bajas presiones que pueden mejorar su interacción electrón-fonón y, en consecuencia, aumentar la temperatura crítica predicha a presión baja, si no ambiental. Los resultados arrojan esperanzas de encontrar superconductividad a alta temperatura y presión ambiental para sistemas ricos en hidrógeno.

Contents

CHAPTER 1

Introduction

As the modern world becomes more dependent on electricity, the necessity of electrical power sources and efficient distribution becomes increasingly important. The loss of electrical energy, due to resistance to flowing currents, translates into wasted energy and wasted economic resources, with a consequential negative impact on the environment. The phenomenon of superconductivity may offer a solution to such challenging issues. Superconductivity is characterised by the loss of resistance inside a material. Thus, the use of superconducting materials may significantly reduce the electrical energy loss in distribution networks and electrical power use, as well as producing a reduction in size and weight of power components and machinery. Additionally, the application for superconductivity are not limited to energy transmission. Superconductors may have relevant impact in plasma control on fusion energy production through the generation of strong magnetic fields [1]. They might have applications in energy storage due to the persistent currents enclosed superconducting loops [2], applications in low consumption transportation through levitating vehicles [3], as well as in quantum computing [4, 5].

Superconductors, however, come with many associated challenges. To start, a material has to satisfy a set of physical properties in order to be classified as superconductor. First, unlike ordinary conductors, whose resistance decreases gradually as its temperature is lowered, a superconductor has a characteristic critical temperature (T_c) below which the resistance drops abruptly to zero [6, 7]. Second, below the same critical temperature, there is a complete ejection of magnetic field from the interior of the super-

conductor. Such phenomenon is called the Meissner effect [8]. The first ever superconductor, found by the dutch physicist Heike Kamerlingh Onnes in 1911, was mercury (Hg) and exhibited a critical temperature of just about 4.2 K [9]. Such a small value for the critical temperature was foreshadowing the core issue related to practical applicability for superconductivity. Superconducting critical temperatures are low. This fact alone hinders their large scale practical applicability due to the challenges and costs related to cooling.

Since 1911, the goal of the field of superconductivity has been to attempt finding new materials in order to increase the superconducting critical temperatures. For about 65 years such values did not change much until, in 1986, it was discovered that some cuprate-perovskite ceramic materials exhibit critical temperatures above 90 K [10]. This represented a major breakthrough in the field due to the availability of cheap liquid nitrogen with a boiling temperature of 77 K. Thus, the existence of superconductivity at higher temperatures than liquid nitrogen facilitated its applicability in many experiments and applications that were less practical at lower temperatures.

On parallel routes, attempts were made to formulate a theory of superconductivity. The first theory of its microscopic behavior was developed in 1957 by John Bardeen, Leon Cooper and John Robert Schrieffer (BCS theory) [6]. However, even if the theory was able to justify the results for the low temperature superconductors, it was not able to justify the critical temperatures for the cuprate-perovskite ceramics, which, for this reason, became classified as "unconventional" superconductors. The BCS theory assumes the existence of an attractive force between pairs of electrons that is able to overcome the repulsive Coulomb interaction. This interaction becomes stable enough to bind the electrons together below the critical temperature, leading to the formation of a condensed state [11]. In this condition, the pair of electrons are free to move in the material without scattering and consequently without generating energy loss. In most of the cases for conventional superconductors, this attractive force is due to the interactions between electrons and ions [12]. However, accurate predictions for the appearance of the superconducting transition became possible only with the later appearance and refinement of the Migdal-Eliashberg theory [13]. Although based on the BCS theory, the advantage of the Migdal-Eliashberg formalism lies in the ability of describing the appearance of the superconducting state just through the properties of the normal electronic state.

Based on the specifics of the BCS theory, in 1968 Neil Ashcroft first suggested that pressurized hydrogen could exhibit superconductivity at high temperature due to the strong electron-ion interactions arising from

its high Debye temperature [14]. Later on, he expanded on his first proposal suggesting that the pressures required to achieve high superconductivity in hydrogen could be reduced by using other more heavy atoms as sort of chemical precompressors [15]. These suggestions did not have imminent implications considering the difficulty of performing experiments at high pressures and, exception made in 2001 for a the discovery of MgB_2 with T_c of 39 K [16], the critical temperature for conventional superconductors remained more or less the same for the coming few decades.

The ulterior breakthrough came when, with the advancement of high pressure experimental techniques, it became possible to synthesize materials at extremely high pressures through the use of diamond anvil cells (DAC) [17–21]. In this technique, a ceramic or metal gasket able to contain the sample is placed in between two opposing diamonds. By compressing the diamonds, it is then possible to generate pressures up to thousands of gigapascals in an area of several microns. Considering the diamond is optically transparent, X-ray scattering methods can be employed to study the structural properties of the sample and, with the addition of an electrode system in the diamond, it is also possible to measure the behavior of electrical signals.

In 2015 this technique allowed to synthesize the superconducting H_3S at 150 GPa exhibiting a critical temperature of 200 K [22]. For comparison, the pressure of the core of the Earth is about 300 GPa. This result ignited hope in the possibility of room temperature superconductivity and, soon enough, additional experiments in 2019 were able to synthesize the LaH_{10} compound at 170 GPa with T_c of 250 K [23, 24]. These results ignited faith in this class of hydrogen rich superconductors and confirmed the suspects first brought forward by Neil Ashcroft about the potential of pressurized hydrogen. Room temperature superconductivity is now almost at hand. The issue, however, is that the extremely high pressures needed for the stability of these systems lead to the impossibility of synthesizing samples bigger than few microns. Still then, the practical applicability of superconductivity on large scale remains elusive.

In the meanwhile, the experimental advancements where accompanied by a strong development of theoretical tools. The refinement of the density functional theory (DFT) [25], co-occurring with the exponential increment of the available computational resources, led to the development of structural prediction methods [26–29]. These tools brought the possibility of accurate investigations of atomic composition phase diagrams and made so that theoretical works assumed a more active role. At this point in time, simulations are not only able to correctly reproduce results for conventional BCS superconductors, but they are also able to make accurate predictions for new superconductors to better orient experimental efforts. This was

indeed the case for H_3S [30, 31], LaH_{10}[32, 33] and YH_6[32, 34], where theoretical works where able to suggest and predict the stability of the superconducting phases and the value of the T_c's. Currently in fact, the phase diagrams for almost all binary hydrogen rich H-X compositions, where H stands for hydrogen and X represents any element in the periodic table, have been explored in search for new superconductors. Among these predictions, the highest T_c values are 300 K for pure metallic hydrogen [35] and 326 K for the YH_{10} binary compound [36]. The combination of all the experimental and theoretical developments place hydrogen rich systems as the most promising candidates for the pursuit of commercial superconductivity despite their current drawbacks.

The research on hydrogen rich systems is now shifting towards reducing their pressure of stability. In recent years, attempts have been made to explore the energy landscape of ternary and quaternary hydrides [37–41] to further expand the list of predicted compounds. The most prominent result is for the possible metastability of $LaBH_8$ with a remarkable T_c of approximately 120 K [42, 43]. This compound was found to be stable against decomposition above 115 GPa and maintained dynamical stability down to 40 GPa. The same structural motifs of $LaBH_8$, with similar critical temperatures, have also been recently predicted for $BaSiH_8$ and $SrSiH_8$ [41]. This latter result brings hope that, with the right ternary or quaternary combination of atoms, it is possible to synthesize phases at high pressures that could remain metastable down to room pressure.

Despite the current theoretical advancements however, a simple physical-chemical understanding of the properties enhancing the critical temperatures in hydrogen based systems is still lacking. This creates an obstacle toward the discovery of new compounds with high T_c at low pressures. Contrarily to what was proposed by Neil Ashcroft in fact, having a high Debye temperature was shown not to be a guarantee by itself of high-temperature superconductivity. The results observed throughout the years have shown that critical temperatures in hydrogen rich systems can vary from few Kelvin, as for example for Th_4H_{15} [44], PdH [45], PrH_9[46], and AlH_3 [47], to almost room temperature as in the case for H_3S [22], YH_9 [48], YH_6 [49], and LaH_{10} [23, 24]. In this regard, the hundreds of compounds predicted to be superconductors through structural prediction methods constitute a rich working dataset to extract conclusions going beyond the idea of the high Debye temperature as a marker for high T_c [19, 50, 51]. Aiming at extracting useful information from this dataset, machine learning methods [52–55] are starting to be employed to further increase the list of predicted systems, while also attempting to classify these superconductors using simple footprints based on structural, chemical, and electronic properties [19, 53, 56]. These studies suggest hydrogen rich systems with

highly symmetrical structures and high density of states (DOS) at the Fermi level are the best candidates for high-temperature superconductivity. Even if these properties are able to suggest good trends, they serve necessary but not sufficient conditions. This ultimately means there are not yet good known optimizers: improving these parameters will not necessarily lead to an improvement of the superconducting critical temperatures. In other words, it is not yet possible to rely on simple variables to estimate the superconducting temperatures, and, ultimately, chemically engineer better superconductors.

An additional issue is related to the current methods employed to perform the theoretical simulations. In most of the DFT-based calculations for hydrogen-based superconductors at high pressure, the ions in the system are treated as classical particles. For this class of systems however, composed mainly of light hydrogen atoms, it is important to have in mind that the quantum nature of the ions cannot be neglected and can significantly alter the structural, phononic, and superconducting properties. For example, in the high pressure phases of H_2O [57, 58], quantum ionic fluctuations symmetrise the hydrogen bond and reduce the boundary between asymmetric and symmetric structures in the phase diagram by 30 gigapascals [59]. Another example is the strong renormalization in the phonon spectra of PdH [60] introduced by the quantum treatment of the atoms. These results suggest that most of the theoretical calculations related to the investigation of hydrogen rich compounds might be incomplete without the introduction of ionic quantum effects and might lead to inaccurate, if not completely wrong, predictions.

This thesis reports a theoretical-computational work on hydrogen rich systems performed in an attempt to tackle the issues mentioned in the previous paragraphs. First, an investigation of the chemical, structural, and electronic properties for large set of hydrogen-based binary H-X superconductors, previously predicted in the literature [50], is performed through *ab initio* methods based on DFT. This analysis aims at identifying correlations or footprints that could clarify the specific features giving rise to good superconductors. As a result the analysis leads to the identification of an observable based solely on the combination of structural and electronic properties that exhibits an astonishing correlation with the superconducting critical temperature. On a parallel route, through the use of the Stochastic Self Consistent Harmonic Approximation (SSCHA) method [61–64], the behavior of the structural stability for LaH_{10} and $LaBH_8$ is investigated with the inclusion of quantum ionic fluctuations. This is done in order to understand how the phase stability is affected by the quantum nature of the light hydrogen atoms. For LaH_{10}, the obtained results show that the landscape of phase stability is simplified and the structure is sustained

to much lower pressures. For $LaBH_8$ instead, quantum ionic fluctuations destabilize the structure to much higher pressures. These opposite results sparked the interest to perform an additional analysis regarding the behavior of quantum ionic fluctuations on hydrogen rich systems. In this regard, all systems for which quantum fluctuations were taken into account with the SSCHA were compared. The results reveal the effects that quantum fluctuations have on the structure are strongly dependent on the specifics of the interatomic bonding patterns.

The thesis is organized in three parts as follows. In Part I the theory required to perform the analysis listed above is exposed. The part includes the basic of condensed matter physics, the density functional theory, the methods for the calculation of phonons and the electron-phonon interaction, the stochastic self consistent harmonic approximation, and the BCS and Migdal-Eliashberg theories of superconductivity. Part II exposes the analysis regarding the chemical, structural, and electronic properties for the large set of theoretically predicted superconductors. Here, a classification based on chemical bonding markers is introduced and is then used in conjunction with the electronic properties of these systems to identify relevant correlations with the superconducting critical temperature. Finally Part III exposes the results for the phase stability in presence of quantum ionic fluctuations for LaH_{10} and $LaBH_8$, and reports the analysis related to the behavior of quantum fluctuations for all systems investigated through the SSCHA.

I

Theoretical Methods

CHAPTER 2

Basics of condensed matter physics

The chapter discusses the basic concepts and approximations of condensed matter physics used throughout this work. The chapter starts from the basics of the many body Hamiltonian and the Born-Oppenheimer approximation, and continues with the discussion of the methods to treat the electronic problem through density functional theory. Furthermore, the chapter discusses the Hartree-Fock approximation in preparation for the derivation of the electron localization function. This latter tool proved to be instrumental for the analysis of the results that will follow in the next chapters.

2.1 The many body Hamiltonian

The building blocks of the systems described in condensed matter physics are nuclei a, with mass M_a, atomic number Z_a and charge eZ_a, and the electrons i, with mass m_e, charge $-e$, and spin $\hat{s} = \frac{\hbar}{2}\hat{\sigma}$, where $\hat{\sigma}$ expresses the Pauli matrices. Both nuclei and electrons are moving objects and, considering their quantum mechanical properties, their respective position $\mathbf{R}_a$ and $\mathbf{r}_i$ are to be intended as canonical position operators, while their momentum can be described as $\mathbf{P}_a = -i\hbar\nabla_{\mathbf{R}_a}$ and $\mathbf{p}_i = -i\hbar\nabla_{\mathbf{r}_i}$, respectively. In this specific notation, the bold symbols and letters represent vectors.

An accurate description for a general system and its properties, such as the absorption spectra of a molecule or superconductivity in a crystal,

can then be obtained by accounting for all its basic building blocks and their interactions through Coulomb forces. Such forces include the electronic interaction ($V_{e,e}$), the nuclear interaction ($V_{n,n}$), and the interaction between electrons and nuclei ($V_{e,n}$). The combination of these quantities with the nuclei and electron kinetic energies (T_n and T_e) generates a resulting Hamiltonian that is able to describe a system in its most general form:

$$H = T_e + V_{e,n} + V_{e,e} + V_{n,n} + T_n. \tag{2.1}$$

In a less compact expression, the Hamiltonian can be rewritten as

$$H = -\sum_i \frac{1}{2}\frac{\hbar^2 \boldsymbol{\nabla}_i^2}{m_e} - \sum_{i,a} \frac{1}{4\pi\epsilon_0}\frac{e^2 Z_a}{|\,\mathbf{r}_i - \mathbf{R}_a\,|} + \frac{1}{2}\sum_{\substack{i,j \\ i\neq j}} \frac{1}{4\pi\epsilon_0}\frac{e^2}{|\,\mathbf{r}_i - \mathbf{r}_j\,|} + \frac{1}{2}\sum_{\substack{a,b \\ a\neq b}} \frac{1}{4\pi\epsilon_0}\frac{e^2 Z_a Z_b}{|\,\mathbf{R}_a - \mathbf{R}_b\,|} - \sum_a \frac{1}{2}\frac{\hbar^2 \boldsymbol{\nabla}_a^2}{M_a}, \tag{2.2}$$

where ϵ_0 is the permittivity of vacuum. To obtain a concrete solution to the Hamiltonian problem of equation (2.2) it is necessary to solve the Schrödinger equation with the introduction of a wave function ($|\chi\rangle$) containing the probability amplitude for each configuration of the constituent particles. This wave function must account for all the nuclei (N_n) and the associated electrons (N_e)

$$\langle \mathbf{r}, \mathbf{R} | \chi \rangle = \chi(\mathbf{r}_1, \mathbf{r}_2, ...\mathbf{r}_{N_e}, \mathbf{R}_1, \mathbf{R}_2, ...\mathbf{R}_{N_n}), \tag{2.3}$$

so that the Schrödinger problem can be formulated as

$$H\,|\chi\rangle = E\,|\chi\rangle. \tag{2.4}$$

In this notation $\mathbf{R}$ and $\mathbf{r}$ denote the ensemble of all nuclear and electronic coordinates so that $\mathbf{R} \equiv \{\mathbf{R}_1, \mathbf{R}_2, ...\mathbf{R}_{N_n}\}$ and $\mathbf{r} \equiv \{\mathbf{r}_1, \mathbf{r}_2, ...\mathbf{r}_{N_e}\}$.

Even if it appears conceptually simple, an exact *"ab-initio"* solution of the Schrödinger equation for the Hamiltonian (2.2) is far from being possible. The presence of the electron-electron, electron-nuclei, and nuclei-nuclei interactions makes impossible to split the Hamiltonian into different single particle sub Hamiltonians. For example, to describe a small sample of 1 mm^3 of solid matter, it is in theory necessary to compute all the interactions for each of the basic constituents present in the system and, in this case, one is expected to find a number of constituents of the order of 10^{20}. It is clear at this point that in the current state of the art there is no brain or machine able to tackle the size of this problem, and that simplifications are necessary in order to advance in the quest for a solution to the many body problem.

2.2 THE BORN-OPPENHEIMER APPROXIMATION

The first big step toward an actual solution for the Hamiltonian (2.2) can be made by considering the scale of the nuclei dynamics with respect to the one of electrons. For instance, the mass of an electron is just about 0.0005% the mass of a hydrogen nucleus. It is therefore reasonable to expect that the timescale for phenomena and interactions for electrons and nuclei are very far apart. In practical terms, for an insulating system the electronic energy gap is of the order of 1 eV suggesting that the timescale for an electronic excitation is of the order of 10^{-14} s. Instead, the frequency of an average phonon vibration is of the order of 10 meV and therefore on a timescale of 10^{-12} s. On such a different scale, the nuclei can, for all purposes of description, be treated as interacting only with the average electronic cloud, while the electrons see the nuclei as frozen particles in space during their dynamics [65, 66].

A similar concept holds for metallic systems as well. For these systems no electronic band gap is present. This means that the electronic excitations can be small in energy and comparable with the nuclei dynamics in time. However, in metals non-adiabaticity is governed by the ratio between the characteristic phonon frequency and the energy of the highest energetic electron, the Fermi energy (ϵ_F). Considering an electron gas model, at low temperature the thermal energy is usually lower than the Fermi energy and therefore the resulting excitations are small and still close to the Fermi energy. Most of the properties of a metal are then little affected by neglecting these kind of contributions due to the motion of the metal electrons [67].

With these considerations in mind, it is reasonable to consider that equation (2.2) can be split so to have a part of the Hamiltonian related solely to the dynamics of the electrons obtained by neglecting the nuclear kinetic energy (T_n). After finding a reasonable solution for the latter, it is possible to reintroduce the nuclear kinetic term and solve the remaining dynamics for the nuclei. To practically derive this concept, it is useful to start by separating equation (2.2) as

$$H = H_e + T_n, \tag{2.5}$$

where H_e is the electronic Hamiltonian containing the terms T_e, V_{ee}, V_{en} and V_{nn}. Supposing that H_e has K number of electronic wave functions $\psi_k(\mathbf{r};\mathbf{R})$ as solution, it is possible to write its associated Schrödinger equation as

$$H_e \left|\psi_k(\mathbf{R})\right\rangle = E_k(\mathbf{R}) \left|\psi_k(\mathbf{R})\right\rangle. \tag{2.6}$$

In this equation, the general nuclei positions $\mathbf{R}$ enters just as a parametric dependence. By expressing the general wave function of the system

$\chi(\mathbf{r},\mathbf{R})$ through an expansion in terms of $\psi_k(\mathbf{r};\mathbf{R})$ and a set of nuclear wave functions $\phi_{k\alpha}(\mathbf{R})$ as

$$|\chi_{k\alpha}\rangle = \left|\psi_k(\mathbf{R})\right\rangle\left|\phi_{k\alpha}\right\rangle, \tag{2.7}$$

it is possible to write both the electronic Hamiltonian (H_e) and the nuclear kinetic term (T_n) as

$$H_e(\mathbf{R})_{k'k} = \left\langle\psi_{k'}(\mathbf{R})\right| H_e \left|\psi_k(\mathbf{R})\right\rangle_e = \delta_{k'k}E_k(\mathbf{R}), \tag{2.8}$$

and

$$T_n(\mathbf{R})_{k'k} = \delta_{k'k}T_n - \sum_{a,\gamma}\frac{1}{M_a}\left\langle\psi_{k'}(\mathbf{R})\right| P_{a\gamma}\left|\psi_k(\mathbf{R})\right\rangle_e P_{a\gamma} + \left\langle\psi_{k'}(\mathbf{R})\right| T_n \left|\psi_k(\mathbf{R})\right\rangle_e. \tag{2.9}$$

In the second equation, the index γ refers to the Cartesian components of the nuclear momentum operator $\mathbf{P}_a$, while the notation $\langle|\rangle_e$ denotes an integral performed only on the electronic degrees of freedom.

In this form, while the application of $\psi_k(\mathbf{r};\mathbf{R})$ over H_e is diagonal, its application over T_n is not. This shows why the electronic and nuclear degrees of freedom cannot generally be separated and in this case one is tasked to solve a system of $K\times K$ coupled equations. However, by expanding the second term of the right side of the second equation as

$$\langle\psi_{k'}(\mathbf{R}) \mid P_{a\gamma} \mid \psi_k(\mathbf{R})\rangle = \frac{\langle\psi_{k'}(\mathbf{R}) \mid \left[P_{a\gamma}, H_e\right] \mid \psi_k(\mathbf{R})\rangle}{E_k(\mathbf{R}) - E_{k'}(\mathbf{R})}, \tag{2.10}$$

it can be seen that whenever $E_k(\mathbf{R}) - E_{k'}(\mathbf{R})$ is large, or, more precisely, when the electronic bands are not degenerate and far apart, the second and third terms in the right side of equation (2.9) are small and, therefore, negligible. When this is possible, the operator $T_n(\mathbf{R})$ can be consider diagonal and it is reasonable to first solve the electronic problem as in equation (2.6). This means that once a solution for the electronic energies $E_k(\mathbf{R})$ is obtained, the nuclei equation can be solved as

$$\left[T_n + E_k(\mathbf{R})\right]\left|\phi_{k\alpha}\right\rangle = E_{k\alpha}\left|\phi_{k\alpha}\right\rangle. \tag{2.11}$$

Here $E_{k\alpha}$ represents the α eigenvalue for the energy curve with excited electrons k. Usually, equation (2.11) is solved considering the electronic problem to be in its ground state $\psi_0(\mathbf{r};\mathbf{R})$, associated to the eigenenergy $E_0(\mathbf{R}) = V(\mathbf{R})$, that minimises equation (2.8). In this case, the equation for the ground state has the form

$$\left[T_n + V(\mathbf{R})\right]\left|\phi_\alpha\right\rangle = E_\alpha\left|\phi_\alpha\right\rangle, \tag{2.12}$$

For metals, however, as it was mentioned before, this approximation holds when the characteristic phonon frequencies are small compared to the Fermi energy. For some systems this might not be the case and the average phonon frequencies can become quite high. In this case the approximation made here does not hold and additional interactions between electrons and nuclei become relevant. This situation will be studied in the next chapters.

2.3 THE HARTREE-FOCK APPROXIMATION

In the previous section the conditions for which it is possible to properly disentangle the nuclear wave function $\phi_{k\alpha}(\mathbf{R})$ from the electronic wave function $\psi_k(\mathbf{r};\mathbf{R})$ were shown. In this section, further approximations used for the electronic wave function alone discussed are instead. Generally speaking, solving the electronic problem is far from being simple. The wave function $\psi_k(\mathbf{r};\mathbf{R})$ contains all the information for the N_e electrons inside the system and takes into account all their interactions through the Coulomb electron-electron potential. This latter term adds an incredible complexity to the structure of the wave function, and makes each electron depend on all the others. As before, some approximations are needed in order to reach a practical solution. Usually, the state which is of most interest among all the electronic states is the one related to the lowest energy level ($V(\mathbf{R})$), the ground state. In order calculate the ground state, the main idea behind the approximations that will follow is to find a solution to the electronic problem by first neglecting the Coulomb electron-electron interaction. The latter can then be reintroduced with the hope it will not alter significantly the behavior of the system.

To work toward this approximation, it is worth considering that the general electronic Hamiltonian H_e can be separated in a part containing only single electron terms (H_i^{1e}), and a part containing the two-body electronic interaction (H_{ij}^{2e}) as

$$H_e = \sum_i H_i^{(1e)} + \sum_{\substack{i,j \\ i\neq j}} H_{ij}^{(2e)}. \tag{2.13}$$

More in detail the two terms of H_e can be written as

$$H_i^{(1e)} = -\frac{\hbar^2 \boldsymbol{\nabla}_i^2}{2m_e} - \sum_a \frac{1}{4\pi\epsilon_0} \frac{e^2 Z_a}{|\,\mathbf{r}_i - \mathbf{R}_a\,|} + \frac{1}{2} \sum_{\substack{a,b \\ a\neq b}} \frac{1}{4\pi\epsilon_0} \frac{e^2 Z_a Z_b}{|\,\mathbf{R}_a - \mathbf{R}_b\,|}, \tag{2.14}$$

and

$$H_{ij}^{(2e)} = \frac{1}{8\pi\epsilon_0} \frac{e^2}{|\,\mathbf{r}_i - \mathbf{r}_j\,|}. \tag{2.15}$$

In the equation for H_i^{1e}, the nuclei-nuclei interaction can be neglected as it contributes just as a constant. Furthermore, to obtain a solution for this one electron Hamiltonian it is necessary to define a basis for single particle states $\left\{\left|\bar{b}\right\rangle\right\}_b$ for both spacial wave functions and spin. The presence of the spin is denoted by the bar on top of the b state. With this basis, it results that the one electron Hamiltonian obeys the following Schrödinger equation

$$\hat{H}_i^{1e}\left|\bar{b}_a\right\rangle_i = E_i^{b_a}\left|\bar{b}_a\right\rangle_i, \tag{2.16}$$

where E_i^b is the energy E of particle ith related to the state $\bar{b}_a$. It is also important to remember that, in order to describe the complete electronic state, it is necessary to first of all include the indistinguishable nature of the electronic particles. This can be done by combining the single-particle states through a tensorial product containing all the one electron states $\left\{\left|\bar{b}_1\right\rangle_1 \otimes \left|\bar{b}_2\right\rangle_2 \ldots \otimes \left|\bar{b}_{N_e}\right\rangle_{N_e}\right\}_{b_1 \ldots b_{N_e}}$. Furthermore, the states need to be combined so that the resulting function respects the fermionic nature of the electronic states. The best way to achieve this is through the introduction of the Slater determinant. This is a linear combination of general states built on top of permutations of single particle states of the form

$$\left|SD(\bar{b}_1, \bar{b}_2, \ldots \bar{b}_{N_e})\right\rangle = \frac{1}{\sqrt{N_e!}} \begin{vmatrix} \left|\bar{b}_1\right\rangle_1 & \ldots & \left|\bar{b}_{N_e}\right\rangle_1 \\ \left|\bar{b}_1\right\rangle_2 & \ldots & \left|\bar{b}_{N_e}\right\rangle_2 \\ \vdots & \ddots & \vdots \\ \left|\bar{b}_1\right\rangle_{N_e} & \ldots & \left|\bar{b}_{N_e}\right\rangle_{N_e} \end{vmatrix}. \tag{2.17}$$

By applying the Slater determinant over the sum of all the single particle Hamiltonians one obtains

$$\sum_i H_i^{(1e)} \mid SD(\bar{b}_1, \bar{b}_2, \ldots \bar{b}_{N_e})\rangle = E^{(1e)}_{\{\bar{b}_1, \bar{b}_2, \ldots \bar{b}_{N_e}\}} \mid SD(\bar{b}_1, \bar{b}_2, \ldots \bar{b}_{N_e})\rangle, \tag{2.18}$$

where $E^{(1e)}_{\{\bar{b}_1, \bar{b}_2, \ldots \bar{b}_{N_e}\}}$ is expressed as the sum of all the single particle energies $\sum_i E_i^{b_a}$.

To continue towards a solution for the electronic problem, it is then possible to reintroduce the two electron Hamiltonian (H_{ij}^{2e}) and look for a specific Slater determinant that minimizes the total electronic energy (E_{SD}) in this form:

$$E_{SD} = \min_{\langle \bar{b}_a | \bar{b}_b \rangle = \delta_{ab}} \left[\langle SD \mid \left(\sum_i H_i^{1e} + \sum_{\substack{i,j \\ i \neq j}} H_{ij}^{2e} \right) \mid SD \rangle \right]. \tag{2.19}$$

Considering general the validity of the variational principle, the energy coming from choosing as ground state of the system the Slater determinant will always be greater than the energy obtained through the real ground state associated to $\psi_k(\mathbf{r},\mathbf{R})$. In this approximation, the aim is to then introduce the right combination of single particle states into the determinant that minimizes the ground state energy.

It is also insightful to find an explicit form for the application of the Slater determinant on the two electron Hamiltonian. To achieve this it is useful to introduce a single particle projector operator $\mathcal{P}$ respecting the following properties:

$$\mathcal{P} = \sum_i^{N_e} \left|\bar{b}_i\right\rangle\left\langle\bar{b}_i\right|; \quad \mathcal{P}^2 = \mathcal{P}; \quad Tr[\mathcal{P}] = N_e; \quad E^{(1e)} = Tr\left[\mathcal{P}\sum_i H_i^{(1e)}\right], \tag{2.20}$$

which when expressed in the Schrödinger space with the inclusion of the spin (σ) it takes the form

$$\rho(\mathbf{r},\mathbf{r}',\sigma,\sigma') = \langle \mathbf{r},\sigma|\mathcal{P}\left|\mathbf{r}',\sigma'\right\rangle. \tag{2.21}$$

The effect of the Slather determinant over the two particle Hamiltonian can then be written as

$$\langle SD|\sum_{i,j,i\neq j}\hat{H}_{i,j}^{(2e)}|SD\rangle = E^{(2e)} = \frac{1}{2}\int d\mathbf{r}d\mathbf{r}'\frac{1}{4\pi\epsilon_0}\frac{e^2}{|\,\mathbf{r}-\mathbf{r}'\,|}\sum_{\substack{i,j\\ \sigma,\sigma'}}$$
$$\left[\left\langle\bar{b}_i\middle|\mathbf{r},\sigma\right\rangle\left\langle\mathbf{r},\sigma\middle|\bar{b}_i\right\rangle\left\langle\bar{b}_j\middle|\mathbf{r}',\sigma'\right\rangle\left\langle\mathbf{r}',\sigma'\middle|\bar{b}_j\right\rangle - \left\langle\bar{b}_i\middle|\mathbf{r},s\right\rangle\left\langle\mathbf{r},s\middle|\bar{b}_j\right\rangle\left\langle\bar{b}_j\middle|\mathbf{r}',s'\right\rangle\left\langle\mathbf{r}',s'\middle|\bar{b}_i\right\rangle\right], \tag{2.22}$$

and, taking advantage of the density operator, it can be expressed in the more compact form

$$E^{(2e)} = \frac{1}{2}\int d\mathbf{r}d\mathbf{r}'\frac{1}{4\pi\epsilon_0}\frac{e^2}{|\,\mathbf{r}-\mathbf{r}'\,|}\sum_{\sigma,\sigma'}$$
$$\left[\rho(\mathbf{r},\mathbf{r},\sigma,\sigma)\rho(\mathbf{r}',\mathbf{r}',\sigma',\sigma') - \rho(\mathbf{r},\mathbf{r}',\sigma,\sigma')\rho(\mathbf{r}',\mathbf{r},\sigma',\sigma)\right]. \tag{2.23}$$

In this last equation, the term coming from the integral of the first term in the square brakets is called the Hartree term and takes in consideration the energy coming from the Coulomb interaction between the probability density of two electrons. The remaining term, is called the exchange term, and it energetically describes the effect coming from the antisymmetric

nature of the general electronic state, the Fermi repulsion. Furthermore, the combination of the two terms into the square brackets defines the two electron density probability. In the next sections, it will be shown the possibility of using such quantity to investigate the localization properties of electrons.

One limit of this approximation is clear: the electronic interaction between the electrons is based upon their unperturbed single particle states. It is reasonable to expect that, if two electrons are correlated, the probability of finding the first electron at a certain position in space depends on the position of the second electron and vice versa. In other words, the product of their independent density functions does not adequately describe the real state. At small distances, the uncorrelated pair density is too large as electrons are expected to repel each other, while, at large distances, the uncorrelated pair density is too small for somewhat the same reason. These kind of effects are called correlation effects. Most of the time they cannot be neglected while looking for an accurate solution of the ground state of the system.

2.4 DENSITY FUNCTIONAL THEORY

Density functional theory (DFT) is an exact theory proposing that any property of a many interacting particle system can be described as a functional of the ground state density $\rho(\mathbf{r})$, since the latter is able to determine all the information for the general ground state wave function and all excited states. Although DFT alone is of no practical use without approximations, it has proven to be a key concept that has made possible the development of many computational methods now at the core of theoretical condensed matter science. In the framework of DFT, the general electronic Hamiltonian (H_e) is expressed in the form

$$H = -\sum_i \frac{1}{2}\frac{\hbar^2 \nabla_i^2}{m_e} + \frac{1}{2}\sum_{i,j,i\neq j} \frac{1}{4\pi\epsilon_0}\frac{e^2}{|\,\mathbf{r}_i - \mathbf{r}_j\,|} + V_{ext}, \tag{2.24}$$

where V_{ext} represents a generic external potential in the electronic system, but in most cases it is interpreted as the electron-nuclei interaction. The ground state density $\rho(\mathbf{r})$ is then determined as

$$\rho(\mathbf{r}) = \langle \psi_{GS} \Big| \sum_{i,\sigma} |\mathbf{r}_i, \sigma\rangle\langle \mathbf{r}_i, \sigma| \,|\, \psi_{GS}\rangle, \tag{2.25}$$

where ψ_{GS} is the ground state wave function for the DFT Hamiltonian.

The basic theorems of DFT [68] state that, for any system of interacting particles in an external potential V_{ext}, its potential is uniquely defined,

except for a constant, by the ground state particle density $\rho(\mathbf{r})$. Since the Hamiltonian is fully determined, except for a constant shift in energy, it follows that the many-body wave functions for all states are determined. This leads to the statement that all properties of the system are completely determined given only the ground state density $\rho(\mathbf{r})$. In addition, it is possible to define a universal functional for the ground state energy $E[\rho(\mathbf{r})]$ in terms of the ground state density $\rho(\mathbf{r})$ of the form

$$E[\rho(\mathbf{r})] = F[\rho(\mathbf{r})] + \int d\mathbf{r} V_{ext}(\mathbf{r})\rho(\mathbf{r}), \tag{2.26}$$

where $F[\rho]$ is referred to the application of the ground state over the kinetic and electron-electron Coulomb interaction operator as

$$F[\rho(\mathbf{r})] = \left\langle \psi_{GS}^{[\rho]} \middle| \hat{T}_e + \hat{V}_{ee} \middle| \psi_{GS}^{[\rho]} \right\rangle. \tag{2.27}$$

For any particular V_{ext}, the exact ground state energy corresponds to the minimum of the functional $E[\rho(\mathbf{r})]$ for the given system and the density that minimizes it is the exact ground state density $\rho(\mathbf{r})$.

DFT is, however, just a reframing of the many-body problem and it is not able to reduce the complexity of the electronic states. Ultimately, the electronic ground state density is still dependent on the ground state wave fuction, which most often cannot be derived. A clever solution to this problem is obtained through the Kohn-Sham mapping, which transfers the many body system into a non interacting particles system similar to the Hartree-Fock method. With the right approximations, the Kohn-Sham mapping can then lead to remarkable results.

2.4.1 *The Kohn-Sham mapping*

Effectively, the theorems of DFT state a relationship between the external potential V_{ext} and the density $\rho(\mathbf{r})$, but do not make assumptions on the specific of the electronic system itself. In the Kohn-Sham approach, the many-body interacting system defined by the electronic Hamiltonian is therefore replaced with an auxiliary system composed by non interacting electrons which are described by a set of single particle wave functions $\{\bar{\psi}_i^{KS}\}_{i=1,\dots\frac{N_e}{2}}$. In this case, the index i spans only on half the number of electron as the spin is assumed to be isotropic in the system. This auxiliary system has the advantage of being much easier to solve numerically. The main goal is then to map the general many-body system through this non interacting system. To achieve this, all the many-body terms related to the particle interactions are incorporated into an exchange and correlation functional of the density.

To work toward this procedure, it is possible to start by representing the ground state density for the auxiliary single particle system as

$$\rho(\mathbf{r}) = \sum_{i,\sigma} \left\langle \bar{\psi}_i^{KS} \middle| \mathbf{r}_i, \sigma \right\rangle \left\langle \mathbf{r}_i, \sigma \middle| \bar{\psi}_i^{KS} \right\rangle. \tag{2.28}$$

The auxiliary single particle Hamiltonian is then chosen so to have the usual kinetic operator and an effective local potential V^{KS} acting on an electron with certain spin located at position $\mathbf{r}_i$. This auxiliary Hamiltonian has the form:

$$H^{KS} = -\frac{\hbar^2 \boldsymbol{\nabla}^2}{2m_e} + V^{KS}(\mathbf{r}), \tag{2.29}$$

and satisfies the following shrödinger equation:

$$H^{KS} \left| \bar{\psi}_i^{KS} \right\rangle = E_i \left| \bar{\psi}_i^{KS} \right\rangle. \tag{2.30}$$

As mentioned before, the Kohn-Sham approach to the full interacting many-body problem is to rewrite the universal functional previously defined in equation (2.26) for the many body interacting system trough the auxiliary system in the form

$$E[\rho] = T_0[\rho] + E_H[\rho] + E_{XC}[\rho] + \int d\mathbf{r} V_{ext}(\mathbf{r})\rho(\mathbf{r}). \tag{2.31}$$

Here $T_0[\rho]$ represents the total kinetic energy for the non interacting particles system:

$$T_0[\rho] = -2 \sum_{i}^{N_e/2} \left\langle \psi_i^{KS} \middle| \frac{\hbar^2 \boldsymbol{\nabla}_{\mathbf{r}}^2}{2m_e} \middle| \psi_i^{KS} \right\rangle, \tag{2.32}$$

where the 2 in front of the right side of the equation takes into account the two possible spin state for the wavefunctions ψ_i^{KS}. Furthermore, $E_H[\rho]$ represents the Hartree term for the non interacting system:

$$E_H[\rho] = \frac{1}{2} \int d\mathbf{r} d\mathbf{r}' \frac{e^2}{4\pi\epsilon_0} \frac{\rho(\mathbf{r})\rho(\mathbf{r}')}{|\,\mathbf{r} - \mathbf{r}'\,|}. \tag{2.33}$$

$E_{XC}[\rho]$ is instead an energetic terms that includes all the corrections coming from the exchange properties and the correlation effects of the many-body system. This quantity is implicitly defined through the real solution of the functional $F[\rho]$ for the many-body system of equation (2.27) as

$$E_{XC}[\rho] = F[\rho] - E_H[\rho] - T_0[\rho]. \tag{2.34}$$

Finally, the external potential V_{ext} is the same external potential of the many-body problem. The mapping from the universal energy functional

$E[\rho]$ to the Kohn-Sham system is done considering that it is possible to write the Kohn-Sham energy as

$$E_{KS}[\rho] = E_H[\rho] + E_{XC}[\rho] + \int d\mathbf{r} V_{ext}(\mathbf{r})\rho(\mathbf{r}), \tag{2.35}$$

so that

$$E[\rho] = T_0[\rho] + E_{KS}[\rho]. \tag{2.36}$$

With these definitions, the energy of the ground state for the single particle system can be obtained by choosing the right set of Kohn-Sham wave functions that minimize the energy functional:

$$E_{GS} = \min_{\rho(\mathbf{r})} E[\rho] = \min_{\substack{\{|\bar{\psi}_i^{KS}\rangle\}_{i=1,\dots,\frac{N_e}{2}} \\ \langle\bar{\psi}_i^{KS}|\bar{\psi}_j^{KS}\rangle = \delta_{ij}\delta_{\sigma\sigma'}}} \Big[T_0[\rho] + E_{KS}[\rho]\Big]. \tag{2.37}$$

In theory, the ground state energy E_{GS} given by the Kohn-Sham mapping corresponds to the real ground state energy for the many body interacting system. However, although this expression appears simple to solve, it still contains inside the complexity of the many-body electronic states. In this formalism, such complexity is transferred to the exact exchange correlation energy ($E_{XC}[\rho]$) used in the single particle auxiliary system. Finding the exact exchange-correlation energy is far from being possible and it is necessary to rely on some approximations. Regardless of this issue, a solution to the Kohn-Sham problem can be obtained by explicitly deriving the form of the Kohn-Sham potential (V^{KS}). To do so it is possible to use the Lagrange multipliers imposing the normalization of the density as

$$\frac{\partial}{\partial\rho}\left[E[\rho] - \lambda\left(N_e - \int d\mathbf{r}\rho(\mathbf{r})\right)\right] = 0, \tag{2.38}$$

or better expressed through the set of Kohn-Sham single particle wave functions as

$$\frac{\partial}{\partial\langle\psi_k^{KS}|}\left[E[\{\psi_i^{KS}\}] - 2\sum_{i,j}\lambda_{i,j}\left(\langle\psi_i^{KS}|\psi_j^{KS}\rangle - \delta_{ij}\right)\right] = 0. \tag{2.39}$$

In these equations λ represents a set of Lagrange multipliers. Considering the form of $E[\rho]$ shown in equation (2.31), it is possible to derive each term with the respective forms:

$$\frac{\partial}{\partial\langle\psi_k^{KS}|}T_0[\rho] = -4\frac{\hbar\boldsymbol{\nabla}^2}{2m_e}|\psi_k^{KS}\rangle \tag{2.40}$$

for the kinetic term,

$$\frac{\partial}{\partial\left\langle\psi_k^{KS}\right|}E_H[\rho] = 4\int d\mathbf{r}'\frac{e^2}{4\pi\epsilon_0}\frac{\rho(\mathbf{r}')}{|\,\mathbf{r}-\mathbf{r}'\,|}|\mathbf{r}\rangle\langle\mathbf{r}\,|\left|\psi_k^{KS}\right\rangle = 4V_H\left|\psi_k^{KS}\right\rangle \tag{2.41}$$

for the Hartree potential term, and

$$\frac{\partial}{\partial\left\langle\psi_k^{KS}\right|}E_{XC}[\rho] = 4\frac{\partial E_{XC}}{\partial\rho}(\mathbf{r})|\mathbf{r}\rangle\langle\mathbf{r}\,|\left|\psi_k^{KS}\right\rangle = 4V_{XC}\left|\psi_k^{KS}\right\rangle, \tag{2.42}$$

for the exchange correlation potential. Combining all the pieces together it is possible to construct the explicit Kohn-Sham Schrödinger equation as

$$\left[-\frac{\hbar\nabla_{\mathbf{r}}^2}{2m_e} + V_H(\mathbf{r}) + V_{XC}(\mathbf{r}) + V_{ext}(\mathbf{r})\right]\left|\psi_k^{KS}\right\rangle = \sum_i \lambda_{i,k}\left|\psi_i^{KS}\right\rangle. \tag{2.43}$$

With a proper unitary rotation of the single particle wave function $\psi_k^{KS} \rightarrow \widetilde{\psi}_k^{KS}$, the previous equation can be rewritten in a diagonal form as

$$\left[-\frac{\hbar\nabla_{\mathbf{r}}^2}{2m_e} + V_H(\mathbf{r}) + V_{XC}(\mathbf{r}) + V_{ext}(\mathbf{r})\right]\left|\widetilde{\psi}_k^{KS}\right\rangle = \epsilon_k\left|\widetilde{\psi}_k^{KS}\right\rangle. \tag{2.44}$$

Finally the Kohn-Sham potential is expressed as the sum of all the individual potentials

$$V^{KS}(\mathbf{r}) = V_H(\mathbf{r}) + V_{XC}(\mathbf{r}) + V_{ext}(\mathbf{r}). \tag{2.45}$$

Assuming that the exchange correlation potential is known, equation (2.44) is solved through a self-consistent loop. An initial guess for the density is used to determine the Kohn-Sham potential of equation (2.45), which is a functional of the density. With the guessed density and potential, equation (2.44) is solved. The resulting new Kohn-Sham states, obtained through the solution of equation (2.44), are then used to compute a new density which is then used again to solve equation (2.45). This cycle repeats until the density is well converged. It is also important to mention that the eigenvalues (ϵ_k) of equation (2.44) are to be treated only as the auxiliary energy states for the single particle wave functions. However, they are generally interpreted as being the many-body system energy states.

2.4.2 *Generalities for the exchange correlation functional*

As anticipated in the previous section, the bigger and only roadblock for the electronic problem practical resolution is related to the inscrutable nature of the exchange-correlation term and the impossibility to derive its exact

expression. However, some reasonable approximations leading to good results can be made. One option is to consider that the behavior of the valence electrons in a solid is quite similar to the one of the free electron gas. In this case, the idea is to substitute the general exact exchange-correlation energy with the one for the free electron gas. At each point in space for this system, the exchange energy can be obtained exactly, while the correlation term has been extensively studied and derived through Monte-Carlo methods [69]. This approximation takes the name of the local density approximation (LDA).

In the LDA the exchange-correlation energy is defined as

$$E_{XC}(\mathbf{r}) \simeq E_{XC}^{LDA}(\mathbf{r}) = \int d\mathbf{r}\rho(\mathbf{r})\epsilon_{XC}(\rho(\mathbf{r})), \tag{2.46}$$

where $\epsilon_{XC}(\rho(\mathbf{r}))$ is the exchange-correlation energy density for the free electron gas. From this expression, the exchange-correlation potential can be derived as

$$V_{XC}(\mathbf{r}) = \epsilon_{XC}(\rho(\mathbf{r})) + \rho(\mathbf{r})\frac{\partial\epsilon_{XC}(\rho(\mathbf{r}))}{\partial\rho(\mathbf{r})}. \tag{2.47}$$

Another approximation for the exchange correlation energy is derived by expressing the exchange correlation energy as a function of the density and its gradient [70]. This approximation takes the name of the generalized gradient approximation (GGA) and has the form

$$E_{XC}(\mathbf{r}) \simeq E_{XC}^{GGA}(\mathbf{r}) = \int d\mathbf{r}\rho(\mathbf{r})\epsilon_{X}^{hom}(\rho(\mathbf{r}))F_{XC}(\rho(\mathbf{r}), \nabla\rho(\mathbf{r})). \tag{2.48}$$

In this expression F_{XC} is a dimentionless function while $\epsilon_X^{hom}(\rho(\mathbf{r}))$ is the exchange energy of the free electron gas.

These approximations generally yield good results but with limitations. Usually the LDA is more accurate for describing solids behaving as free electron gasses while the GGA performs better when the electronic density is more localized or exhibits strong variations in space. The general shortcomings for both LDA and GGA are related to the underestimation of the electronic band gap [71–73]. Ultimately however, there is no general rule to determine which functional is better to describe the exchange-correlation energy and, often, the functional of choice is the one that best describes the experimental measurements.

2.4.3 *Generalities for the pseudopotentials*

For a solid system to exist, its basic constituents, the atoms, need to form bonds that are able to keep the structure together. For this to happen,

the electrons orbiting the nuclei need to be able to pass from a nucleus to another. However, not all electrons take part in this exchange process and, usually, just the few highest energy ones, the valence electrons, are able to hop to another adjacent nucleus. These same electrons are those that give rise to the properties of a system, such as conductivity, charge density waves or even superconductivity. Practically, the lower energetic electrons, the core electrons, are locked in close to their respective nuclei and can be neglected when describing the bonding interactions.

While performing a simulation, it is important to consider that being able to neglect the unnecessary constituents of a system comes to great computational advantage both in terms of memory storage and time. For this reason, there are all the incentives to neglect the description of the core electrons while attempting to model the properties of a system. To achieve this, pseudopotentials are often used instead of the real atomic potential. The main goal of the pseudopotentials is to cut out from the computations all the electronic degrees of freedom which are unnecessary to describe the valence properties of the system. Usually, this description is achieved by giving the pseudopotential a specific core radius r_c, above which the potential resembles exactly the atomic one, and below which, it differs from the real atomic potential and is approximated with a much smoother curve.

There are different types of pseudopotential approximations and each of them comes with advantages and disadvantages. The most used are the norm conserving pseudopotentials [74]. These pseudopotentials are normalized and are solutions of a model potential chosen to reproduce the valence properties of an all electron calculation. They are built so that the Kohn-Shan states satisfy an orthonormal relationship between each other. An extension to the norm conserving pseudopotentials are the ultrasoft ones [75, 76]. These pseudopotentials aim to create an ultra smooth function faster to converge than norm conserving pseudopotentials. To achieve this it is necessary to relax the condition of orthonormality between the Kohn-Shan states. Another method to describe pseudo interactions are given by the projector augmented-wave method (PAW) [77–79]. This is a general approach to the solution of the electronic structure problem that keeps the full-electron wave function of a system. Since the wave function varies rapidly near the nucleus of an atom, the integrals are described as combinations of smooth functions extending through space and a set of localized contributions evaluated by radial integration over muffin-thin spheres located at the center of the nuclei.

2.4.4 *Periodicity and Bloch wave function*

As previously mentioned, the problem of electrons in a solid is a complex many-body problem. The full Hamiltonian contains both the one electron potential, describing the interactions between ions and nuclei, and the two-body term describing the electron-electron interactions. In the Kohn-Sham approach to DFT, it was shown that the complete many particle system can be mapped into a single particle problem represented by an effective one-electron potential V_{KS}. Whatever detail the one electron effective potential might have, if the crystal is perfectly lattice periodic, the effective potential must satisfy the same periodicity of the crystal:

$$V_{KS}(\mathbf{r}+\mathbf{T}) = V_{KS}(\mathbf{r}). \tag{2.49}$$

Here $\mathbf{T}$ is a generic lattice vector [14]. From this, the independent electrons, described by the one particle Hamiltoninan

$$H_{KS}\left|\psi_{n\mathbf{k}'}\right\rangle = \left[-\frac{\hbar^2\boldsymbol{\nabla}^2}{2m_e} + V_{KS}(\mathbf{r})\right]\left|\psi_{n\mathbf{k}'}\right\rangle = \epsilon_{n\mathbf{k}'}\left|\psi_{n\mathbf{k}'}\right\rangle, \tag{2.50}$$

follow the rule for the Bloch electrons [15], and obey the following important property:

$$\psi_{n\mathbf{k}'}(\mathbf{r}+\mathbf{T}) = e^{i\mathbf{k}'\cdot\mathbf{T}}\psi_{n\mathbf{k}'}(\mathbf{r}). \tag{2.51}$$

Here $\mathbf{k}'$ is a generic plane wave vector and an additional index n, usually referred as the band index, is introduced to signify that the Hamiltonian H_{KS} admits more than one solution for each $\mathbf{k}'$.

In order to properly describe the system, a set of boundary conditions are introduced for the wavefunction $\psi_{n\mathbf{k}'}(\mathbf{r})$ in the lattice of volume Ω. The application of such boundary conditions imposes that $e^{i\mathbf{G}\cdot\mathbf{T}} = 1$, where $\mathbf{G}$ is called a reciprocal lattice vector. The set of all plane wave vectors $\mathbf{k}$ smaller then the smallest reciprocal lattice vectors $\mathbf{G}^0$, defines the first Brillouin zone. Any generic vector $\mathbf{k}'$ inside or outside the Brillouin zone can then be defined as a vector inside the Brillouin zone $\mathbf{k}$, plus a reciprocal lattice vector as

$$\mathbf{k}' = \mathbf{k} + \mathbf{G}. \tag{2.52}$$

This allows to expand the wave function $\psi_{n\mathbf{k}}$ as

$$\left|\psi_{n\mathbf{k}}\right\rangle = \sum_{\mathbf{G}} c_{n\mathbf{k}+\mathbf{G}}\left|\mathbf{k}+\mathbf{G}\right\rangle, \tag{2.53}$$

where $|\mathbf{k}+\mathbf{G}\rangle$ has the form

$$\langle\mathbf{r}|\mathbf{k}+\mathbf{G}\rangle = \frac{1}{\sqrt{\Omega}}e^{i(\mathbf{k}+\mathbf{G})\cdot\mathbf{r}}. \tag{2.54}$$

Whenever attempting to solve equation (2.50) for a volume Ω, it is then necessary to consider an infinite amount of reciprocal lattice vectors $\mathbf{G}$. This is of course computationally unpractical. Often a cutoff E_{cut} is taken so that the $\mathbf{G}$ vectors taken in the sum of equation (2.53) can be truncated as

$$\frac{1}{2} \mid \mathbf{k} + \mathbf{G} \mid^2 < E_{cut}. \tag{2.55}$$

The value of E_{cut} is chosen big enough so to include enough vectors $\mathbf{G}$ to be able to accurately converge the wave function $\psi_{n\mathbf{k}}$.

Following the Bloch theorem, the wave function $\psi_{n\mathbf{k}}(\mathbf{r})$ can be decomposed in a plane wave times a periodic function in the unit cell as

$$\psi_{n\mathbf{k}'}(\mathbf{r}) = e^{i\mathbf{k}'\cdot\mathbf{r}} u_{n\mathbf{k}'}(\mathbf{r}), \tag{2.56}$$

where $u_{n\mathbf{k}'}(\mathbf{r})$ respects the following properties:

$$u_{n\mathbf{k}'}(\mathbf{r}+\mathbf{T}) = u_{n\mathbf{k}'}(\mathbf{r}), \quad \langle \psi_{n\mathbf{k}'}(\mathbf{r}) \big| \psi_{n'\mathbf{k}''}(\mathbf{r}) \rangle = \langle u_{n\mathbf{k}'}(\mathbf{r}) | u_{n'\mathbf{k}''}(\mathbf{r}) \rangle = \delta_{\substack{nn' \\ \mathbf{k}'\mathbf{k}''}}. \tag{2.57}$$

With this set of wave functions it is also possible to calculate the electronic density through the sum of vectors $\mathbf{k}$ inside the Brillouin zone as

$$\rho(\mathbf{r}) = \sum_{n\mathbf{k}} f_{n\mathbf{k}} \langle u_{n\mathbf{k}} | u_{n\mathbf{k}} \rangle, \tag{2.58}$$

where $f_{n\mathbf{k}}$ is the occupation function

$$f_{n\mathbf{k}} = \frac{2}{e^{\beta(\epsilon_{n\mathbf{k}} - \epsilon_F)} + 1}. \tag{2.59}$$

Here $\beta = 1/k_B T$, with k_B the Boltzmann's constant and T the temperature, and ϵ_F is the Fermi energy, the highest occupied energy. The factor 2 comes from the spin degeneracy of the Kohn-Sham states. Additionally, it is also possible to introduce the density of states (DOS). This quantity represents the amount of available $\mathbf{k}$ states for a generic energy ϵ and is calculated as

$$N(\epsilon) = \frac{2}{\Omega} \sum_{n\mathbf{k}} \delta(\epsilon - \epsilon_{n\mathbf{k}}). \tag{2.60}$$

It is important to mention that in order to get an accurate result in equations (2.60) and (2.58), one would have to sum over an infinite amount of states $\mathbf{k}$. On a computational level, this choice is far from being practical and the sums over $\mathbf{k}$ are kept finite. In this case, specific grids for the states $\mathbf{k}$, such as the Monkhorst-Pack grid [80], can be chosen to increase the accuracy. Additionally, for the same reasons, smearing functions such as the Methfessel-Paxton smearing [81] are introduced for the occupation function $f_{n\mathbf{k}}$.

2.5 ELECTRON LOCALIZATION FUNCTION

A question that one might ask is related to the position of pairs of electrons in a certain zone of space inside the material. Although this question might appear ill defined, it is often considered in a chemical sense in order to identify the chemical bonds holding the structure together. The ill definition of the question comes from the quantum nature of electrons, which obey the Heisenberg principle. In a strict sense, it is meaningless to speak about the position of an electron, as such particles are delocalized in their quantum description, and is not easy to derive the positional information of pairs through the Schrödinger equation. There are, however, better ways to approach the problem. To start, it is useful to remember that the general wave function of the system contains all the information related to the asymmetric state of the electrons imposed by the Pauli principle. This gives rise to the concept of Fermi hole [82] that, for a given electron with a certain spin in a given position, measures the probability of finding another electron with the same spin in another point in space. It is of course expected that such probability goes to zero whenever the two electrons find themselves in the same position as to respect the Pauli principle. In a way, the Fermi hole describes the spacial delocalization of the charge of a reference electron. If the Fermi hole of a reference electron with certain spin is extremely localized in a certain region of space, then all other electrons with same spin are excluded from that region. Furthermore, the Fermi hole acts only between electrons with the same spin. This means that the existence of a localized electron implies that there exists a high probability of finding two electrons of opposite spin in a given region of space, simply because of the absence of Pauli repulsion. For these localized pair of electrons, there will be a small probability of exchange with other electrons outside of this region.

To work towards a simple expression that could help better define this concept, it is necessary to recall the expression (2.23) for the two particle energy in the Hartree-Fock approximation and consider the two electron probability. The latter is expressed as

$$\rho^{2e}(\mathbf{r},\mathbf{r}',\sigma,\sigma') = \rho(\mathbf{r},\mathbf{r},\sigma,\sigma)\rho(\mathbf{r}',\mathbf{r}',\sigma',\sigma') - \rho(\mathbf{r},\mathbf{r}',\sigma,\sigma')\rho(\mathbf{r}',\mathbf{r},\sigma',\sigma). \quad (2.61)$$

This quantity expresses the probability of finding an electron with spin σ in position $\mathbf{r}$ and another electron with spin σ' in position $\mathbf{r}'$. Furthermore, it was shown that it respects the anti-symmetric constrains for the wave function related to the fermionic nature of the electrons. It is then useful to look to the same spin two electron probability, and define a conditioned probability of finding an electron at position $\mathbf{r}'$ knowing there is already an

electron at position **r**:

$$P^{2e}_{cond}(\mathbf{r},\mathbf{r}',\sigma) = \frac{\rho^{2e}(\mathbf{r},\mathbf{r}',\sigma,\sigma)}{\rho(\mathbf{r},\mathbf{r},\sigma,\sigma)} = \rho(\mathbf{r}',\mathbf{r}',\sigma,\sigma) - \frac{|\,\rho(\mathbf{r},\mathbf{r}',\sigma,\sigma)\,|^2}{\rho(\mathbf{r},\mathbf{r},\sigma,\sigma)}. \tag{2.62}$$

By looking for the probability of finding **r** close to **r**′ and expanding the expression through the spherical average of the Taylor expansion [83, 84] with $\mathbf{r}' = \mathbf{r} + \delta$ one obtains:

$$\langle P^{2e}_{cond}(\mathbf{r},\mathbf{r}',\sigma)\rangle_{\mathbf{r}'=\mathbf{r}} = \frac{1}{3}\left[\kappa(\mathbf{r},\sigma) - \frac{1}{4}\frac{(\nabla\rho(\mathbf{r},\mathbf{r},\sigma,\sigma))^2}{\rho(\mathbf{r},\mathbf{r},\sigma,\sigma)}\right]\delta^2 + \ldots, \tag{2.63}$$

where $\kappa(\mathbf{r},\sigma)$ is the kinetic energy density of the form

$$\kappa(\mathbf{r},\sigma) = \sum_i |\,\nabla\left\langle \mathbf{r},\sigma\middle|\bar{b}_i\right\rangle|^2\,. \tag{2.64}$$

In this expression the states $\bar{b}_i(\mathbf{r})$ represent a set of single particle orbitals. The main interest lies on the quantity in the brackets in equation (2.63):

$$D(\mathbf{r},\sigma) = \kappa(\mathbf{r},\sigma) - \frac{1}{4}\frac{(\nabla\rho(\mathbf{r},\mathbf{r},\sigma,\sigma))^2}{\rho(\mathbf{r},\mathbf{r},\sigma,\sigma)}. \tag{2.65}$$

$D(\mathbf{r},\sigma)$ is by definition positive and contains all the information related to the Pauli exclusion principle and the electron localization.

It is reasonable to expect that $D(\mathbf{r},\sigma)$ will be small in the regions of the space where the probability of finding a localized electron, or a localized pair of electrons with opposite spin, is high. However this function is not bound and can have arbitrarily high values, it is therefore an arbitrary decision how close to zero the value of $D(\mathbf{r},\sigma)$ has to be in order to consider an electron localized. For this reason two scaling rules are introduced. First, $D(\mathbf{r},\sigma)$ is tested against the free electron gas kinetic energy density:

$$\chi(\mathbf{r},\sigma) = \frac{D(\mathbf{r},\sigma)}{D_0(\mathbf{r},\sigma)}, \tag{2.66}$$

where the free electron gas kinetic energy has the form:

$$D_0(\mathbf{r},\sigma) = \frac{3}{5}(6\pi^2)^{2/3}\rho(\mathbf{r},\mathbf{r},\sigma,\sigma)^{5/3}. \tag{2.67}$$

Here $\rho(\mathbf{r},\mathbf{r},\sigma,\sigma)$ is the electronic density of the system under study. Second, the value of $\chi(\mathbf{r},\sigma)$ is renormalized to unity as

$$ELF(\mathbf{r},\sigma) = \frac{1}{1+\chi(\mathbf{r},\sigma)^2}. \tag{2.68}$$

This last formula defines the electron localization function [85] and it is a measure to describe zones of space where localized pairs of electrons with opposite spins sit with small probability of hopping to other areas. The electron localization function is not to be interpreted at every single value of $\mathbf{r}$, but instead through zones around the ELF maximum points. Such points are defined as attractors and one should look at zones of space surrounding the attractors and separated by the minimum values of $ELF(\mathbf{r}, \sigma)$.

CHAPTER 3

Phonons and the electron-phonon interaction

This chapter discusses the treatment of the nuclear part of the Born-Oppenheimer Hamiltonian. Starting from the harmonic approximation, the density functional perturbation theory for the solution of the phonon spectra is then described. The chapter expands on the electron-phonon interaction, the role of anharmonicity and the treatment of the quantum nuclear fluctuations described through the stochastic self consistent harmonic approximation.

3.1 The dynamical matrix

In this chapter, the interest lies on finding a solution for the ground state of the nuclear part of the Hamiltonian obeying equation (2.12). In order to study the dynamic of the ions, the usual first step is to assume the validity of the harmonic approximation [86], where it is assumed that the motion of the nuclei can be described through small vibrations around their equilibrium position $\mathbf{R}_0$. The equilibrium positions $\mathbf{R}_0$ are identified by the minimum of the potential $V(\mathbf{R})$ obtained by equation (2.12).

Considering this assumption, it is reasonable to expand the nuclear energy surface to second order with respect to the ion displacement $\tau_{pa\gamma}$:

$$\tau_{pa\gamma} = R_{pa\gamma} - R_{0,pa\gamma}, \tag{3.1}$$

where $R_{pa\gamma}$ represents the γth Cartesian coordinate for the position of the ath ion in the pth cell and $R_{0,pa\gamma}$ represents the equilibrium position of the same ion. In this approximation the potential energy surface $V(\mathbf{R})$ can be written as

$$V(\mathbf{R}) \approx V_0 + \frac{1}{2} \sum_{\substack{pa\gamma \\ p'a'\gamma'}} \left. \frac{\partial^2 V(\mathbf{R})}{\partial \tau_{p'a'\gamma'} \partial \tau_{pa\gamma}} \right|_{\mathbf{R}_0} \tau_{p'a'\gamma'} \tau_{pa\gamma}, \tag{3.2}$$

where V_0 represent the equilibrium energy where all the nuclei are in their equilibrium positions. In this last equation, the second derivatives of the potential with respect to the ion displacements are called the "interatomic force constants"

$$C_{\substack{pa\gamma \\ p'a'\gamma'}} = \frac{\partial^2 E(\mathbf{R})}{\partial \tau_{p'a'\gamma'} \partial \tau_{pa\gamma}}, \tag{3.3}$$

and are usually expressed through their reciprocal space form as "dynamical matrices". The dynamical matrices can be obtained through a Fourier transform of the interatomic force constants as

$$D_{\substack{a\gamma \\ a'\gamma'}}(\mathbf{q}) = \frac{1}{\sqrt{M_a M_{a'}}} \sum_{p} C_{\substack{pa\gamma \\ 0a'\gamma'}} e^{i(\mathbf{q}\cdot\mathbf{T}_p)}. \tag{3.4}$$

It is important to mention that for crystals the interatomic force constants are transnational invariant. For this reason, the Fourier transform is reduced just to the sum over a cell index p instead of both p and p'. Furthermore, the dynamical matrix is Hermitian and therefore admits $3N_n$ real eigenvalues $\omega_\nu^2(\mathbf{q})$, where N_n is the number of nuclei in the unit cell. With this in mind, equation (3.4) can be diagonalized in the following way:

$$\sum_{a'\gamma'} D_{\substack{a\gamma \\ a'\gamma'}}(\mathbf{q}) e_{a'\gamma',\nu}(\mathbf{q}) = \omega_\nu^2(\mathbf{q}) e_{a\gamma,\nu}(\mathbf{q}). \tag{3.5}$$

Here $e_{a\gamma,\nu}(\mathbf{q})$ represents the γ coordinate of the eigenvector of the ath atom at vector $\mathbf{q}$ and with mode ν. Additionally, it is possible to impose the condition of orthonormailty between the vectors through the following transformation:

$$\sum_{\nu} e^*_{a'\gamma',\nu}(\mathbf{q}) e_{a\gamma,\nu}(\mathbf{q}) = \delta_{aa'}\delta_{\gamma\gamma'} \quad \sum_{a\gamma} e^*_{a\gamma,\nu'}(\mathbf{q}) e_{a\gamma,\nu}(\mathbf{q}) = \delta_{\nu\nu'}. \tag{3.6}$$

The harmonic approximation made in equation (3.2) can be solved exactly in a simple manner by expressing the nuclear vibrational modes trough a series of $3N_n$ normal modes. To achieve this, the atomic displacements

and the momentum need to be rewritten in terms of the ladder operators $a_{\mathbf{q}\nu}$ and $a^{+}_{-\mathbf{q}\nu}$ as

$$\tau_{pa\gamma} = \frac{1}{\sqrt{N_p}} \sum_{\mathbf{q},\nu} e^{i(\mathbf{q}\cdot\mathbf{T}_p)} e_{a\gamma,\nu}(\mathbf{q}) \sqrt{\frac{\hbar}{2M_a\omega_\nu(\mathbf{q})}} (a_{\mathbf{q}\nu} + a^{+}_{-\mathbf{q}\nu}), \tag{3.7}$$

and

$$P_{pa\gamma} = \frac{i}{\sqrt{N_p}} \sum_{\mathbf{q},\nu} e^{i(\mathbf{q}\cdot\mathbf{T}_p)} e_{a\gamma,\nu}(\mathbf{q}) \sqrt{\frac{\hbar M_a\omega_\nu(\mathbf{q})}{2}} (a^{+}_{-\mathbf{q}\nu} - a_{\mathbf{q}\nu}), \tag{3.8}$$

where N_p represent the number of unit cells and where the ladder operators respect the following commutation rules:

$$\left[a_{\mathbf{q}\nu}, a^{+}_{\mathbf{q}'\nu'}\right] = \delta_{\mathbf{q}\mathbf{q}'}\delta_{\nu\nu'}, \quad \left[a_{\mathbf{q}\nu}, a_{\mathbf{q}'\nu'}\right] = 0, \quad \left[a^{+}_{\mathbf{q}\nu}, a^{+}_{\mathbf{q}'\nu'}\right] = 0. \tag{3.9}$$

In this case, the nuclear Hamiltonian for the independent oscillators can then be written by considering together equations (3.2), (3.5) and (3.7):

$$H = V_0 + \sum_{\mathbf{q}\nu} \hbar\omega_\nu(\mathbf{q}) \left(a^{+}_{\mathbf{q}\nu} a_{\mathbf{q}\nu} + \frac{1}{2} \right). \tag{3.10}$$

This final Hamiltonian describes the behavior of quasi particles of energy $\omega_\nu(\mathbf{q})$ composed by a quantum of vibration $(a_{\mathbf{q}\nu} + a^{+}_{-\mathbf{q}\nu})$ in the crystal lattice called phonon.

3.2 DYNAMICAL MATRIX THROUGH LINEAR RESPONSE

The previous section showed how to solve the nuclear Hamiltonian in the harmonic approximation and how to derive its diagonal expression. Although the solution appears simple in principle, all the complexity of the problem lies on determining the force constants of equation (3.3). Effectively, this means that the second derivatives of the potential $V(\mathbf{R})$ with respect to the nuclear displacements need to be calculated for all the atoms in the crystal.

One approach to solve the problem is called the finite displacement method. In this method, there is the need to create a supercell commensurate to each monochromatic perturbation of size $2\pi/\mathbf{q}$, and to have the atoms displaced accordingly with the given perturbation in order to sample the variation in the energy $V(\mathbf{R})$ with respect to the displacement. This approach, although generically straightforward and even if there are sophisticated methods to optimize the calculations [87], has obvious drawbacks associated with expressing phonon energies $\omega_\nu(\mathbf{q})$ through periodic displacements. Whenever there is the need to investigate the behavior of the

phononic spectra for $\mathbf{q} \to 0$, the size of the supercell for the system goes to infinity and the calculations become computationally unfeasible.

Another approach takes advantage of the functional for DFT [88] of equation (2.26) in order to obtain the dynamical matrices. Furthermore, this approach takes advantage of the possibility of expressing the force constants through the derivative of the functional with respect to the atomic displacements. The latter can be written as

$$\frac{\partial^2 V(\mathbf{R})}{\partial \tau_{pa} \partial \tau_{p'b}} = \int \frac{\partial \rho_{\mathbf{R}}(\mathbf{r})}{\partial \tau_{p'b}} \frac{\partial V_{ext}(\mathbf{r})}{\partial \tau_{pa}} d\mathbf{r} + \int \rho_{\mathbf{R}}(\mathbf{r}) \frac{\partial^2 V_{ext}(\mathbf{r})}{\partial \tau_{pa} \partial \tau_{p'b}} d\mathbf{r} + \frac{\partial^2 E_{nn}(\mathbf{R})}{\partial \tau_{pa} \partial \tau_{p'b}}. \quad (3.11)$$

This equation shows that the calculation of the Born-Oppenheimer energy surface requires the calculation of the ground-state electron charge density $\rho(\mathbf{r})$ as well as of its response to a distortion of the nuclear geometry $\partial\rho(\mathbf{r})/\partial\tau$. It is reasonable to expect that the response of the density can be treated linearly whenever this distortion is small.

The real advantage of this procedure appears in conjunction of the specific form of the Bloch states. Attempting to solve the system by treating the ionic displacement as monochromatic perturbations will lead to have the responses to different wavelengths decoupled. This feature makes so phonon frequencies can be calculated at arbitrary wave vectors $\mathbf{q}$ without the need of introducing supercells. This will be shown throughout this and the next section. Ultimately this leads to the electronic calculations becoming completely independent from the wavelength. To achieve this, it is convenient to work with a reciprocal lattice version of the force constant:

$$C^{\,a\gamma}_{a'\gamma'}(\mathbf{q}) = \sqrt{M_a} D^{\,a\gamma}_{a'\gamma'}(\mathbf{q}) \sqrt{M_{a'}}, \quad (3.12)$$

and it is useful to express the external potential $V_{ext}(\mathbf{r})$ as a sum of individual nuclear contributions in the following form:

$$V_{ext}(\mathbf{r}) = \sum_{pa} V_a(\mathbf{r} - \mathbf{R}_a + \mathbf{T}_p). \quad (3.13)$$

Here a sums over all the atoms in the unit cell and p sums over all the lattice vectors in the chosen supercell N_p. It is then convenient to calculate the derivative of the external potential with respect to the nuclear displacements in the reciprocal space as

$$V'^{\mathbf{q}a\gamma}_{ext}(\mathbf{r}) = \sum_{p} e^{i\mathbf{q}(\mathbf{T}_p + \mathbf{R}_a)} \frac{\partial V_a(\mathbf{r} - \mathbf{R}_a + \mathbf{T}_p)}{\partial \tau_{pa\gamma}(\mathbf{r})}. \quad (3.14)$$

Furthermore, it is possible to express the derivative of the external potential in a manner similar to the Bloch states by having a plane wave times a

periodic function of the form

$$V'^{\mathbf{q}a\gamma}_{ext}(\mathbf{r}) = e^{i\mathbf{q}\cdot\mathbf{r}} v'^{\mathbf{q}a\gamma}_{ext}(\mathbf{r}), \tag{3.15}$$

where

$$v'^{\mathbf{q}a\gamma}_{ext}(\mathbf{r}) = \sum_p e^{-i\mathbf{q}(\mathbf{r}-\mathbf{T}_p-\mathbf{R}_a)} \frac{\partial V_a(\mathbf{r}-\mathbf{R}_a+\mathbf{T}_p)}{\partial \tau_{pa\gamma}(\mathbf{r})}. \tag{3.16}$$

These same considerations apply to the variation of the general Kohn-Sham potential in response to a density perturbation $\Delta V_{KS}(\mathbf{r})$. The latter can be expressed as well in a similar form to equation (3.15) as

$$\Delta V^{\mathbf{q}a\gamma}_{KS}(\mathbf{r}) = e^{i\mathbf{q}\cdot\mathbf{r}} \Delta v^{\mathbf{q}a\gamma}_{KS}(\mathbf{r}). \tag{3.17}$$

At this point in the derivation, the form of $\Delta v^{\mathbf{q}a\gamma}_{KS}(\mathbf{r})$ will not be defined and will be treated in the next section. This quantity, as shown before, is functional of the density $\rho(\mathbf{r})$ and is expected to depend on the linear response of the density to the atomic displacement. The latter can be obtained through perturbation theory by expressing the variation of the Kohn-Sham states as

$$\left|\Delta\psi^{\mathbf{q}a\gamma}_{i\mathbf{k}}\right\rangle = \sum_{j\mathbf{k}'} \left|\psi_{j\mathbf{k}'}\right\rangle \frac{\left\langle\psi_{j\mathbf{k}'}\right| e^{i\mathbf{q}\cdot\mathbf{r}} \Delta v^{\mathbf{q}a\gamma}_{KS}(\mathbf{r}) \left|\psi_{i\mathbf{k}}\right\rangle}{\epsilon_{i\mathbf{k}} - \epsilon_{j\mathbf{k}'}}, \tag{3.18}$$

where the sum over $\mathbf{k}$ and j extends over both occupied and empty states. Considering the form of the Bloch states, the perturbation can be expressed through the periodic part in the unit cell. This leads to a simplification in the sum over the $\mathbf{k}$ states as

$$\left|\Delta u^{\mathbf{q}a\gamma}_{i\mathbf{k}}\right\rangle = \sum_{j} \left|u_{j\mathbf{k}+\mathbf{q}}\right\rangle \frac{\left\langle u_{j\mathbf{k}+\mathbf{q}}\right| \Delta v^{\mathbf{q}a\gamma}_{KS}(\mathbf{r}) \left|u_{i\mathbf{k}}\right\rangle}{\epsilon_{i\mathbf{k}} - \epsilon_{j\mathbf{k}+\mathbf{q}}}. \tag{3.19}$$

With this expression, it is possible to define the induced charge density arising in response of the perturbation as

$$\Delta\rho_{\mathbf{q}a\gamma}(\mathbf{r}) = \frac{e^{i\mathbf{q}\cdot\mathbf{r}}}{N_p} \sum_{i\mathbf{k}} \left[\langle u_{i\mathbf{k}}|\mathbf{r}\rangle \left\langle \mathbf{r}\right|\Delta u^{\mathbf{q}a\gamma}_{i\mathbf{k}}\right\rangle + \left\langle \Delta u^{-\mathbf{q}a\gamma}_{i\mathbf{k}}\right|\mathbf{r}\right\rangle \langle \mathbf{r}|u_{i\mathbf{k}}\rangle \Big]. \tag{3.20}$$

Finally, the reciprocal space form of the dynamical matrix in equation (3.11) can be obtained by substituting all the terms as

$$\begin{aligned} C^{\ a\gamma}_{a'\gamma'}(\mathbf{q}) = \sum_{i\mathbf{k}} \Big[&\left\langle \Delta u^{-\mathbf{q}a\gamma}_{i\mathbf{k}}\right| v'^{\mathbf{q}a\gamma}_{ext}(\mathbf{r}) |u_{i\mathbf{k}}\rangle + \langle u_{i\mathbf{k}}| v'^{-\mathbf{q}a\gamma}_{ext}(\mathbf{r}) \left|\Delta u^{\mathbf{q}a\gamma}_{i\mathbf{k}}\right\rangle \Big] \\ &+ \int d\mathbf{r}\rho(\mathbf{r}) V''^{\mathbf{q}a\gamma,-\mathbf{q}a'\gamma'}_{ext}(\mathbf{r}) + \sum_p \frac{\partial^2 E_{nn}}{\tau_{0a'\gamma'}\tau_{pa\gamma}} e^{i\mathbf{q}\cdot\mathbf{T}_p}. \end{aligned} \tag{3.21}$$

In this last equation, $V_{ext}^{\prime\prime\mathbf{q}a\gamma,-\mathbf{q}a'\gamma'}(\mathbf{r})$ is the second derivative of the external potential with respect to the atomic displacement

$$V_{ext}^{\prime\prime\mathbf{q}a\gamma,-\mathbf{q}a'\gamma'}(\mathbf{r}) = \sum_p e^{i\mathbf{q}(\mathbf{T}_p+\mathbf{R}_a)} e^{-i\mathbf{q}(\mathbf{T}_p+\mathbf{R}_{a'})} \delta_{aa'} \frac{\partial^2 V_a(\mathbf{r}-\mathbf{R}_a+\mathbf{T}_p)}{\partial\tau_{pa\gamma}\partial\tau_{pa\gamma}}. \quad (3.22)$$

3.3 PHONONS IN DENSITY FUNCTIONAL PERTURBATION THEORY

One problem arising from the solution of the dynamical matrix of equation (3.21) is related to the form of the perturbed states of equation (3.19). Here the sum over the index j is performed over all occupied and unoccupied states. In theory, it is then necessary to calculate enough empty states to ensure the convergence of the linear response. This turns out to be an inconvenient process, since one would hope to be able to neglect calculations related to unoccupied states that, being unoccupied, do not carry knowledge in regard to the properties of the ground state of the material.

To work around this issue it is enough to consider the explicit form of first order perturbation theory expressed through the periodic part of the Bloch states as

$$\left(H_{KS}^{\mathbf{k}+\mathbf{q}} + \alpha \sum_{v'} \left|u_{v'\mathbf{k}+\mathbf{q}}\right\rangle\left\langle u_{v'\mathbf{k}+\mathbf{q}}\right| - \epsilon_{v\mathbf{k}}\right)\left|\Delta u_{v\mathbf{k}}^{\mathbf{q}a\gamma}\right\rangle = -\left[1 - \sum_{v'} \left|u_{v'\mathbf{k}+\mathbf{q}}\right\rangle\left\langle u_{v'\mathbf{k}+\mathbf{q}}\right|\right]\Delta v_{KS}^{\mathbf{q}a\gamma} |u_{v\mathbf{k}}(\mathbf{r})\rangle. \quad (3.23)$$

Here α is an arbitrary real parameter and the term $\alpha \sum_{v'} \left|u_{v'\mathbf{k}+\mathbf{q}}\right\rangle\left\langle u_{v'\mathbf{k}+\mathbf{q}}\right|$ is introduced to avoid singularities in the left side of the equation. Additionally, the sum over v' is performed only over all the occupied states and the Hamiltonian operator $H_{KS}^{\mathbf{k}+\mathbf{q}}$ has its coordinate representation [89] defined by the relation

$$H_{KS}^{\mathbf{k}+\mathbf{q}}(\mathbf{r},\mathbf{r}') = e^{-i(\mathbf{k}+\mathbf{q})\cdot\mathbf{r}} H_{KS}(\mathbf{r},\mathbf{r}') e^{i(\mathbf{k}+\mathbf{q})\cdot\mathbf{r}'}. \quad (3.24)$$

Furthermore, the Fourier components of the self consistent Kohn-Sham potential can be expressed as

$$\Delta v_{KS}^{\mathbf{q}a\gamma}(r) = v_{ext}^{\prime\mathbf{q}a\gamma}(r)\tau_{a\gamma}(\mathbf{q}) + \frac{e^2}{4\pi\epsilon_0}\int \frac{\Delta\rho_{\mathbf{q}a\gamma}(\mathbf{r}')}{|\,\mathbf{r}-\mathbf{r}'\,|} e^{i\mathbf{q}\cdot(\mathbf{r}-\mathbf{r}')} d\mathbf{r}' + \frac{dv_{xc}^{[\rho]}(\mathbf{r})}{d\rho(\mathbf{r})}\Delta\rho_{\mathbf{q}a\gamma}(\mathbf{r}). \quad (3.25)$$

The form of the self consistent potential response from equation (3.25), the equation for the induced charge density (3.20), and the form of the

linear response of equation (3.23), are all in a self consistent relationship between each other. In theory, it is possible to self consistently solve this set of equation in the same way as the normal Kohn-Sham system. This procedure comes with two major advantages. First, there is no need to perform summations over empty states and, second, considering that all equations depend on the periodic part of the Bloch states $u_{\mathbf{k},v}(\mathbf{r})$, there is no need to create supercells for the calculations. Therefore, the computational cost of every perturbation $\mathbf{q}$ is always of the same order.

3.4 THE ELECTRON-PHONON INTERACTION

The previous chapter mentioned the limits of the Born-Oppenheimer approximation. Recalling equation (2.9), it was shown that the second and third terms on the right side can be neglected under the condition for which the energies of the states involved in the braket of equation (2.10) (E_k and E'_k) are far apart. Although this condition is well fulfilled in insulators, it clearly breaks down for metals, where, since the electronic bands are not filled, it is possible to have transitions with vanishingly small energy differences. In this case, the terms mentioned above become relevant giving rise to interactions between electrons and phonons that, for instance, alter the nuclear dynamics, produce variations in the particle lifetime, and give rise to the phenomenon of superconductivity [86]. In particular, specific interest is given to the second term of the right side of equation (2.9), as it adds contributions to linear order in the displacement and, between the two, it is the most dominant term.

To work toward a specific form for this electron-phonon interaction term, it is first useful to work in second quantization by defining an electronic field operator $\Psi(\mathbf{r}) = \sum_{i\mathbf{k}} \psi_{i\mathbf{k}}(\mathbf{r}) c_{i\mathbf{k}}$, defining the creation and destruction of an electron at position $\mathbf{r}$. Considering also the DFT formalism in the Kohn-Sham framework, the second term of the right side of equation (2.9) can be written as

$$H_{el-ph} = -\sum_{a\gamma,i\mathbf{k},j\mathbf{k}'} \frac{1}{M_a} c^{+}_{j\mathbf{k}'} c_{i\mathbf{k}} \langle \psi_{j\mathbf{k}'}(\mathbf{r}) \mid P_{a\gamma} \mid \psi_{i\mathbf{k}}(\mathbf{r}) \rangle P_{a\gamma}. \tag{3.26}$$

This equation can be rewritten considering the form of equation (2.10) and expressing the nuclear momentum operator P_a through its normal

coordinate form of equation (3.8). This gives

$$H_{el-ph} = \sum_{\substack{pa\gamma \\ i\mathbf{k},j\mathbf{k}',\nu\mathbf{q}}} \frac{1}{M_a} c^+_{j\mathbf{k}'} c_{i\mathbf{k}} \frac{\left\langle \psi_{j\mathbf{k}'} \right| \frac{\partial V_{KS}}{\partial \tau_{pa\gamma}} \left| \psi_{i\mathbf{k}} \right\rangle}{\epsilon_{jk'} - \epsilon_{ik}} \sqrt{\frac{\hbar M_a \omega_\nu(\mathbf{q})}{2N_p}} e_{a\gamma\nu}(\mathbf{q}) e^{i(\mathbf{q}\cdot\mathbf{T})} (a^+_{\nu-\mathbf{q}} - a_{\nu\mathbf{q}}). \tag{3.27}$$

Taking advantage of the form of the Kohn-Sham Bloch states, the equation can be rewritten through just the periodic part of the wave functions. Imposing the conservation of momentum ($\mathbf{k}' = \mathbf{k}+\mathbf{q}$) and energy ($\epsilon_{jk'} - \epsilon_{ik} = \omega_\nu(\mathbf{q})$) leads to express the electron-phonon Hamiltonian as

$$H_{el-ph} = -\frac{1}{\sqrt{N_p}} \sum_{i\mathbf{k},\nu\mathbf{q},j} c^+_{j\mathbf{k}+\mathbf{q}} c_{i\mathbf{k}} g_{i\mathbf{k},j,\mathbf{q}\nu} (a^+_{\nu-\mathbf{q}} + a_{\nu\mathbf{q}}), \tag{3.28}$$

where $g_{i\mathbf{k},j,\mathbf{q}\nu}$ is the electron phonon coupling parameter of the form

$$g_{i\mathbf{k},j,\mathbf{q}\nu} = \left\langle u_{j\mathbf{k}+\mathbf{q}} \right| \Delta_{\nu\mathbf{q}} v_{KS} \left| u_{i\mathbf{k}} \right\rangle, \tag{3.29}$$

and where the term in the bracket has the form

$$\Delta_{\nu\mathbf{q}} v_{KS} = \sum_{a\gamma} \sqrt{\frac{\hbar}{2\omega_\nu(\mathbf{q}) M_a}} e_{a\gamma\nu}(\mathbf{q}) \sum_p e^{-i\mathbf{q}\cdot(\mathbf{r}-\mathbf{T}_p)} \frac{\partial V_{KS}}{\partial \tau_{a\gamma}}\bigg|_{\mathbf{r}-\mathbf{T}_p}. \tag{3.30}$$

Equation (3.28) describes the processes of interactions between electrons and phonons in which a phonon (a) with momentum $\mathbf{q}$ scatters with an electron (c) with momentum $\mathbf{k}$, generating electron (c^+) in the final state with momentum $\mathbf{k}+\mathbf{q}$. Alternatively, it describes the equivalent process in which an electron (c) of momentum $\mathbf{k}$ emits a phonon (a^+) with momentum $-\mathbf{q}$, generating an electron in the final state (c^+) with momentum $\mathbf{k}+\mathbf{q}$. Finally, on a practical sense, the value of $g_{i\mathbf{k},j,\mathbf{q}\nu}$ can be obtained through the density functional perturbation theory exposed in the previous sections.

3.5 ANHARMONICITY AND QUANTUM EFFECTS

The previous sections discussed why the harmonic approximation of the Born-Oppenheimer energy surface is a reasonable first step toward an accurate description of the atomic vibrations. To recall it, the harmonic approximation introduces a second order expansion of $V(\mathbf{R})$. This expansion holds, in principle, in the limit in which the atomic oscillations around

their equilibrium positions $\mathbf{R}_0$, which arise from quantum and thermal fluctuations, are small. However, there are many circumstances in which this approximation does not produce accurate results. For instance, the harmonic approximation is not able to reproduce the phonons finite lifetime, cannot account for finite thermal conductivity nor the thermal expansion and, at times, it cannot even reproduce the real equilibrium positions of the nuclei.

There is the need to go beyond the harmonic approximation in order to describe these phenomena and introduce an anharmonic description of the system. This is often done through the inclusion of higher order terms of the Taylor expansion of the Born-Oppenheimer energy surface. Usually, these additional terms can be treated trough perturbation theory, but under the assumption that atomic oscillations are small and that high order terms are small compared to the second order one.

These last assumptions do not always hold. Looking at the form of the nuclei displacement equation (3.7), it can be seen that the nuclei displacement depends on the inverse of the nuclei mass and the phonon frequency. In fact, one expects that either in presence of weak interatomic bonds, light atoms or high temperatures, the atomic displacements could lie in highly anharmonic zones of the Born-Oppenheimer energy surfaces. Even at low temperatures, there is always a residual vibrational amplitude due to the zero point motion, arising from the quantum nature of the atoms, and, for light atoms, the harmonic approximation might also break down in this limit.

One possibility to treat strong anharmonicities is to make use of molecular dynamics simulations above Debye temperature [90] or make use of path integral molecular dynamics simulations [91], which however comes at a great computational cost. The latter is also valid in the low temperature quantum limit. Another approach to include both anharmonicity and the quantum nature of the atoms is through the Stochastic Self Consistent Harmonic Approximation (SSCHA) [61–64, 92], which, although being computationally expensive, it is still much more convenient than path integral methods, and is able to offer an (almost) exact description of the vibrational properties of a system for any degree of anharmonicity.

3.6 THE STOCHASTIC SELF CONSISTENT HARMONIC APPROXIMATION

The Stochastic Self Consistent Harmonic Approximation (SSCHA) [62] is a variational approach based on the minimization of the Helmholtz free energy aiming at including the effect of quantum ionic fluctuations and

anharmonicity in the dynamics of the nuclear degrees of freedom. Generally speaking, the nuclear kinetic term of equation (2.12) is neglected in the framework of standard DFT calculations in the harmonic approximation, because the structural and phonon spectra properties are obtained trough the local curvature around the minimum value of the Born-Oppenheimer potential $V(\mathbf{R})$. In contrast, the SSCHA aims to keep the nuclear kinetic contribution of the Hamiltonian and describes the nuclei as quantum particles interacting with the complete form of $V(\mathbf{R})$. This is done under the approximation that the ground state nuclear wave function is Gaussian. Although one could expect that the real ground state wave function differs from the assumption made in the SSCHA, it has been shown that a Gaussian ground state nuclear wave function is a reasonable enough approximation yielding good results even in the most anharmonic cases [62].

The first step toward the SSCHA description is the definition of a harmonic trial Hamiltonian of the form

$$\widetilde{H}_{\boldsymbol{\mathcal{R}},\boldsymbol{\varphi}} = \sum_a -\frac{\hbar^2 \nabla_a^2}{2M_a} + \frac{1}{2}\sum_{ab}(R-\mathcal{R})^a \varphi_{ab} (R-\mathcal{R})^b, \tag{3.31}$$

where $\mathcal{R}$ represents the most probable ionic positions, the centroid positions, φ_{ab} are trial force constants, and where the indexes a and b represents both atoms and Cartesian coordinates. Furthermore, a trial density matrix, restricted to equilibrium density matrices, is defined using the auxiliary Hamiltonian as

$$\widetilde{\rho}_{\boldsymbol{\mathcal{R}},\boldsymbol{\varphi}} = e^{-\beta \widetilde{H}_{\boldsymbol{\mathcal{R}},\boldsymbol{\varphi}}} / tr[e^{-\beta \widetilde{H}_{\boldsymbol{\mathcal{R}},\boldsymbol{\varphi}}}]. \tag{3.32}$$

In this equation $\beta = 1/(k_B T)$ where T is the temperature, and k_B is Boltzmann's constant. The SSCHA free energy is then defined by sampling the "real" Hamiltonian of the system in the Born-Oppenheimer approximation ($H = T_n + V(\mathbf{R})$) defined in equation (2.12) through the auxiliary trial density matrix

$$\mathcal{F}[\widetilde{\rho}_{\boldsymbol{\mathcal{R}},\boldsymbol{\varphi}}] = tr[\widetilde{\rho}_{\boldsymbol{\mathcal{R}},\boldsymbol{\varphi}} H] + \frac{1}{\beta} tr[\widetilde{\rho}_{\boldsymbol{\mathcal{R}},\boldsymbol{\varphi}} ln(\widetilde{\rho}_{\boldsymbol{\mathcal{R}},\boldsymbol{\varphi}})]. \tag{3.33}$$

Due to the validity of the Gibbs-Bogoliubov variational principle, the SSCHA free energy $\mathcal{F}[\widetilde{\rho}_{\boldsymbol{\mathcal{R}},\boldsymbol{\varphi}}]$ will always be greater or equal to the real free energy of the system. The goal would then be to chose the appropriate set of the parameters $\boldsymbol{\mathcal{R}}$ and $\boldsymbol{\varphi}$ that minimize $\mathcal{F}[\widetilde{\rho}_{\boldsymbol{\mathcal{R}},\boldsymbol{\varphi}}]$. The SSCHA performs a minimization procedure where, at each step, the free energy is sampled by generating a set of random ionic configurations according to a Gaussian nuclear probability distribution

$$\widetilde{\rho}_{\boldsymbol{\mathcal{R}},\boldsymbol{\varphi}}(\mathbf{R}) = \sqrt{det\left(\frac{\boldsymbol{\Psi}^{-1}}{2\pi}\right)} e^{-\left[\frac{1}{2}\sum_{a,b}(R-\mathcal{R})^a \Psi_{ab}^{-1} (R-\mathcal{R})^b\right]}, \tag{3.34}$$

where $\mathbf{\Psi}$ is the displacement-displacement correlation matrix of the form:

$$\Psi_{a,b} = \langle u_a u_b \rangle_{\widetilde{\rho}_{\boldsymbol{\mathcal{R}},\boldsymbol{\varphi}}} = \frac{1}{\sqrt{M_a M_b}} \sum_{\nu} \frac{\hbar(2n_\nu + 1)}{2\omega_\nu} e_{a,\nu} e_{b,\nu}. \tag{3.35}$$

In this last equation, the notation $\langle \cdot \rangle_{\widetilde{\rho}_{\boldsymbol{\mathcal{R}},\boldsymbol{\varphi}}}$ stands for the quantum average of the operator $\cdot$ taken with $\widetilde{\rho}_{\boldsymbol{\mathcal{R}},\boldsymbol{\varphi}}$, ω_ν and $\mathbf{e}_\nu$ are respectively eigenvalues and eigenvectors for the mass scaled auxiliary force constants

$$\mathcal{D}^{(2)}_{a,b} = \frac{\phi_{ab}}{\sqrt{M_a M_b}}, \tag{3.36}$$

n_ν represents the Bose-Einstein occupation number for ω_ν and where $u_a = R_a - \mathcal{R}_a$ is the displacement from the average centroid position. Here u_a is different from the ion displacement $\tau_{pa\gamma}$ defined in (3.1). The former is the difference between the atomic position and the centroid position, while the latter is the difference between the atomic position and the local minimum of the Born-Oppenheimer potential.

The minimization strategy implemented in the SSCHA code for the free energy is based on a preconditioned gradient descent. At each step of the minimization both auxiliary force constants ($\boldsymbol{\varphi}$) and auxiliary centroid positions ($\boldsymbol{\mathcal{R}}$) are updated as

$$\varphi^{(n+1)}_{a,b} = \varphi^{(n)}_{a,b} - \lambda_{\boldsymbol{\varphi}} \left\langle \left(f^{(BO)}_b(\mathbf{R}) - f^{\widetilde{H}_{\boldsymbol{\mathcal{R}},\boldsymbol{\varphi}}}_b(\mathbf{R}) \right) \sum_c \Psi^{-1}_{a,c} (R_c - \mathcal{R}_c) \right\rangle_{\widetilde{\rho}_{\boldsymbol{\mathcal{R}},\boldsymbol{\varphi}}}, \tag{3.37}$$

and

$$\mathcal{R}^{(n+1)}_a = \mathcal{R}^{(n)}_{a,b} + \lambda_{\boldsymbol{\mathcal{R}}} \sum_b \varphi^{-1}_{a,b} \left\langle f^{(BO)}_b(\mathbf{R}) - f^{\widetilde{H}_{\boldsymbol{\mathcal{R}},\boldsymbol{\varphi}}}_b(\mathbf{R}) \right\rangle_{\widetilde{\rho}_{\boldsymbol{\mathcal{R}},\boldsymbol{\varphi}}}. \tag{3.38}$$

In these equations $\lambda_{\boldsymbol{\varphi}}$ and $\lambda_{\boldsymbol{\mathcal{R}}}$ are two arbitrary parameters normalized to unity introduced to ensure a safe convergence, $f^{(BO)}_a$ are the forces for the ath atom in the Born-Oppenheimer approximation and where $f^{\widetilde{H}_{\boldsymbol{\mathcal{R}},\boldsymbol{\varphi}}}_b$ are the forces for the bth atom related to the auxiliary Hamiltonan

$$f^{\widetilde{H}_{\boldsymbol{\mathcal{R}},\boldsymbol{\varphi}}}_a(\mathbf{R}) = -\sum_b \varphi_{a,b}(R_b - \mathcal{R}_b). \tag{3.39}$$

The procedure is then repeated until both $\varphi^{(n+1)}_{a,b}$ and $\mathcal{R}^{(n+1)}_a$ reach convergence.

After the minimization, the phonon spectra can be calculated through the second derivative of the free energy as

$$\mathcal{D}^{(F)}_{ab} = \frac{1}{\sqrt{M_a M_b}} \frac{\partial^2 \mathcal{F}}{\partial \mathcal{R}_a \partial \mathcal{R}_b} \bigg|_{\boldsymbol{\mathcal{R}}_{eq}}. \tag{3.40}$$

Here $\boldsymbol{\mathcal{R}}_{eq}$ represents the final ionic equilibrium positions after the SSCHA relaxation, and $\mathcal{D}^{(F)}_{ab}$ is the dynamical matrix of the free energy. The latter is associated to the "free energy phonons" quasi particles, with energies $\hbar\Omega_\mu$, and polarization vectors ϵ^a_μ, obtained by diagonalization as

$$\sum_b \mathcal{D}^{(F)}_{ab}\epsilon^b_\mu = \Omega^2_\mu \epsilon^a_\mu. \tag{3.41}$$

It has been shown that the free energy Hessian can be expressed through an analytic form involving the order equilibrium SSCHA force constants [63]

$$\mathcal{D}^{(n)}_{a_1,a_2,\dots a_n} = \frac{1}{\sqrt{M_{a_1}M_{a_2}\dots M_{a_n}}}\left\langle \frac{\partial^n V(\mathbf{R})}{\partial R_{a_1}\partial R_{a_2}\dots\partial R_{a_n}}\right\rangle_{\widetilde{\rho}_{\boldsymbol{\mathcal{R}},\boldsymbol{\varphi}}}. \tag{3.42}$$

Through this quantity, the SSCHA free energy can be written in a compact form as

$$\frac{\partial^2 \mathcal{F}}{\partial \boldsymbol{\mathcal{R}}\partial\boldsymbol{\mathcal{R}}} = \boldsymbol{\mathcal{D}}^{(2)} + \boldsymbol{\mathcal{D}}^{(3)}\boldsymbol{\Lambda}\left[\frac{1}{1-\boldsymbol{\mathcal{D}}^{(4)}\boldsymbol{\Lambda}}\right]\boldsymbol{\mathcal{D}}^{(3)}. \tag{3.43}$$

In this equation, $\boldsymbol{\Lambda}$ represents a negative defined tensor [63].

Overall, each term appearing in equation (3.43) is a complex object that contains a dependence from the complete features of the Born-Oppenheimer potential $V(\mathbf{R})$ averaged over the density of equation (3.34). This expression is able to specify much about the properties of the SSCHA free energy Hessian matrix. In particular, it is useful to notice that, although $\boldsymbol{\mathcal{D}}^{(2)}$ is positive defined, $\boldsymbol{\mathcal{D}}^{(3)}$ and $\boldsymbol{\mathcal{D}}^{(4)}$ do not necessarily need to be so. This implies that, recalling that the tensor $\boldsymbol{\Lambda}$ is a negative defined quantity, the second term on the right side of equation (3.43) can be negative and can allow for the free energy hessian to have negative eigenvalues. This feature allows the SSCHA to describe the appearance of second order structural phase transitions, even if the auxiliary SSCHA Hamiltonian is harmonic and $\boldsymbol{\mathcal{D}}^{(2)}$ is positive.

As a final note, it is important to mention that, at the end of the SSCHA relaxation, it is also possible to obtain the anharmonic stress tensor $\mathbf{P}$ calculated with the inclusion of both quantum and thermal nuclear fluctuations. This is done by calculating the derivatives of the free energy with respect to a strain tensor $\boldsymbol{\epsilon}$

$$\begin{aligned} P_{\alpha\beta} = -\frac{1}{2\Omega}\frac{\partial \mathcal{F}}{\partial \epsilon_{\alpha\beta}}\bigg|_{\epsilon=0} &= \left\langle P^{(BO)}_{\alpha\beta}(\mathbf{R})\right\rangle_{\bar{\rho}\mathcal{R},\varphi} \\ &\quad - \frac{1}{2\Omega}\sum_{s=1}^{N_a}\left\langle u^\alpha_s f^{(BO)\beta}_s + u^\beta_s f^{(BO)\alpha}_s\right\rangle_{\bar{\rho}\mathcal{R},\varphi}. \end{aligned} \tag{3.44}$$

In this equation Ω is the simulation box volume, and α and β represent the Cartesian coordinates. Additionally, it is possible to perform a lattice relaxation through the use of the stress tensor $\mathbf{P}$. This is done through the generation of a strain for the lattice as

$$\epsilon_{\alpha\beta} = \Omega(P_{\alpha\beta} - P^* \delta_{\alpha\beta}), \tag{3.45}$$

where P^* is the target pressure of the relaxation, and $\delta_{\alpha\beta}$ is the delta function. Through this strain, the lattice parameters $\mathbf{a}_i$ can be updated as

$$a'_{i\alpha} = a_{i\alpha} + \lambda_{\mathbf{a}_i} \sum_{\beta} \epsilon_{\alpha\beta} a_{i\beta}, \tag{3.46}$$

where $\lambda_{\mathbf{a}_i}$ is an updating step.

CHAPTER 4

Conventional Superconductivity

This chapter is dedicated to the theory of superconductivity. Here the appearance of the attractive interaction between electrons and the collapse of the normal state in favor of a bound electronic state are briefly discussed. Furthermore, the BCS theory for superconductivity and the more complete Migdal-Eliashberg theory for determining the critical temperature are also introduced. The chapter closes with the discussion of the the McMillan and Allen-Dynes equations for the estimate of the superconducting critical temperature.

4.1 Attractive potential

The electronic and nuclear problems faced in the previous chapters represent the basic building blocks for problems in condensed matter physics. The two are often considered separately, but it is important to remember they are just a separation of the general Hamiltonian problem. They often result in more than the sum of their single parts and are able to give rise to much more complex and at times counter intuitive phenomena. Few examples are the renormalization of the electronic and phonon spectra, finite particle lifetimes, the appearance of electronic satellite states, or superconductivity [86]. This section will focus on the latter phenomena. Generally speaking, superconductivity is still a not completely understood problem, and, in some cases, cannot be described through a combination

of nuclear and electronic processes. This section however, focuses on highlighting the theory valid whenever superconductivity is well described by electron-phonon interactions.

Regardless of the type of description, the appearance of superconductivity in a material is defined by the appearance of two universal markers below a certain critical temperature: the vanishing electrical resistance and, in case in which the material is in a magnetic field, the expulsion of the latter from its bulk.

In the current state of the art, the most developed theory able to describe the appearance of the superconducting state is the Bardeen-Cooper-Schrieffer theory or often called BCS theory [6]. The main assumption of BCS is the existence of a form of attractive interaction between pairs of electrons able to overcome their reciprocal Coulomb repulsion. Through this interaction, two electrons bind together to form a bosonic unit, named as the Cooper pair.

Considering the jellium model, where the nuclei positive charges are assumed to be uniformly distributed in space [93] allowing to neglect the band index n, a qualitative description for the attractive interaction binding the electrons together can be given considering the Hamiltonian for the system in presence of electron-electron (H_{e-e}) and, retarded electron-phonon (H_{e-ph}) interactions

$$H = H_0 + H_{e-e} + H_{e-ph}. \tag{4.1}$$

In this equation, H_0 is the general non interacting Hamiltonian for both phonons and electrons with spin σ

$$H_0 = \sum_{\mathbf{q}} \hbar\omega(\mathbf{q})\left(a^+_{\mathbf{q}} a_{\mathbf{q}} + \frac{1}{2}\right) + \sum_{\mathbf{k},\sigma} \epsilon_k(\mathbf{k}) c^+_{\mathbf{k}\sigma} c_{\mathbf{k}\sigma}, \tag{4.2}$$

and the electron-electron and the retarded electron-phonon interactions have the forms

$$H_{e-e} = \frac{1}{2\Omega_{cell}} \sum_{\mathbf{q},\mathbf{k}\sigma,\mathbf{k}'\sigma'} V(\mathbf{q}) c^+_{\mathbf{k}+\mathbf{q}\sigma} c^+_{\mathbf{k}'-\mathbf{q}\sigma'} c_{\mathbf{k}'\sigma'} c_{\mathbf{k}\sigma}, \tag{4.3}$$

and

$$H_{e-ph} = \frac{1}{2\Omega} \int_0^\beta d\tilde{t}_2 \sum_{\mathbf{q},\mathbf{k}\sigma,\mathbf{k}'\sigma'} \frac{|\, g_{\mathbf{q}} \,|^2}{\Omega} G^{(0)}(\mathbf{q}, \tilde{t}_i - \tilde{t}_j) \times \\ \times c^+_{\mathbf{k}+\mathbf{q}\sigma}(\tilde{t}_2) c^+_{\mathbf{k}'-\mathbf{q}\sigma'}(\tilde{t}_1) c_{\mathbf{k}'\sigma'}(\tilde{t}_1) c_{\mathbf{k}\sigma}(\tilde{t}_2). \tag{4.4}$$

Here Ω is the volume of the system, $V(\mathbf{q})$ represents the Fourier transform of the Coulomb potential, $\tilde{t}$ defines imaginary time, $G^{(0)}(\mathbf{q}, \tilde{t}_i - \tilde{t}_j)$ is the free phonon propagator and $g_{\mathbf{q}}$ is the electron-phonon matrix element.

An effective interaction can be defined on the unperturbed system after Fourier transforming H_{e-ph} into the time space. Considering the form for the electron-electron and the electron-phonon interactions together, it is possible to write the effective interaction as

$$V_{eff}(\mathbf{q}, iq_n) = V(\mathbf{q}) + \frac{|\, g_{\mathbf{q}} \,|^2}{\Omega} G^{(0)}(\mathbf{q}, iq_n), \tag{4.5}$$

where iq_n represents a Matsubara frequency. Considering that in the jellium model the electron-phonon matrix elements [94, 95] can be expressed in terms of the Coulomb potential and a characteristic phonon frequency ω_c as

$$\frac{|\, g_{\mathbf{q}} \,|^2}{\Omega} = \frac{1}{2} V(\mathbf{q}) \omega_c, \tag{4.6}$$

it is possible to expand the form of $G^{(0)}(\mathbf{q}, iq_n)$ and transform the imaginary frequencies iq_n into real frequencies ω and rewrite the effective interaction as

$$V_{eff}(\mathbf{q}, \omega) = V(\mathbf{q}) \frac{\omega^2}{\omega^2 - \omega_c^2}. \tag{4.7}$$

This final expression highlights that, for frequencies $\omega < \omega_c$, the effective interaction V_{eff} between electrons is negative and therefore it is possible for two electrons to experience an attractive interaction.

4.2 THE COOPER PROBLEM

To understand the consequence of the attractive interaction, it is helpful to consider the problem of a pair of electrons above the Fermi sea interacting with each other through an non retarded attractive potential V [11]. In this model, all but the two electrons are considered to be interacting while the rest of the electrons below the Fermi sea interact with the pair only through Pauli repulsion by preventing it from sinking below the Fermi energy. Under this assumption the orbital wave function of the electronic pair can be written as

$$\Psi(\mathbf{r}_1, \mathbf{r}_2) = \phi_{\mathbf{q}}(\boldsymbol{\rho}) e^{i\mathbf{q}\cdot\mathbf{R}}, \tag{4.8}$$

where $\boldsymbol{\rho} = \mathbf{r}_2 - \mathbf{r}_1$ represents the relative coordinates between the electrons, and the position of the center of mass is described by the coordinate $\mathbf{R} = (\mathbf{r}_2 + \mathbf{r}_1)/2$. The relative coordinate wave function $\phi_{\mathbf{q}}(\boldsymbol{\rho})$ is symmetric in the singlet spin state and asymmetric for the triplet state. To study the lowest

energy state of the wave function it is necessary to consider the case in which $\mathbf{q} = 0$ for the singlet spin state. In this case, the wave function can be expanded through plane waves with coefficients $a_{\mathbf{k}}$ as

$$\Psi(\mathbf{r}_1, \mathbf{r}_2) = \phi(\rho) = \sum_{\mathbf{k}} a_{\mathbf{k}} e^{i\mathbf{k}\cdot\mathbf{r}_1} e^{-i\mathbf{k}\cdot\mathbf{r}_2}. \tag{4.9}$$

This pair wave function is composed by a combination of single particle states with momentum $\mathbf{k}$ and $-\mathbf{k}$. This means it can be interpreted as if the general wave function is composed by a superposition of configurations in which a pair of states $(\mathbf{k}, -\mathbf{k})$ are occupied. The eigenvalues of $\Psi(\mathbf{r}_1, \mathbf{r}_2)$ can then be found through the associated Shrödinger equation for the potential V as

$$(E - H_0)\Psi = V\Psi. \tag{4.10}$$

Here H_0 is the free particle Hamiltonian. Considering a plane wave expansion, the previous Shrödinger equation can be rewritten as

$$(E - 2\epsilon_k)a_{\mathbf{k}} = \sum_{\mathbf{k}'} V_{\mathbf{k},\mathbf{k}'} a_{\mathbf{k}'}, \tag{4.11}$$

where $V_{\mathbf{k},\mathbf{k}'}$ can be expressed through a factorized form

$$V_{\mathbf{k},\mathbf{k}'} = \langle \mathbf{k}, -\mathbf{k}| \, V \, \left|\mathbf{k}', -\mathbf{k}'\right\rangle = \lambda \omega_{\mathbf{k}'} \omega^*_{\mathbf{k}} \tag{4.12}$$

with the assumption that $\omega_{\mathbf{k}}$ has the form

$$\omega_{\mathbf{k}} = \begin{cases} 1 & 0 < \epsilon_{\mathbf{k}} < \omega_c \\ 0 & \text{otherwise} \end{cases} . \tag{4.13}$$

Equation (4.11) can be solved self consistently by substituting in it the form of the potential (4.12) obtaining

$$(E - 2\epsilon_k)a_{\mathbf{k}} = \lambda \omega_{\mathbf{k}} \sum_{\mathbf{k}'} \omega^*_{\mathbf{k}'} a_{\mathbf{k}'} \tag{4.14}$$

and under the assumption that the density of states $N(\epsilon_{\mathbf{k}})$ is slowly varying in the interval $0 < \epsilon_{\mathbf{k}} < \omega_c$ so that it can be approximated as $N(0)$ close to the Fermi energy. As a result the bound state for the electronic pair becomes

$$| E | = \frac{2\omega_c}{exp(\frac{2}{N(0)|\lambda|}) - 1}. \tag{4.15}$$

This result shows that a bound state exists for any arbitrary weak coupling as long as the potential is attractive near the Fermi surface. This

results suggests that whenever two electrons enter this bound state they produce an instability of the normal phase which is associated with the occurrence of superconductivity. The same analysis can be repeated with $\mathbf{q} \neq 0$ or in the case in which the wave function of the system is in the triplet state. What will result is that for $\mathbf{q} \neq 0$ the energy of the bound state will be smaller. This suggests that the pair non zero net momentum will tend to disrupt the bound state. Furthermore, it is possible to have a bound state for the triplet state where the electrons have the same spin and asymmetric wave function. For this to happen however, it is necessary for the potential V to carry momentum [7]. Often however, one can count on the ground state for the pair to be associated with a stationary state ($\mathbf{q} = 0$) and the singlet state wave function with opposite spins.

4.3 REDUCED HAMILTONIAN

In the previous section it was shown the existence of a bound state for a pair of electrons in the presence of an attractive potential, and it was mentioned how the lowest energy state for the bound pair is achieved in the singlet state with center of mass momentum $\mathbf{q} = 0$. In this section instead, a more general description for a system of more than just two electrons is shown. In this case, the general behavior of all particles can be described through an effective reduced Hamiltonian considering only interactions between pairs of electrons with opposite momentum $\mathbf{k}$ and $-\mathbf{k}$ and opposite spin. This reduced Hamiltonian can be expressed in the form

$$\hat{H}_{Red} = \sum_{i\mathbf{k}} \xi_i(\mathbf{k}) c^+_{i\mathbf{k}} c_{i\mathbf{k}} + \sum_{i\mathbf{k},j\mathbf{k}'} V_{ik,jk'} c^+_{i\mathbf{k}\uparrow} c^+_{i-\mathbf{k}\downarrow} c_{j-\mathbf{k}'\downarrow} c_{j\mathbf{k}'\uparrow}. \tag{4.16}$$

In this equation, $\xi_i(\mathbf{k})$ represents the energy of the single particle from the chemical potential:

$$\xi_i(\mathbf{k}) = \epsilon_i(\mathbf{k}) - \mu. \tag{4.17}$$

A simple way to obtain a solution for the reduced Hamiltonian is to assume the validity of the mean field approximation that allows to rewrite the interacting term as

$$\sum_{i\mathbf{k},j\mathbf{k}'} V_{ik,jk'} c^+_{i\mathbf{k}\uparrow} c^+_{i-\mathbf{k}\downarrow} c_{j-\mathbf{k}'\downarrow} c_{j\mathbf{k}'\uparrow} = \sum_{i\mathbf{k},j\mathbf{k}'} V_{ik,jk'} \Big[\langle c^+_{i\mathbf{k}\uparrow} c^+_{i-\mathbf{k}\downarrow} \rangle c_{j-\mathbf{k}'\downarrow} c_{j\mathbf{k}'\uparrow} + \langle c_{j-\mathbf{k}'\downarrow} c_{j\mathbf{k}'\uparrow} \rangle c^+_{i\mathbf{k}\uparrow} c^+_{i-\mathbf{k}\downarrow} - \langle c^+_{i\mathbf{k}\uparrow} c^+_{i-\mathbf{k}\downarrow} \rangle \langle c_{j-\mathbf{k}'\downarrow} c_{j\mathbf{k}'\uparrow} \rangle \Big], \tag{4.18}$$

where in this equation the bracket $\langle\rangle$ represents the grand-canonical thermodynamic average. The reduced Hamiltonian can then be diagonalized

by introducing a transformation in the electronic creation and destruction operators of the form

$$c_{i\mathbf{k}\uparrow} = u^*_{i\mathbf{k}}\gamma_{i\mathbf{k}\uparrow} + v_{i\mathbf{k}}\gamma^+_{i-\mathbf{k}\downarrow}, \tag{4.19}$$

$$c^+_{i-\mathbf{k}\downarrow} = u_{i\mathbf{k}}\gamma^+_{i-\mathbf{k}\downarrow} - v^*_{i\mathbf{k}}\gamma_{i-\mathbf{k}\downarrow}. \tag{4.20}$$

Here, $u_{i\mathbf{k}}$ and $v_{i\mathbf{k}}$ are two normalization constants such that $\mid u_{i\mathbf{k}} \mid^2 + \mid v_{i\mathbf{k}} \mid^2 = 1$. With this transformation, the diagonalized Hamiltonian takes the form

$$H = \sum_{i\mathbf{k},\sigma} E_i(\mathbf{k})\gamma^+_{i\mathbf{k},\sigma}\gamma_{i\mathbf{k},\sigma} + \sum_{i\mathbf{k}}\left(\xi_i(\mathbf{k}) - E_i(\mathbf{k}) + \Delta_{i\mathbf{k}}\langle c^+_{i\mathbf{k}\uparrow}c_{i-\mathbf{k}\downarrow}\rangle\right), \tag{4.21}$$

where $\Delta_{i\mathbf{k}}$ is defined as the gap function

$$\Delta_{i\mathbf{k}} = \sum_{j\mathbf{k}'} V_{i\mathbf{k},j\mathbf{k}'}\langle c_{j-\mathbf{k}'\downarrow}c_{j\mathbf{k}'\uparrow}\rangle, \tag{4.22}$$

and $E_i(\mathbf{k})$ represents the eigenstates of the diagonalized effective Hamiltonian

$$E_i(\mathbf{k}) = \sqrt{\xi_i(\mathbf{k})^2 + \Delta^2_{i\mathbf{k}}}. \tag{4.23}$$

The gap function $\Delta_{i\mathbf{k}}$ is called as such because even at the Fermi level, where $\xi_i(\mathbf{k}) = 0$, the energy spectrum of the superconductor has a gap of size $\mid \Delta_{i\mathbf{k}} \mid$. Thus, the minimum energy of $2 \mid \Delta_{i\mathbf{k}} \mid$ needs to be transmitted to the system in order excite its quasi-particles, which are described by the operators $\gamma_{i\mathbf{k},\sigma}$, and are usually called Bogoliubons. These latter excitations are defined as the inverse transformation of the operators defined in equations (4.19) and (4.20):

$$\gamma_{i\mathbf{k}\uparrow} = u_{i\mathbf{k}}c_{i\mathbf{k}\uparrow} - v_{i\mathbf{k}}c^+_{i-\mathbf{k}\downarrow} \tag{4.24}$$

$$\gamma^+_{i-\mathbf{k}\downarrow} = u^*_{i\mathbf{k}}c^+_{i-\mathbf{k}\downarrow} - v^*_{i\mathbf{k}}c_{i\mathbf{k}\uparrow}. \tag{4.25}$$

The destruction of a Bogoliubons through the application of the operator $\gamma_{i\mathbf{k},\sigma}$ is to be interpreted as the destruction of a single particle electronic state $c_{i\mathbf{k}\uparrow}$ with probability $\mid u_{i\mathbf{k}} \mid^2$ and a creation of a single particle state $c^+_{i-\mathbf{k}\downarrow}$ with probability $\mid v_{i\mathbf{k}} \mid^2$. Additionally, through the diagonalized Hamiltonian of equation (4.21), it is then possible to give an explicit expression for the parameters $u_{i\mathbf{k}}$ and $v_{i\mathbf{k}}$ in the form

$$\mid u_{i\mathbf{k}} \mid^2 = \frac{1}{2}\left(\frac{1}{2} + \frac{\xi_i(\mathbf{k})}{\sqrt{\xi_i(\mathbf{k})^2 + \Delta^2_{i\mathbf{k}}}}\right) \tag{4.26}$$

$$| v_{i\mathbf{k}} |^2 = \frac{1}{2}\left(\frac{1}{2} - \frac{\xi_i(\mathbf{k})}{\sqrt{\xi_i(\mathbf{k})^2 + \Delta_{i\mathbf{k}}^2}}\right). \tag{4.27}$$

A last note is dedicated to the determination of the BCS ground state wave function (Ψ_{BCS}) in terms of the vacuum state. Considering that the main excitation of the BCS theory are the Bogoliubons, the application of the operator $\gamma_{i\mathbf{k}\uparrow}$ on the ground state Ψ_{BCS} will result in the void state

$$\gamma_{i\mathbf{k}\uparrow}|\Psi_{BCS}\rangle = 0. \tag{4.28}$$

It is then possible to write the BCS wave function as an arbitrary combination of Cooper pairs

$$|\Psi_{BCS}\rangle = \mathcal{N}\Pi_{i\mathbf{q}} e^{a_{i\mathbf{q}} c^+_{i\mathbf{q}\uparrow} c^+_{i-\mathbf{q}\downarrow}}|0\rangle, \tag{4.29}$$

where $\mathcal{N}$ represents a normalization constant, and, upon ensuring the proper normalization of the state, one finally obtains

$$|\Psi_{BCS}\rangle = \Pi_{i\mathbf{k}}(u_{i\mathbf{k}} + v_{i\mathbf{k}} c^+_{i\mathbf{k}\uparrow} c^+_{i-\mathbf{k}\downarrow})|0\rangle. \tag{4.30}$$

4.4 MIGDAL-ELIASHBERG FORMALISM

Until now the general features of the BCS theory have been described. However, on a practical sense, one is most interested in the ability to predict the appearance of the superconducting state and, most importantly, the critical temperature (T_c) at which the material becomes superconductor. Currently, one of the most developed methods to obtain such predictions is the first principle self consistent Green's function method based on the Migdal-Eliashberg formalism [13].

The Migdal-Eliashberg theory is formulated within the framework of the Nambu-Gor'kov formalism. In this formalism, one introduces a two-component field operator of the form

$$\mathbf{\Psi}_{i\mathbf{k}} = \begin{bmatrix} c_{i\mathbf{k}\uparrow} \\ c^+_{i-\mathbf{k}\downarrow} \end{bmatrix}, \tag{4.31}$$

and with this operator a generalized matrix Green's function can be introduced

$$\hat{G}_{i\mathbf{k}}(\tilde{t}) = -\langle T_{\tilde{t}} \Psi_{i\mathbf{k}}(\tilde{t}) \Psi^+_{i\mathbf{k}}(0)\rangle. \tag{4.32}$$

Here, $T_{\tilde{t}}$ represents the time ordering operator for the imaginary time $\tilde{t}$ and the braces $\langle\rangle$ indicate the average over the grand-canonical thermodynamic

ensemble. The form of $\hat{G}_{i\mathbf{k}}(\tilde{t})$ can be expanded explicitly to reveal the various components

$$\hat{G}_{i\mathbf{k}}(\tilde{t}) = -\hbar \begin{bmatrix} \langle T_{\tilde{t}} c_{i\mathbf{k}\uparrow}(\tilde{t}) c^{+}_{i\mathbf{k}\uparrow}(0)\rangle & \langle T_{\tilde{t}} c_{i\mathbf{k}\uparrow}(\tilde{t}) c_{i-\mathbf{k}\downarrow}(0)\rangle \\ \langle T_{\tilde{t}} c^{+}_{i-\mathbf{k}\downarrow}(\tilde{t}) c^{+}_{i\mathbf{k}\uparrow}(0)\rangle & \langle T_{\tilde{t}} c^{+}_{i-\mathbf{k}\downarrow}(\tilde{t}) c^{+}_{i-\mathbf{k}\downarrow}(0)\rangle \end{bmatrix}. \tag{4.33}$$

In this equation, the diagonal elements correspond to the normal Green's functions for electrons while the off-diagonal elements describe the Gor'kov's anomalous green's functions. These functions are related with the dynamics of the Cooper pairs seen in the previous sections and to the superconducting energy gap. Furthermore, the general Green's function is periodic in the imaginary time and can, therefore, be expanded through Fourier series

$$\hat{G}_{i\mathbf{k}}(\tilde{t}) = k_B T \sum_{i\omega_n} e^{i\omega_n \tilde{t}} \hat{G}_{i\mathbf{k}}(i\omega_n), \tag{4.34}$$

where $i\omega_n$ reprenents the Matsubara freequencies for fermions, T is the absolute temperature and k_B is Boltzmann's constant. In Fourier space, the general Green function can be expressed as

$$\hat{G}_{i\mathbf{k}}(i\omega_n) = -\begin{bmatrix} G_{i\mathbf{k}}(i\omega_n) & F_{i\mathbf{k}}(i\omega_n) \\ F^{*}_{i\mathbf{k}}(i\omega_n) & -G_{i-\mathbf{k}}(i\omega_n) \end{bmatrix}. \tag{4.35}$$

In the Migdal-Eliashberg formalism, one aims to study the behavior of the self-energy of the general Green's function with the temperature. To practically achieve this, one is to remember that the general Green's function can be expressed in term of the self energy as

$$\hat{G}^{-1}_{i\mathbf{k}}(i\omega_n) = (\hat{G}^{(0)}_{i\mathbf{k}}(i\omega_n))^{-1} - \hat{\Sigma}_{i\mathbf{k}}(i\omega_n). \tag{4.36}$$

As shown before, in order to describe the appearance of the superconducting state it is sufficient to consider in the self energy just the interactions coming from the the electron-phonon pairing ($\hat{\Sigma}^{el-ph}_{i\mathbf{k}}(i\omega_n)$), called Fan-Migdal self energy, and the Coulomb interaction ($\hat{\Sigma}^{e-e}_{i\mathbf{k}}(i\omega_n)$) in the GW approximation [86]. The general self energy can then be rewritten as the sum of the two terms

$$\hat{\Sigma}_{i\mathbf{k}}(i\omega_n) = \hat{\Sigma}^{e-e}_{i\mathbf{k}}(i\omega_n) + \hat{\Sigma}^{el-ph}_{i\mathbf{k}}(i\omega_n), \tag{4.37}$$

where each term has the form

$$\hat{\Sigma}^{el-ph}_{i\mathbf{k}}(i\omega_n) = -k_B T \sum_{j\mathbf{k}',n'} \hat{\sigma}_3 \hat{G}_{j\mathbf{k}'}(i\omega_{n'}) \hat{\sigma}_3 \sum_{\nu} |g_{i\mathbf{k},j\mathbf{k}',\nu}|^2 D_{\nu\mathbf{k}-\mathbf{k}'}(i\omega_n - i\omega_{n'}), \tag{4.38}$$

and

$$\hat{\Sigma}^{e-e}_{i\mathbf{k}}(i\omega_n) = -k_B T \sum_{j\mathbf{k}'n'} \hat{\sigma}_3 \hat{G}^{od}_{j\mathbf{k}'}(i\omega_{n'})\hat{\sigma}_3 V_{i\mathbf{k},j\mathbf{k}'}. \tag{4.39}$$

In the equation for $\hat{\Sigma}^{el-ph}_{i\mathbf{k}}(i\omega_n)$ the quantity $D_{\nu\mathbf{k}-\mathbf{k}'}(i\omega_n - i\omega_{n'})$ represents the phonon propagator of the form

$$D_{\nu\mathbf{q}}(i\omega_n - i\omega_{n'}) = \frac{2\omega_\nu(\mathbf{q})}{(i\omega_n - i\omega_{n'})^2 - \omega^2_\nu(\mathbf{q})}, \tag{4.40}$$

while, in the equation for $\hat{\Sigma}^{el-el}_{i\mathbf{k}}(i\omega_n)$, $\hat{G}^{od}_{j\mathbf{k}'}(i\omega_{n'})$ represents the off diagonal components of the green function and $V_{i\mathbf{k},j\mathbf{k}'}$ represents the matrix elements of the screened Coulomb interaction.

To properly obtain a practical solution to the Green's function, it is useful to consider that the self energy can commonly be rewritten in terms of the mass enhancement parameter ($Z_{i\mathbf{k}}(i\omega_n)$), the electronic energy shift ($\chi_{i\mathbf{k}}(i\omega_n)$), and the superconducting gap ($\Delta_{i\mathbf{k}}(i\omega_n)$) as

$$\hat{\Sigma}_{i\mathbf{k}}(i\omega_n) = i\omega_n\Big[1 - Z_{i\mathbf{k}}(i\omega_n)\Big]\hat{\sigma}_0 + \chi_{i\mathbf{k}}(i\omega_n)\hat{\sigma}_3 + \Delta_{i\mathbf{k}}(i\omega_n)Z_{i\mathbf{k}}(i\omega_n)\hat{\sigma}_1. \tag{4.41}$$

Two different definitions for the electronic self energy have been considered at this point. The latter equation for the self energy can be substituted in the form of the Green's function so to obtain

$$\begin{aligned}&\hat{G}_{i\mathbf{k}}(i\omega_n) = \\ &-\Big\{i\omega_n Z_{i\mathbf{k}}(i\omega_n)\hat{\sigma}_0 + \Big[\epsilon_{i\mathbf{k}} - \epsilon_F + \chi_{i\mathbf{k}}(i\omega_n)\Big]\hat{\sigma}_3 + \Delta_{i\mathbf{k}}(i\omega_n)Z_{i\mathbf{k}}(i\omega_n)\hat{\sigma}_1\Big\}/\Theta_{i\mathbf{k}}(i\omega_n),\end{aligned} \tag{4.42}$$

where $\Theta_{i\mathbf{k}}(i\omega_n)$ has the form

$$\Theta_{i\mathbf{k}}(i\omega_n) = \Big[\omega_n Z_{i\mathbf{k}}(i\omega_n)\Big]^2 + \Big[\epsilon_{i\mathbf{k}} - \epsilon_F + \chi_{i\mathbf{k}}(i\omega_n)\Big]^2 + \Big[\Delta_{i\mathbf{k}}(i\omega_n)Z_{i\mathbf{k}}(i\omega_n)\Big]^2. \tag{4.43}$$

Finally equation (4.42) can be substituted into the form of the self energy of equation (4.37) and equated to (4.41). The resulting equality can be then separated in a set of three anisotropic equations by equating the scalar coefficients

$$Z_{i\mathbf{k}}(i\omega_n) = 1 + \frac{\pi k_B T}{\omega_n N_F} \sum_{j\mathbf{k}'n'} \frac{\omega_{n'} Z_{j\mathbf{k}'}(i\omega_{n'})}{\Theta_{j\mathbf{k}'}(i\omega_{n'})} \lambda_{i\mathbf{k},j\mathbf{k}'}(n - n'), \tag{4.44}$$

$$\chi_{i\mathbf{k}}(i\omega_n) = -\frac{\pi k_B T}{N_F} \sum_{j\mathbf{k}'n'} \frac{\epsilon_{j\mathbf{k}'} - \epsilon_F + \chi_{j\mathbf{k}'}(i\omega_{n'})}{\Theta_{j\mathbf{k}'}(i\omega_{n'})} \lambda_{i\mathbf{k},j\mathbf{k}'}(n-n'), \tag{4.45}$$

$$\Delta_{i\mathbf{k}}(i\omega_n)Z_{i\mathbf{k}}(i\omega_n) = \frac{\pi k_B T}{N_F} \sum_{j\mathbf{k}'n'} \frac{\Delta_{j\mathbf{k}'}(i\omega_{n'})Z_{j\mathbf{k}'}(i\omega_{n'})}{\Theta_{j\mathbf{k}'}(i\omega_{n'})} \left[\lambda_{i\mathbf{k},j\mathbf{k}'}(n-n') - N_F V_{i\mathbf{k},j\mathbf{k}'}\right]. \tag{4.46}$$

In this set of equations N_F is the electronic density of states per spin at the Fermi energy and $\lambda_{i\mathbf{k},j\mathbf{k}'}(n-n')$ is the anisotropic electron phonon coupling

$$\lambda_{i\mathbf{k},j\mathbf{k}'}(n-n') = \int_0^\infty d\omega \frac{2\omega}{(\omega_n - \omega_{n'})^2 + \omega^2} \alpha^2 F_{i\mathbf{k},j\mathbf{k}'}(\omega), \tag{4.47}$$

where $\alpha^2 F_{i\mathbf{k},j\mathbf{k}'}(\omega)$ is the electron-phonon spectral function

$$\alpha^2 F_{i\mathbf{k},j\mathbf{k}'}(\omega) = N_F \sum_\nu |g_{i\mathbf{k},j\mathbf{k}',\nu}|^2 \delta(\omega - \omega_{\mathbf{k}-\mathbf{k}',\nu}). \tag{4.48}$$

The set of three equations (4.44), (4.45) and (4.46) can then be solved through a self consistent loop for each temperature T.

4.4.1 *Approximations*

Looking at equations (4.44) and (4.46) one can see that a trivial solution is $\Delta_{i\mathbf{k}}(i\omega_n) = 0$ for every T. In order to define the superconducting critical temperature one is however interested in the highest value of T for which the two equations admit solutions with $\Delta_{i\mathbf{k}}(i\omega_n) \neq 0$. To properly obtain this solution, it is necessary to introduce some simplifications in the set of equations (4.44),(4.45) and (4.46). To start, it is useful to consider that the superconducting pairing occurs in a small window of energy around the Fermi level (ϵ_F) of the size of the characteristic phonon frequency of the system ω_c. The first simplification is then to restrict the description of the Eliashberg equations near the Fermi energy. This is achieved by arbitrarily introducing the term $\int_{-\infty}^{\infty} d\epsilon' \delta(\epsilon_{j\mathbf{k}'} - \epsilon') = 1$ on the right side of equations (4.44),(4.45),(4.46). This approximation leads to the energy shift $\chi_{i\mathbf{k}}(i\omega_n) = 0$ and simplifies the form of the two remaining equations as

$$Z_{i\mathbf{k}}(i\omega_n) = 1 + \frac{\pi k_B T}{\omega_n N_F} \sum_{j\mathbf{k}'n'} \frac{\omega_{n'}}{\sqrt{\omega_{n'}^2 + \Delta_{j\mathbf{k}'}^2(i\omega_{n'})}} \lambda_{i\mathbf{k},j\mathbf{k}'}(n-n')\delta(\epsilon_{j\mathbf{k}'} - \epsilon_F), \tag{4.49}$$

and

$$\Delta_{i\mathbf{k}}(i\omega_n)Z_{i\mathbf{k}}(i\omega_n) = \frac{\pi k_B T}{N_F}\sum_{j\mathbf{k}'n'}\frac{\Delta_{j\mathbf{k}'}(i\omega_{n'})}{\sqrt{\omega_{n'}^2+\Delta_{j\mathbf{k}'}^2(i\omega_{n'})}} \times\left[\lambda_{i\mathbf{k},j\mathbf{k}'}(n-n') - N_F V_{i\mathbf{k},j\mathbf{k}'}\right]\delta(\epsilon_{j\mathbf{k}'}-\epsilon_F). \quad (4.50)$$

Two additional approximations lie on the introduction of a cutoff for the Matsubara frequencies ω_c which is usually of the order of 1 eV, and the introduction of a dimensionless Coulomb interaction parameter μ_c defined as

$$\mu_c = N_F\langle\langle V_{i\mathbf{k},j\mathbf{k}'}\rangle\rangle. \quad (4.51)$$

Here the double bracket $\langle\langle\cdot\rangle\rangle$ stands for the average on the Fermi surface. One can then rewrite the Coulomb interaction by performing the sum over the Matsubara frequencies as

$$\mu^* = \frac{\mu_c}{1+\mu_c ln(\epsilon_F/\omega_c)}. \quad (4.52)$$

This parameter is usually assumed in a range between 0.1 and 0.15.

For conventional bulk materials, where the anisotropy is weak, it is possible to further simplify the form of equations (4.44) and (4.46) by assuming the presence of a single isotropic band at the Fermi surface, so that both $\Delta_{i\mathbf{k}}$ and $Z_{i\mathbf{k}}$ loose the dependence from the band index i and the quasimomentum $\mathbf{k}$. Under these conditions, the formulation for Migdal-Eliashberg equations is described by a set of simplified isotropic equations as

$$Z(i\omega_n) = 1+\frac{\pi k_B T}{\omega_n}\sum_{n'}\frac{\omega_{n'}}{\sqrt{\omega_{n'}^2+\Delta^2(i\omega_{n'})}}\lambda(n-n'), \quad (4.53)$$

$$Z(i\omega_n)\Delta(i\omega_n) = \pi k_B T\sum_{n'}\frac{\Delta(i\omega_{n'})}{\sqrt{\omega_{n'}^2+\Delta^2(i\omega_{n'})}}\left[\lambda(n-n')-\mu_c^*\right], \quad (4.54)$$

$$\lambda(n-n') = \int_0^\infty d\omega\frac{2\omega}{(\omega_n-\omega_{n'})^2+\omega^2}\alpha^2F(\omega), \quad (4.55)$$

$$\alpha^2F(\omega) = \frac{1}{N_F}\sum_{\mathbf{k},\mathbf{k}'}\delta(\epsilon_{\mathbf{k}}-\epsilon_F)\delta(\epsilon_{\mathbf{k}'}-\epsilon_F)\alpha^2F_{\mathbf{k},\mathbf{k}'}(\omega). \quad (4.56)$$

4.5 MCMILLAN TYPE EQUATIONS

Another simple way to estimate the value of the superconducting critical temperature is through the simple analytic McMillan equation. The latter was obtained by solving the Eliashberg equations by fitting a large set of results obtained using the spectral function of lead [96]. The most modern version of this equation [97] has the form

$$T_c = \frac{\omega_{log}}{1.2} e^{-\frac{1.04(1+\lambda)}{\lambda - \mu_c^*(1+0.62\lambda)}}, \tag{4.57}$$

where ω_{log} is a logarithmic average phonon frequency that aims to describe more generally the characteristic phonon frequency of the system with the form

$$\omega_{log} = e^{\frac{2}{\lambda}\int_0^\infty d\omega \frac{\alpha^2 F(\omega)}{\omega} ln(\omega)}, \tag{4.58}$$

and where $\lambda = \lambda(0)$ is the zero frequency electron-phonon coupling with the form

$$\lambda = 2\int_0^\infty d\omega \frac{\alpha^2 F(\omega)}{\omega}. \tag{4.59}$$

This equation has proven to be accurate for low values of λ, but deviates from the Migdal-Eliashberg results whenever $\lambda > 1$. Above this value it tends to underestimate the value of the superconducting critical temperature. In this regime, a more accurate estimation for the value of the critical temperature was introduced by Allen and Dynes [98], who modified the McMillan equation as

$$T_c = \frac{f_1 f_2 \omega_{log}}{1.2} e^{-\frac{1.04(1+\lambda)}{\lambda - \mu^*(1+0.62\lambda)}}, \tag{4.60}$$

where f_1 and f_2 are two prefactors

$$f_1 = \left[1 + \left(\frac{\lambda}{2.46(1+3.8\mu^*)}\right)^{\frac{3}{2}}\right]^{\frac{1}{3}}, \tag{4.61}$$

$$f_2 = 1 + \frac{(\bar{\omega}_2/\omega_{log} - 1)\lambda^2}{\lambda^2 + \left[1.82(1+6.3\mu^*)(\bar{\omega}_2/\omega_{log})\right]^2}, \tag{4.62}$$

and where $\bar{\omega}_2$ is an additional parameter calculated as

$$\bar{\omega}_2 = \left[\frac{2}{\lambda}\int d\omega \alpha^2 F(\omega)\omega\right]^{\frac{1}{2}}. \tag{4.63}$$

Equation (4.60) results much more accurate with respect to the McMillan form and the results it obtains are close to the isotropic Migdal-Eliashberg values for $\lambda < 2$.

II

General properties of hydrogen based superconductors

CHAPTER 5

Classification and correlations for hydrogen based superconductors

This chapter exposes the results obtained for an analysis of the electronical properties of a large set of hydrogen based superconductors. Here, a classification based on interatomic bonding properties is introduced and correlations with the critical temperature are tested against variables such as density of state, atomic composition, effective atomic charge and interatomic distances.

5.1 Overview

In recent years, the proliferation of computational resources and the development of ab initio methods based on density functional theory have drastically boosted the possibility of performing theoretical predictions from first principles. In regard to the field of hydrogen based superconductivity, some experimental discoveries have been anticipated by DFT calculations [19, 51], proving the predictive power of the current computational methods. Furthermore, with the appearance of structural prediction methods, it now exists a rich data set of predicted superconductors in the order of the hundreds. With this growing set of structures, it now becomes

possible to attempt identifying general trends that could possibly suggest the specific features giving rise to a good superconductor. This opens the possibly to pave a path for more accurate predictions and discoveries for the future. The set of available structures also allows for the application of machine learning algorithms [52–54], which could ulteriorly boost the possibility for further predictions. It is clear at this stage that with all these available tools, it starts to become possible to perform general broad analysis aiming at defining relevant features that could narrow down the search for better superconductors.

This chapter reports a broad analysis performed through ab initio methods based on density functional theory over a set of 178 binary hydrogen based superconductors previously predicted in the literature. Here, the main focus lies on taking advantage of the previous predictions for hydrogen superconductors and prove a simple understanding of the origin of the high T_c for this class of compounds. The analysis focuses mainly on the electronic and structural properties by means of chemical bonding descriptors, hydrogen–hydrogen distance, electronic charge, and density of states at the Fermi level.

5.2 METHODS FOR THE CALCULATIONS

To perform the analysis, a sample of 178 hydrogen based superconductors previously predicted in the literature was selected. Most of the chosen compounds are those summarized in reference [99], which had been analyzed before in the literature [30, 32, 35, 45, 47, 60, 100–179]. The references and data used in this study of each compound are reported in Appendix A.1. Throughout this and the next chapter, each compound is labeled by an index going from 0 to 178 accordingly with the tables reported in the appendix. For each compound a classical relaxation of the structure was performed minimizing the forces at the reported pressure in the literature through DFT. All the calculations were performed through the plane wave Quantum ESPRESSO package [180, 181] using the Perdew-Burke-Ernzerhof parametrization [182] of the exchange-correlation potential. The PAW pseudopotentials used where selected by making sure the cutoff radius would allow to include at least the first upper core orbitals for each atom in the materials. Such choice was necessary due to the extreme pressures, in the order of hundreds of GPa, at which the compounds where predicted to be stable. Furthermore, an energy cutoff of 70 Ry was chosen for the set of Kohn-Shan wave functions and a cutoff of 700 Ry was chosen for the electronic density. The energy cutoff for the wave functions is related to the square of the wavevector $\mathbf{k}$ for the set of Kohn-Shan states of equation (2.56). The integrations over the reciprocal lattice cell were performed

through Methfessel-Paxton smearing technique [81], with an integration broadening of 0.02 Ry and with a reciprocal space grid where each point occupied a volume of 0.0002 $Å^{-3}$ for the self consistent calculations, and 0.0001 $Å^{-3}$ for the non self consistent calculations. The electronic properties such as the electron localization function, the density of states, and the charge distribution were calculated for each system using the Quantum ESPRESSO post-processing tools through the results obtained for the non self-consistent calculations. To determine the charge associated to the atoms, the method proposed by Bader [183] and coworkers was used. The Bader method makes use of density surfaces of the system and identifies zones of maximum value separated by zero gradient surfaces. This allows to determine the charge around the atoms by mere integration of the electron density within their associated region of space. Since these regions are non overlapping, the charges have the advantageous property of being additive. Finally, the values of the superconducting critical temperatures where taken from the literature and were not recalculated due to the high computational cost.

Among the 178 compounds, a subset 43 had to be discarded due to issues related to lack of information about the atomic structure or impossibility to achieve convergence in the self consistent calculations, making impossible to perform their electronical analysis.

5.3 CHEMICAL COMPOSITION AND BONDING CATEGORIES

This section reports the categorization based on the chemical bonding properties for the set of chosen compounds. Such categorization is based on the bonding patterns of the hydrogen atoms in the system, and is guided by the study of the electron localization function and the atomic charge distribution obtained through the Bader method.

After the analysis of the electron localization function for all the compounds, the categorization was organized into six different families related to the different behavior of the hydrogen atoms in the systems. Such families are for molecular systems, covalent systems, systems driven by weak covalent hydrogen-hydrogen interactions, systems with electride behavior, ionic systems, and isolated systems. In each case, the nature of the bonds is identified through the analysis of the electron localization function saddle points separating the attractors between different atoms. It is important to stress out that the bonds between atoms are mainly a local property as their features appear on the scale of the interatomic distances. It is therefore possible that each system belongs to more than just one family and that intricate transition patterns can appear for systems classifiable at the boundary between two different families. Although these effects have

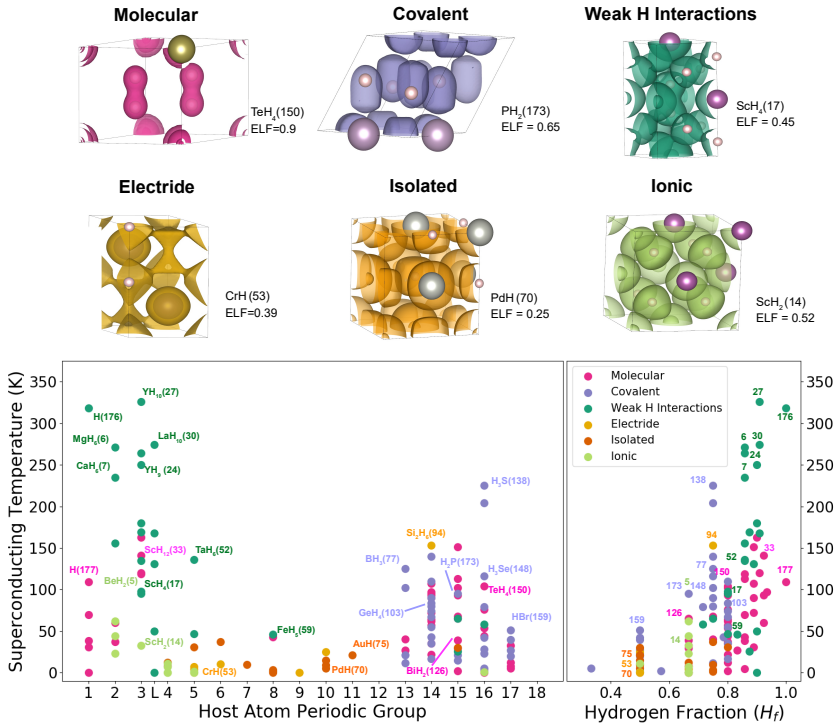

FIGURE 5.1 – The upper panel of the figure shows a representative system for each of the different categories and its charatteristic electron localization function isosurface. Respectively the systems are: TeH_4 for molecular systems (magenta), PH_2 for covalent systems (purple), ScH_4 for weak covalent hydrogen-hydrogen interactions (dark green), CrH for electrides (yellow), PdH for isolated systems (orange), and ScH_2 for ionic systems (light green). The lower panel shows instead the critical temperature as a function of the host atom periodic group (left) and the hydrogen fraction in the compounds (right).

been considered and will be briefly discussed in this section, in order to simplify the analysis, the focus goes on the most dominant family for each compound. A representative for each family, together with the distribution of the families through the groups of the periodic table and the amount of hydrogen fraction in each case, is shown in figure 5.1. In this framework, the hydrogen fraction is defined as the number of hydrogen atoms (N_H) divided by the total number of atoms ($N_X + N_H$) in the unit cell of the material, where N_X is the number of non hydrogen atoms:

$$H_f = \frac{N_H}{N_H + N_X}. \tag{5.1}$$

The system being part of the molecular family are all systems having

at least one pair of hydrogen atoms forming a molecule. The latter can be identified through the electron localization function analysis by locating an isosurface surrounding an isolated molecule at very high values of the electron localization function. An example of a molecular system is shown in figure 5.1 and is TeH_4(150), where the electron localization function isosurfaces are reported in magenta. A system is chosen to be molecular if an isolated pair of hydrogen atoms appears connected at a value of the electron localization function higher than 0.85, i.e., if the minimum electron localization function value in between the hydrogen atoms is above 0.85. The threshold for the appearance of a molecular unit has been chosen arbitrarily after looking at the general behavior of the electron localization function for two closest neighboring hydrogen atoms. It was noticed that the value of the electron localization function at the middle point between two bonded hydrogen atoms decreases linearly with the bonding distance. Systems with molecular behavior appear between groups 1 to 4 and 13 to 17 of the periodic table, and for high values of H_f, thus, in most cases, several molecules exist per host atom as can be seen from figure 5.1. The highest critical temperatures for molecular compounds have been predicted for ScH_{12}(33) and TeH_4(150), with T_c values around 150 K. Overall the critical temperatures in presence of molecular units span from few Kelvin to high values of the order of 100 K.

In the covalent family, all systems where covalent bonds between hydrogen and host atoms are dominant are included. Considering that in the set of chosen compounds only binary systems are included, by host atom here is intended the non hydrogen atom of the binary composition. In the framework of this discussion, the host atom will be labeled as X, with X≠H. For H-X bonds, the covalent character can be identified by an elongation towards the host atom of the electron localization function isosurfaces surrounding the hydrogen as in polarized covalent bonds. This is exemplified by the purple surfaces pointing from the H (small spheres) to the P atoms (big spheres) in PH_2 in figure 5.1. Covalent systems appear for groups 13 to 17 of the periodic table as shown in figure 5.1, and are mostly related to the *p* type orbital character of host atoms. Some of the highest critical temperature for these systems have been predicted for H_3S(138) at 200 K, BH_3(77) at 125 K, and H_3Se(148) at 110 K.

Another family is for the weak covalent hydrogen-hydrogen interaction compounds. It is dominated by compounds with predominant weak H-H covalent interactions. In contrast to the molecular family, here the hydrogen molecules or hydrogen clusters appear elongated or quasi dissociated. This is illustrated with the dark green surfaces in ScH_4 in figure 5.1, where bonds between hydrogen atoms appear at much lower values of the electron localization function. From a quantitative point of view, we

assume that a group of hydrogen atoms is weakly bonded if the electron localization function at the bond point is within the range [0.4 - 0.85]. As for the molecular family, this range of values has been chosen arbitrarily. These systems mostly appear between groups 1 to 5. In this bonding type, interactions seem to be purely related to hydrogen atoms whilst the host atoms appear as inert, or acting as a chemical pre-compressor, or electron donor. Recent literature pointed out that in this kind of compounds the hydrogen atoms tend be located on the host atom sub lattice interstitial bonding sites, or, otherwise, on the valence cloud of electrons as for the the case of transition metals and lanthanides sublattices [184, 185]. The compounds of this family tend to contain many hydrogen atoms per host, as it happens for the molecular compounds. For compounds with the host atom in a low group of the periodic table, the host atoms valence electrons are donated to the hydrogen atoms resulting in a weakening of the H-H bonds. This eventually translates into an increment of the H-H distance. This family shows the highest predicted critical temperatures, the highest being 326 K for YH_{10}(27) and 300 K for metallic hydrogen H(76).

The next family is for the ionic compounds. It includes those systems whose hydrogen atoms show a strong ionic character. The latter is identified by an isolated proto-spherical electron localization function isosurface surrounding the hydrogen. In addition, for a system to be hereby considered as ionic the mean extra charge per hydrogen atom must be more than 0.5 electrons. Once again this threshold was chosen arbitrarily. This is illustrated by the spherical light green surfaces around hydrogen in ScH_2 in figure 5.1, where the extra charge on H is 0.67 electrons. Ionic behavior was observed between groups 2 to 5 of the periodic table, in all cases with low values of H_f. The ionic bonding originates from the strong difference in electronegativity between host and hydrogen atoms, which is always increased under pressure [186]. Critical temperatures for these systems are low, with the highest being 45 K for BeH_2(4).

The electride family contains systems featuring electride behavior, i.e. compounds with electrons localized in the voids or interstitial sites between atoms. The latter can be identified by isolated pockets of localized electrons in empty space of the crystal as the ones shown for CrH in figure 5.1. From a quantitative viewpoint, electride behavior is characterized in terms of isolated isosurfaces not surrounding any nuclei with electron localization function maximum values in between 0.35 to 0.7. Note that metallic compounds are also included in this family. Metallic cases also show isolated bubbles of electron localization function occupying the voids, but their profile is flatter. Given the difficulties to set a quantitative barrier, the two type of compounds have been merged in this unique family. Electrides and metals appear mainly between groups 5 and 10, and are among the systems

with the lowest value of H_f, reaching a maximum of 3 hydrogen atoms per host ($H_f = 0.75$). Critical temperatures for this family are low, not reaching above 50 K, exception made for Si_2H_6(94) with a T_c of 153 K which also shows covalent features.

The last family includes all materials featuring extremely weak bonds between hydrogen and host atoms. These systems have been named as isolated and are identified by the lack of any kind of connection of the electron localization function isosurfaces above 0.25. These systems feature low critical temperatures not reaching above 40 K and appear mainly between groups 5 and 12 of the periodic table. They also show a weak capacity of hosting a large number of H atoms per X atom.

Overall, the results of this investigation highlight that characterizing the bonding type of a solid thanks to these families enables to discard a great number of compounds as potential high-T_c compounds. Covalent interactions, where electrons are strongly localized, be it weak H-H or X-H, are the most favorable for high-temperature superconductivity. This allows to identify the potential interesting combination of elements, especially with respect to the increasing search among ternary compounds. The lowest T_c values appear for electrides and isolated compounds, mostly present between groups 5 and 12, which do not show lots of potential as high-T_c compounds. These families also show the lowest values of H_f. The highest critical temperatures appear between groups 1 and 5 of the periodic table, where bonds are mainly driven by covalent hydrogen-hydrogen interactions, and 13 and 16, where covalent bonds are predominantly between hydrogen and host atoms. From this work emerges that the molecular family transitions towards the weak covalent hydrogen-hydrogen interaction one, with an associated increase in T_c. The transition is smooth, starting from low T_c systems with only hydrogen molecules, such as H_4I(164), going then through a mixed phase where molecules expand and inter molecular H-H interactions start to be present, as for ScH_9(31) and ScH_7(34), to finally transition towards a full weak interacting behavior with no molecules, as found for YH_{10}(27) and LaH_{10}(30), having the largest T_c. A similar transition pattern appears for the ionic compounds. With the increment of H_f the ionic class transitions towards the weak hydrogen-hydrogen interaction one due to the less doping of electrons per hydrogen atom. Similarly, the covalent family as well transitions towards the weak hydrogen-hydrogen interaction one with the increment of H_f. This behavior is due to the limited amount of X-H covalent bonds that the elements between groups 13 to 17 can form. With the increment of H_f the X-H bonds saturate and consequently H-H interactions start to emerge.

From this (de)localization analysis, it appears that systems with high T_c show localized electrons, defined by high electron localization function

maxima, but with a high probability of being coupled, observed through high values of electron localization function saddle points. This suggests that stretching hydrogen molecules is beneficial for superconductivity. The same conclusion is reached looking at the two pure hydrogen phases studied here (systems 176 and 177). The hydrogen phase ascribed to the weak covalent hydrogen-hydrogen interaction behavior (176) shows a far higher T_c of around 300 K compared to the purely molecular phase (177), with T_c = 109 K. Therefore, stretching hydrogen molecules by chemical or mechanical means in systems containing many H_2 units seems a very promising path to discovering new high-T_c compounds. This seems to put in context the extraordinary prediction of a critical temperature of 473 K in Li_2MgH_{16} [39], where doping a molecular MgH_{16} compound with Li brakes the molecular units, transforming the system into one with weak covalent hydrogen-hydrogen interactions.

5.4 HYDROGEN-HYDROGEN DISTANCE AND ELECTRONIC PROPERTIES

This section proposes an analysis of the the trends of the predicted T_c with respect to the structural and electronic properties for the set of hydrogen based superconductors. This analysis focuses on the shortest hydrogen-hydrogen distance for each compound, the charge distribution on hydrogen atoms, and the density of states at the Fermi level. The ultimate goal is to find correlations between such descriptors and the critical temperature. The results are summarized in figure 5.2 and, even if no strong correlation has been found between the chosen descriptors and the critical temperature, several conclusions can be drawn.

The structural analysis related to the shortest hydrogen-hydrogen distance highlights an increment of the superconducting critical temperature with the increment of the distance for those systems where the bonding is driven by pure hydrogen interactions, i.e. the molecular and weak covalent hydrogen-hydrogen interaction families. For these two families the H-H distance spans from 0.74 Å for systems with T_c below 1 K to a maximum of around 1.35 Å for compounds with the highest critical temperatures. In the region between 0.9 and 1.35 Å lie the currently predicted compounds with the highest superconducting temperatures reaching values as high as 300 K. In other words, elongated H-H interactions promote T_c. However, above distances of 1.35 Å the bonds between the hydrogen atoms become too weak to be considered covalent. In this zone, no value higher than 0.4 has been found for the value of the electron localization function at the mid point of the H-H bond. This suggests that effectively above 1.35 Å the H-H

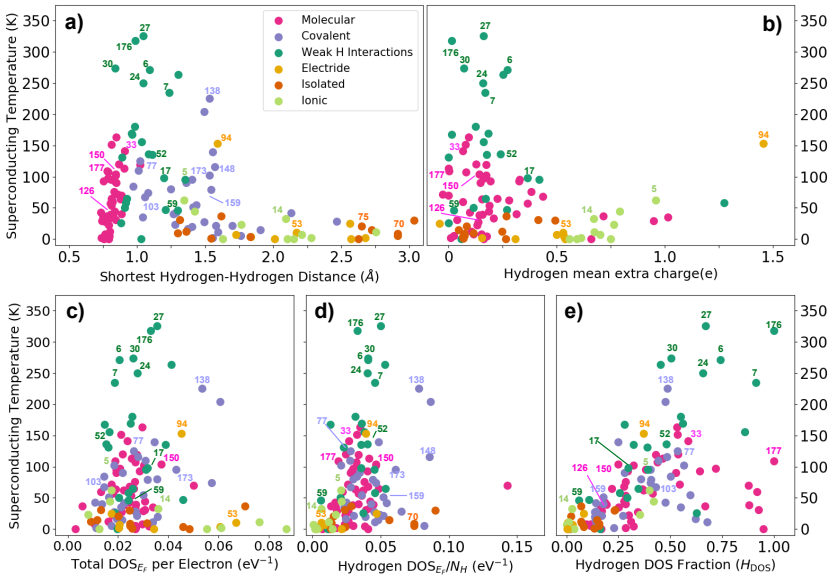

FIGURE 5.2 – Panel **a)** shows T_c as a function of the shortest hydrogen-hydrogen distance. Panel **b)** shows T_c as a function of the mean extra electrons per hydrogen atom. Panels **c)**, **d)**, and **e)**, respectively, show T_c as a function of the total density of states at the Fermi level, the density of states at the Fermi level projected on the hydrogen *s* orbitals per hydrogen, and the fraction of the total density of states at the Fermi level coming from the hydrogen orbitals.

bond can be considered broken. Interestingly, this analysis highlights that such H-H distance variation is not related to a variation of pressure. On a broad level, increasing the pressure does not necessarily yield an increment of the bonding distance, so composition rather than pressure appears to be a more relevant variable to tune. The shortest hydrogen-hydrogen distance for the covalent family spans between 1 to 2.5 Å. Low symmetry covalent systems appear between 1 to 1.45 Å where the short H-H distance is due to H-H bonds appearing beside the dominant hydrogen-host bonds. This zone is for the covalent family a zone of transition towards the weak hydrogen-hydrogen interactions family. As mentioned in the previous section, whenever for the covalent compounds the value of H_f becomes high, the number of covalent H-X bonds saturates and H-H bonds start to appear. The highest reported superconducting temperature for these systems is about 135 K for BH_3(77). Interestingly, at around 1.55 Å the covalent family exhibits a sharp spike in the predicted T_c through systems sharing linear $X = H = X$ bonds originating through the host *p* orbitals, a $\bar{3}$m point group, a value of H_f equal to 0.75, and a lack of direct hydrogen-hydrogen

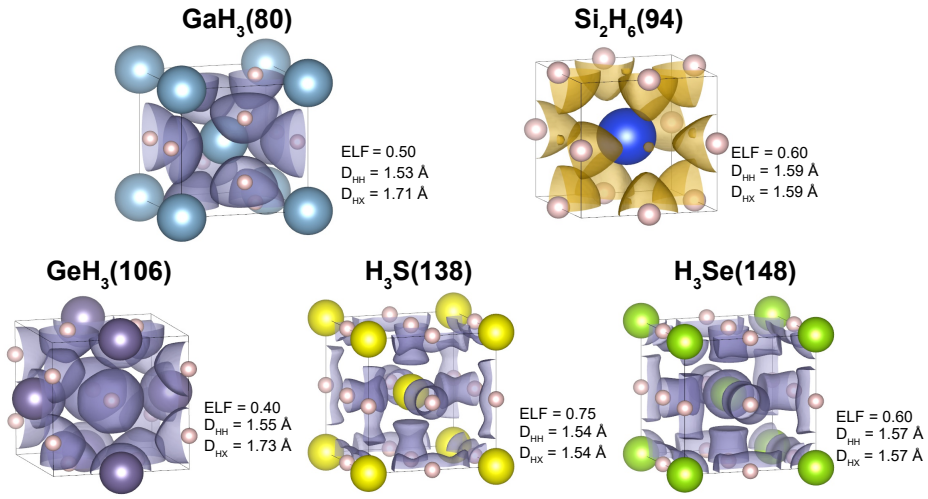

FIGURE 5.3 – This figure shows five compounds related to the T_c spike around a hydrogen-hydrogen distance of 1.55 Å . The pink spheres refer to hydrogen atoms, while the rest refer to the respective host atoms. An electron localization function isosurface is depicted in each case. Also the shortest H-H (D_{HH}) and H-X (D_{HX}) distances are noted. Most of these compounds belong to the covalent family and show a purple electron localization function isosurface. The Si_2H_6 compound is an electride (note the small electron localization function bubbles in empty sites) and its electron localization function isosurface is shown in orange.

bonds. Here lay systems as $H_3S(138)$, $H_3Se(148)$, $GaH_3(80)$, and $GeH_3(106)$. Interestingly, the $Si_2H_6(94)$ electride also shares these features even if the bonding nature is slightly different. All these compounds are shown in figure 5.3 with a representative electron localization function isosurface. For H-H distances above approximately 1.55 Å a sharp drop in T_c appears with systems not reaching above 50 K. This zone lacks direct hydrogen-hydrogen bonds and features systems with a low percentage of hydrogen, with mostly isolated, electride and ionic behavior. Hence, systems with covalent elongated bonds, being H-H with high H_f or H-X with H_f=0.75, seem to be the best candidates to increase T_c.

Panel **b** of figure 5.2 shows the mean extra electrons per hydrogen atom obtained analysing the charge though the Bader method. The mean extra electrons per hydrogen atom ($\bar{\rho}$) is estimated as:

$$\bar{\rho} = \frac{\sum_{i=1}^{N_H} Q_i - N_H}{N_H}, \tag{5.2}$$

where Q_i is the number of electrons assigned to the ith hydrogen atom by

the Bader method and N_H is the total number of hydrogen atoms in the cell. The covalent family has been excluded from this panel due to the difficulty to associating the charges to the atoms. Such issue arises from the difficulties in assigning shared electrons in the H-X bonds to each atom due to the complex representations of the charge regions.

Overall hydrogen atoms tend to gain electrons due to their higher electronegativity with respect to other atoms in the cell. We observe that the highest T_c values are associated with small charge transfers, i.e. from 0 to 0.25 extra electrons per hydrogen atom. As the extra charge increases, T_c drops sharply below 50 K, exception made for the BeH_2(5), compound belonging to the ionic family with T_c = 97 K, and Si_2H_6(94), with T_c = 153 K and part of the electride family but also showing covalent characteristics.

It is often mentioned in the literature that an increment of electron doping on the hydrogen atom leads to a weakening of the hydrogen-hydrogen bonds [34, 39, 104, 187]. The obtained results show that both molecular and weak covalent hydrogen-hydrogen interaction families exhibit non-negligible extra electrons on the hydrogen atoms. It was also observed that the extra charge on the hydrogen is responsible for a slight increment of the H-H distance for the weak covalent hydrogen-hydrogen interaction family. In fact, compounds within this family with a shorter H-H distance tend to have less extra electrons per hydrogen atom. The maximum extra electron per hydrogen among this family is around 0.5, albeit imposed by ionic family definition, increasing up to 1 extra electron per hydrogen atom in the molecular systems.

Panels **c**, **d**, and **e** in figure 5.2 report the results for the density of states analysis. The total density of states per electron at the Fermi level shown in panel **c** features a sharp increment in the highest superconducting temperatures for a density of states value of around 0.015 eV^{-1}. However, for such values, compounds with very low T_c can still be found suggesting that the total density of states at the Fermi level is not a good general descriptor for the trends of T_c, as already been suggested in the literature [188]. This feature is not completely unexpected. The main parameter currently used to determine if a compound has a high value of T_c is the electron-phonon coupling constant (λ) shown in equation (4.59). Although it is true that the latter exhibits a proportional dependence from the total density of states at the Fermi level, it also has a dependence from the phononic density of states and the electron-phonon coupling parameter g of equation (3.29). For this reason, it is possible for a material to posses a high density of states at the Fermi level but reduced electron-phonon coupling which, consequently reduces the value of T_c. However, a recent study performed on different phases of solid hydrogen [189] showed the density of states per atom at the Fermi level exhibits a good correlation with

T_c. This might suggest that the density of states at the Fermi level could be a good descriptor for the value of T_c for chemically equivalent systems.

Considering that H atoms, due to their light mass, are responsible for the large values of T_c in these compounds, the projection of the density of states at the Fermi level onto hydrogen atoms was investigated. The results are reported in panel **d** of figure 5.2). The resulting trends are similar to those obtained for the total density of states. This quantity suggest again that the key for high superconductivity is not strictly related to the value of the density of states. What seems to be more relevant is the fraction of active hydrogen atoms at the Fermi energy H_{DOS} reported in panel **e**. This quantity is obtained dividing the contribution to the density of states at the Fermi energy coming from the hydrogen orbitals by the total density of states at the Fermi level. In agreement with the previous observations, only molecular and weak covalent hydrogen-hydrogen interaction families are able to reach high amounts of density of states coming from the hydrogen active atoms. Nevertheless, false positives exist, specially among molecular compounds, where T_c appears very low despite the large contribution of hydrogen states to the Fermi surface. Furthremore, again for high level of H_f, there is a clear separation between the value of T_c for the molecular and weak hydrogen-hydrogen interactions families. This suggests that the density of states alone is not a good indicator for the T_c and that stoichiometry and atomic arrangement plays as well a relevant role. In fact, as mentioned before, the density of states misses the information on how electrons are coupled with the lattice vibrations, feature that is enhanced by the weakening of interatomic bonds as highlighted by variations in T_c in the transition between molecular and weak hydrogen-hydrogen interaction compounds. Systems with very high values of the density of states at the Fermi energy but with very low electron-phonon coupling will not exhibit high superconducting critical temperatures.

CHAPTER 6

The Networking Value

This chapter is dedicated to the introduction of the networking value. The latter is an observable based on the identification of crystal networks of electron localization function isosurfaces. The networking value is found to exhibit correlations with the superconducting critical temperature for all hydrogen based superconductors.

6.1 Overview

The analysis of the set of hydrogen based superconductors exposed in the previous section was able to reveal insightful correlations of the electronic and structural properties with the superconducting critical temperature. Quantities such as high density of states at the Fermi energy, high fraction of hydrogen atoms, weakened covalent bonds, low or high group in the periodic table for the host atoms or specific structural patterns are all able to enhance the value of T_c. However, this same analysis reveals that even if such quantities indeed exhibit trends related to the T_c, they are in a way quantities serving as necessary but not sufficient conditions. A clear example is for the value of the density of states at the Fermi level. Maximizing the latter will indeed give a chance to have a better superconductor, but for high values of density of states there is still the chance to find poor superconductors. The reason for this issue lies on the fact that all the studied quantities are electronic properties and, to have a good superconductor, is

not only necessary to know its electronic behavior but also how strongly the latter couple with the phonons.

This chapter proposes an attempt to devise a new universal descriptor for the superconducting quality of a system based on the identification of electronic delocalization networks, identified by means of the electron localization function. Here a simple magnitude, the networking value, which is easily obtained from the calculation of electron localization function isosurfaces, is defined. Such quantity reveals useful by suggesting insights on the chemistry and patterns for good superconductors, and it is able to give a reasonable first estimate of the T_c for hydrogen based superconductors without the need of performing electron-phonon coupling calculations.

6.2 NETWORKING THROUGH THE ELECTRON LOCALIZATION FUNCTION

The electron localization function is a quantity suited to analyze the degree of electronic localization. Its isosurfaces at high values reveal regions in space where electrons localize. In fact, for isosurfaces with values close to unity the electrons are localized generally on atomic sites and start to delocalize towards neighbors as the value decreases, eventually revealing the interatomic bonding patterns. Considering these properties, it is then possible to take advantage of the electron localization function in order to analyze the degree of delocalization on a crystal size scale. For systems composed by atoms where the electrons are localized around the nuclei, as in the case for hydrogen rich systems, one could consider to attempt modelling the interaction between phonons and electrons looking at the localization of the electrons. Phonon properties ultimately depend on the forces holding the lattice together, which, in the case of covalent systems, ultimately arise by the localization of the electrons in the interstitial sites in the lattice. What one would want is strongly localized electrons on sites, but also a non zero probability for these electrons to hop from an atomic site to another, leading to a net between strongly localized sites bridged by localized overlapping regions between sites.

In a rough attempt to define an observable that could capture the features previously described, a quantity called networking value (ϕ), defined as *the highest value of the electron localization function that creates an isosurface spanning through the whole crystal in all three Cartesian directions*, was introduced. The ϕ value can thus be easily extracted by calculating the electron localization function and determining at which value a crystal sized isosurface is created when lowering the value of the electron localization function from 1. Generally speaking, the isosurface that will result encloses

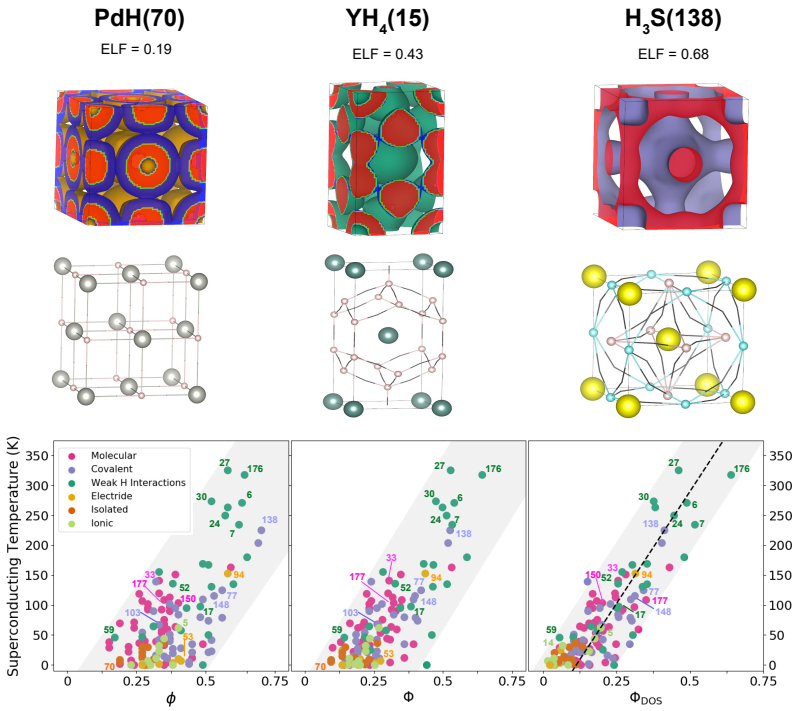

FIGURE 6.1 – The upper panel shows the electron localization function isosurface and the three dimensional network spanning through all the crystal, which is formed by the electron localization function saddle points and the atoms, associated with the ϕ value for PdH(70), YH_4(15), and H_3S(138). The networking value is given for each case. The bottom panels show the critical temperature T_c as a function of the networking value ϕ (left), the networking value multiplied by H_f (center), $\Phi = \phi H_f$, and the networking value multiplied by H_f and the cubic root of the fraction of the DOS at the Fermi energy coming from the hydrogen atoms H_{DOS}, $\Phi_{\mathrm{DOS}} = \phi H_f \sqrt[3]{H_{\mathrm{DOS}}}$ (right). The dotted line in the last panel represents a fit for which $T_c = (750\Phi_{\mathrm{DOS}} - 85)$ K which is able to estimate T_c within 60 K.

most of the atoms in the crystal, but not necessarily all. In this description the saddle points of the electron localization function surfaces reveal crucial for the determination of the networking value, especially for hydrogen based compounds. For these systems, where hydrogen-hydrogen bonds are dominant, the saddle points identify the weak or strong interatomic bonds that pave the crystal sized electronic localization network. Thus, for the determination of the networking value, it is sufficient to identify the ensemble of electron localization function saddle points at the highest value of electron localization function able to bridge the gap between different atoms and create the 3D network.

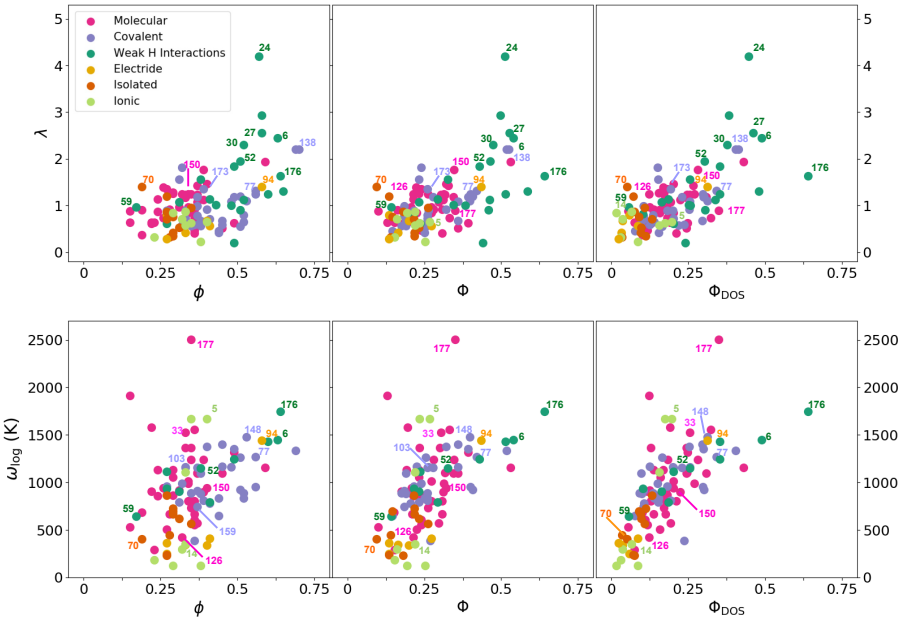

FIGURE 6.2 – The figure shows respectively λ and $\omega_{\log}$ as a function of the networking value (ϕ), the reduced networking value (Φ), and the reduced networking value corrected by the hydrogen contribution to the DOS at the Fermi energy (Φ_{DOS}).

Figure 6.1 reports the electron localization function isosurfaces related to the ϕ value as well as the networks created by the saddle points for this electron localization function value for PdH(70), YH_4(15), and H_3S(138). These three cases are related to the most common types of networks identified during the analysis: isolated, weak covalent hydrogen-hydrogen interaction, and covalent families, respectively. In PdH(70) the network includes both Pd and H atoms. The isolated behavior of the atoms makes the electron localization function bubbles around the atoms network at very low values of the ELF, 0.19. For YH_4(15) the highest 3D connecting network appears at ELF=0.43, and is constructed only by hydrogen atoms showing a weak covalent interaction. This is one of the cases in which the 3D network subsisting at the highest value of electron localization function does not include all the atoms in the unit cell. For the case of H_3S(138), two interlaced networks appear at ELF=0.68 due to its high symmetry, which is supported by the $H = S$ covalent bonds. Another type of network is the one arising from the electride systems, where the connection appears through the isolated pockets of charge in the empty zones of the unit cell. Additional

example of networks are reported in Appendix A.2.

Interestingly, the networking value correlates rather well with T_c as shown in figure 6.1, clearly much better than any other descriptor based on the structure or the electronic properties presented until now in figures 5.1 and 5.2. These quantities are also the quantities most studied in the current literature. The positive correlation between the networking value and T_c is universal as it was observed to hold for all bonding families for hydrogen based superconductors. This is not surprising as bonding families are determined by localized electrons around atomic cores, while the networking value is related instead to delocalized electrons that bridge the space between locally bonded units.

Further analysis have been performed by applying additional conditions over the definition of the networking value; adding requirements such as having all hydrogen atoms taking part to the network, or connecting the atoms up to a certain distance through direct channels of electron localization function, has shown to increase the accuracy of the correlation. This result is not unexpected. Considering that the networking value is an attempt to try to reproduce the coupling between electrons and phonons, one would have to consider in the network as many channels of interactions as possible and not just limit to the strongest interactions as obtained by considering the highest 3D network. However, the addition of the extra restriction introduced a substantial complication and ambiguity related to the procedure for the determination of the networking value. For this reason the definition of the networking value was restricted to the bare minimum requirement necessary to have a good correlation. Such minimum requirement corresponds to the 3D nature of the network as, while performing the analysis, it was observed that the relaxation of this latter restriction produced a complete loss of correlation.

There are however different ways to improve the correlation between ϕ and T_c. As seen in figure 6.1, an improvement in the correlation is obtained by multiplying ϕ by the hydrogen fraction H_f of the compound:

$$\Phi = \phi H_f. \tag{6.1}$$

A explanation for such improvement is related to the fact that the hydrogen fraction is a rough estimation of the multiplicity of hydrogen bonds. Systems with few H atoms will tend to form less bonds in which H atoms participate. This is in contrast with hydrogen rich systems with an incredible number of bonds in which H atoms participate. A further improvement can be obtained by adding a correction coming from the density of states by defining

$$\Phi_{\mathrm{DOS}} = \phi H_f \sqrt[3]{H_{\mathrm{DOS}}}, \tag{6.2}$$

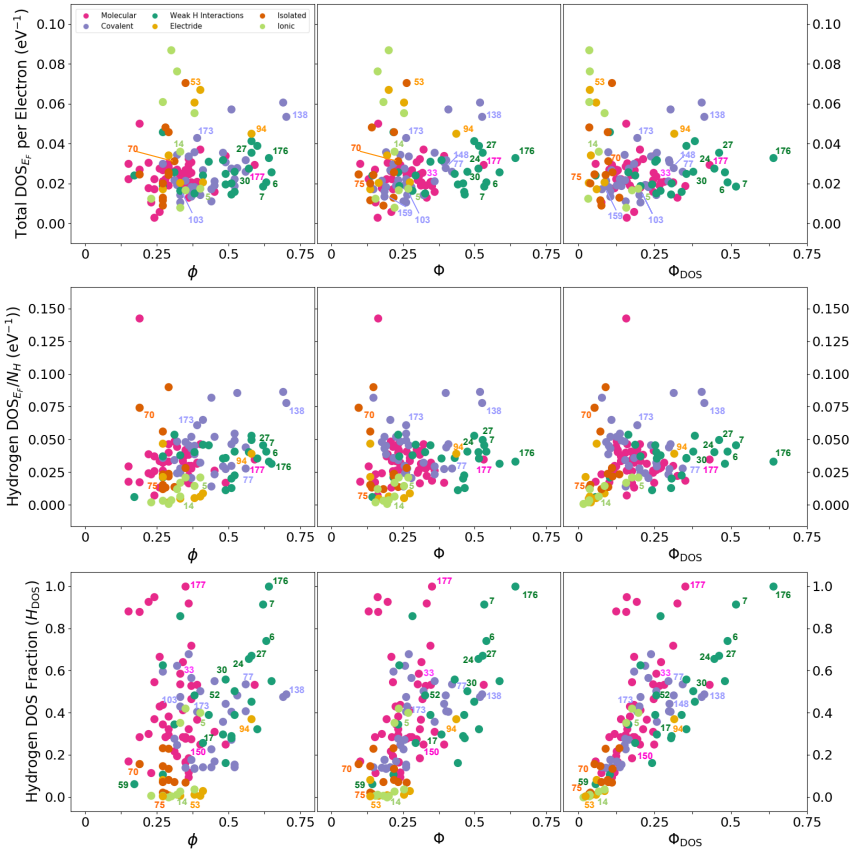

FIGURE 6.3 – The figure shows the total DOS per electron at the Fermi energy, the hydrogen contribution at the DOS at the Fermi energy per hydrogen atom, and the fraction of DOS at the Fermi level coming from the hydrogen orbitals as a function of the *networking value* (ϕ), the reduced networking value (Φ), and the reduced networking value weighted by the fraction of DOS at the Fermi level coming from the Hydrogen atoms (Φ_{DOS}) (See main text for the definitions) .

where H_{DOS} is the hydrogen fraction of the total density of states at the Fermi energy. The introduction of this quantity is able to screen out all those systems that have a high value of Φ but a low contribution of H atoms to the density of states, i.e., all systems that present good bonding properties for superconductivity but lack active electrons coming from hydrogen at the Fermi level to host it. In fact, the networking value does not correlate at all with the density of states at the Fermi level, not even with the density of states coming from H atoms as can be seen from figure 6.3, underlining that these two descriptors are measuring different quantities.

The networking value offers for the first time an adimensional magnitude that shows a striking correlation with T_c, which is valid to estimate the superconducting critical temperature in hydrogen-based superconductors. In fact, the obtained results show that the superconducting critical temperature of these systems can be predicted, within roughly 60 K, following the $T_c = (750\Phi_{\mathrm{DOS}} - 85)$ K equation.

It is illustrative to look at the simple McMillan equation of the critical temperature (4.60) in order to understand if the correlation found with the networking value is assigned to the electron-phonon coupling constant λ or to the logarithmic average phonon frequency $\omega_{\log}$. As shown in Fig. 6.2 both λ and $\omega_{\log}$ correlate with ϕ, Φ, and Φ_{DOS}. This confirms that the networking value is able to capture how prone electrons are to couple to phonons. Also, the average strength of the bonds, which affects phonon frequencies. However, the correlation found for both λ and $\omega_{\log}$ is worse than the one found for T_c. The reason is that many of the predictions in our dataset are obtained in materials with rather low phonon frequencies, close to structural instabilities. In this regime, while λ soars, $\omega_{\log}$ is suppressed. This balancing is eventually able to preserve the correlation with T_c also in these cases.

In conclusion, the networking value ϕ defined here has shown to be able to capture effectively how sensitive the electronic cloud is on average to lattice vibrations, and, consequently, correlates well with T_c. As extracting ϕ simply requires the analysis of electron localization function isosurfaces, which can be easily obtained post-processing DFT ground state calculations, it offers a simple way of screening hydrogen-based superconductors, as well as showing the correct directions to chemically engineering better hydrogen-based superconductors. Interestingly, although the definition of ϕ is completely general, not limited to the presence of hydrogen in the system, one would expect it to potentially be applied to estimate the T_c of all phonon-mediated superconductors.

As a final word for this section, it is important to underline that the superconducting critical temperatures used to find correlations are extracted directly from the literature, without being recalculated. All the T_c values were obtained by first principles DFT calculations, but at different levels of theory, for instance, for the estimation of the critical temperature. Indeed, for the highest critical temperature systems, the value of T_c can vary up to 40 K depending on the choice of μ^*. The wide grey area in Fig. 6.1 could be the result of such inconsistencies. In addition, most of these T_c values have been obtained assuming that the ground state structure is the one given by the minimum of the Born-Oppenheimer energy surface and that lattice vibrations can be described within the harmonic approximation around these positions. However, in hydrogen-based superconductors, the crystal

structure can be largely modified by ionic quantum effects and anharmonicity strongly renormalizes the obtained harmonic phonon spectra, which can strongly impact the predicted T_c as it will be shown in the next part of this thesis. These effects could produce a narrower correlation between T_c and ϕ by introducing variations due to corrections on the structure and T_c.

6.3 DENSITY AND ELECTRON-PHONON COUPLING IN REAL SPACE

The networking value introduced so far is just an heuristic quantity that aims to describe the appearance of the high superconducting temperature. The philosophy behind the networking value is that, in some ways, it is able to capture the coupling between electrons and phonons through the identification of the electron localization function delocalization networks. This section exposes an attempt in formulating an a posteriori description for the validity of the networking value. Since the latter is defined in real space, in order to find the appearance of a correlation between networking value and the electron-phonon coupling, it is useful to express the latter in real space by introducing a transformation of the electronic block states in a set of real space localized Wannier functions [190]. Such transformation is of the form

$$W_{n\mathbf{T}}(\mathbf{r}) = \frac{\Omega_{cell}}{(2\pi)^3} \int_{BZ} d\mathbf{k} e^{-i\mathbf{k}\cdot\mathbf{T}} \sum_m U^{(\mathbf{k})}_{mn} \psi_{m\mathbf{k}}(\mathbf{r}). \tag{6.3}$$

In this equation Ω_{cell} represent the volume of the primitive cell and $U^{(\mathbf{k})}$ represents a unitary transformation matrix for a given $\mathbf{k}$ related to a manifold of occupied Block states ψ that leaves the trace of such manifold invariant. Through this transformation, the electronic density can be expressed as

$$\rho(\mathbf{r}) = \sum_{ij} \sum_{\mathbf{TT}'} W^*_{j\mathbf{T}'}(\mathbf{r}) K_{ij}(\mathbf{T}' - \mathbf{T}) W_{i\mathbf{T}}(\mathbf{r}), \tag{6.4}$$

where K represent the kernel of the density expressed as:

$$K_{ij}(\mathbf{T}' - \mathbf{T}) = \frac{V}{(2\pi)^3} \int_{BZ} d\mathbf{k} e^{-i\mathbf{k}\cdot(\mathbf{T}'-\mathbf{T})} \sum_n \left[U^{(\mathbf{k})+}\right]_{in} f_{n\mathbf{k}} U^{(\mathbf{k})}_{nj}. \tag{6.5}$$

In this equitation $f_{n\mathbf{k}}$ represents the fermionic occupation function for a band n at wave number $\mathbf{k}$.

A simple example for the form of the density can be obtained for a linear chain of hydrogen atoms spaced by a distance L. In this case the system can be described considering just a single localized orbital per hydrogen

site $W_T(\mathbf{r})$ and the density reduces to the sum of the single square Wannier functions:

$$\rho(\mathbf{r}) = \sum_{\mathbf{T}} |W_{\mathbf{T}}(\mathbf{r})|^2. \tag{6.6}$$

It is interesting to consider the value of the density at the middle point of the hydrogen bonds $\mathbf{r}_n = \frac{L}{2} + nL$. The latter can be expressed by symmetrically summing the onsite Wannier functions with respect to the value of $\mathbf{r}_n$:

$$\rho(\mathbf{r}_n) = \sum_{\mathbf{T}} \left[|W_{-\mathbf{T}+\mathbf{L}n}(\mathbf{r}_n)|^2 + \left| W_{\mathbf{T}+\mathbf{L}(n+1)}(\mathbf{r}_n) \right|^2 \right]. \tag{6.7}$$

For the hydrogen atoms it is reasonable to expect the Wannier functions to be exponentially localized around the atomic sites. For this reason, only the first few values of $\mathbf{T}$ are expected to contribute to the values of $\rho(\mathbf{r}_n)$. Fundamentally, for this specific case, even if obtained by summing single site functions, $\rho(\mathbf{r}_n)$ is able to estimate the overlap between functions on different sites. If the electronic density is extremely localized on the atoms, one expects $\rho(\mathbf{r}_n)$ to be vanishingly small at $\mathbf{r}_n$, i.e. both $|W_{-\mathbf{T}+\mathbf{L}n}(\mathbf{r}_n)|^2$ and $\left|W_{\mathbf{T}+\mathbf{L}(n+1)}(\mathbf{r}_n)\right|^2$ will decay exponentially to zero before reaching $\mathbf{r}_n$ and will not overlap. The opposite is also true: for the chain of hydrogen atoms one expects the electronic density between two adjacent atoms to be different from zero. Consequently, this means that the Wannier functions are delocalized enough to overlap with each other.

In the same way it is possible to express the electron phonon coupling parameter of equation (3.29) through its real space form [190] as

$$g_{mn,\nu}(\mathbf{k},\mathbf{q}) = \sum_{\mathbf{T}\mathbf{T}'} e^{i(\mathbf{k}\cdot\mathbf{T}+\mathbf{q}\cdot\mathbf{T}')} \sum_{m'n'a\gamma} \left[U^{(\mathbf{k})+}\right]_{nn'} \left[g_{m'n',a\gamma}(\mathbf{T},\mathbf{T}')\right] U^{(\mathbf{k}+\mathbf{q})}_{mm'} \tau_{a\gamma,\mathbf{q}\nu}, \tag{6.8}$$

where in this equation the quantity $g_{m'n',a\gamma}(\mathbf{T},\mathbf{T}')$ represents the real space representation of the electron-phonon coupling parameter

$$g_{m'n',a\gamma}(\mathbf{T},\mathbf{T}') = \int d\mathbf{r}\, W^*_{m'\mathbf{0}}(\mathbf{r}) \frac{\partial V_{KS}}{\partial \mathbf{R}_{a\gamma}}(\mathbf{r}-\mathbf{T}') W_{m'\mathbf{T}}(\mathbf{r}). \tag{6.9}$$

From this last equation it results clear that the value of $g_{m'n',a\gamma}(\mathbf{T},\mathbf{T}')$ is related to the strength of the overlap between different localized functions. Furthermore it is possible to express an upper limit to $g_{m'n',a\gamma}(\mathbf{T},\mathbf{T}')$ [190] as

$$|\, g_{m'n',a\gamma}(\mathbf{T},\mathbf{T}')\,| \leq \int d\mathbf{r}\,|\, W^*_{m'\mathbf{0}}(\mathbf{r}) W_{n'\mathbf{T}}(\mathbf{r})\,| \int d\mathbf{r}\,|\, \frac{\partial V}{\partial \mathbf{R}_{a\gamma}}(\mathbf{r}-\mathbf{T}')\,| \tag{6.10}$$

Equation (6.10) evidences that the bigger is the overlap between the different sites Wannier functions the stronger will be the electron phonon coupling parameter.

It is reasonable to expect that, when far from a structural instability, $\frac{\partial V}{\partial \mathbf{R}_{a\gamma}}$ will be similar for hydrogen rich systems, especially due to the presence of normal displacements $\tau_{a\gamma,\mathbf{q}\nu}$ in equation (6.9), which tend to dampen the contributions arising from heavier host atoms leaving the hydrogen contributions dominant. Therefore, the strength of the overlap between the localized functions, which can be estimated through the lowest value of the density between localized electron pockets along the bonding paths, it is possibly a good way to estimate the variations of $g_{m'n',a\gamma}(\mathbf{T},\mathbf{T}')$. One issue however lies on the fact that the electronic density is dependent on the specific exchange correlation functional and the specifics of the pseudo potentials used. A solution to this problem comes by instead using the electron localization function which not only is able to determine the areas of localization of electrons, but, although being dependent on the electronic density, is better normalized and much more resistant to variations of functionals and potentials. The idea is then that, using the electron localization function, which constitutes a well normalized quantity, one can estimate the magnitude of the density at the interstitial sites between atoms. Furthermore, considering equations (6.7), (6.9) and (6.10) it is possible to relate this value to the magnitude of the electron phonon coupling parameter.

III

Anharmonicity and quantum ionic fluctuations in hydrogen based superconductors

CHAPTER 7

Phase stability of LaH_{10}

This chapter discusses the phase stability of the C2 and $R\bar{3}m$ phases of LaH_{10} with the inclusion of quantum ionic fluctuations in comparison with the high symmetry $Fm\bar{3}m$ phase. Harmonic classical calculation suggest that the C2 and $R\bar{3}m$ phases have lower entalphy with respect to the high symmetry $Fm\bar{3}m$ phase. However, the introduction of quantum ionic fluctuations completely change this behavior. A structural relaxation performed through the SSCHA is able to show that the C2 and $R\bar{3}m$ phases evolve towards the $Fm\bar{3}m$ phase suggesting that quantum fluctuations can completely alter the energy landscape.

7.1 Overview

In 2017, a systematic high pressure ab initio structural search performed by Liu et al. in the La-H and Y-H systems revealed the stability of the LaH_{10} composition in a sodalite-like face-centered fcc structure above 200 GPa [32]. Additional more accurate studies performed later placed a more accurate guess for the stability of the compound at 230 GPa [191]. At this pressure, the composition was predicted to exhibit a value of the superconducting critical temperature of 280 K. Immediately after the prediction of Liu, a lanthanum hydride structure was synthesized by laser heating a lanthanum sample in a hydrogen-rich atmosphere inside a diamond anvil cell [33]. Based on the unit cell volume obtained by x-ray diffraction, the hydrogen to lanthanum ratio was estimated to be between 9 and 12 and an fcc arrangement of the La atoms was determined above 160 GPa, transitioning

to a rhombohedral $R\bar{3}m$ space group for the La sublattice below. However, due to the small x-ray cross section of hydrogen, it was not possible to experimentally resolve directly the hydrogen lattice and the details of the structure for the compounds remained unknown. Subsequently in 2019, independent efforts of two experimental groups were able to synthesize a LaH_{10} compound and measure a critical temperature of 250 K. Electrical and x-ray diffraction measurements in one of these studies determined a weakly pressure-dependent critical temperature for the LaH_{10} between 137 and 218 GPa in a structure with a face-centered cubic fcc arrangement of lanthanum atoms [24], but still no information about the hydrogen lattice was obtained. Additionally, no transition toward other structures was observed at the lower pressure of stability. Finally later studies performed by Sun et al. [192] reported again the stability of LaH_{10} $Fm\bar{3}m$ till 138 GPa and, below such pressure, a transition to a $C2/m$ phase with lower T_c was observed.

Meanwhile on a theoretical level, in order to identify a stable structure able to reproduce the T_c results in the same pressure range, distorted versions of the fcc structure with space group $C2/m$ and rhombohedral lanthanum sublattice were found to be the lowest enthalpy structures [193]. Unfortunately, no predicted LaH_{10} structure was found to be dynamically stable below 200 GPa, implying that the LaH_{10} phase is not a minimum of the Born-Oppenheimer energy surface in that pressure range. This contradiction between experimental and theoretical results was signaling a problem related to the computational approaches and specifically, considering the presence of light hydrogen atoms, regarding the treatment of the quantum fluctuations of the ions, the behavior of which was already well documented in the literature in other hydrogen-based systems [92, 161, 194].

This chapter reports an ab-initio investigation of the phase stability for the LaH_{10} $C2$ and $R\bar{3}m$ phases at 160 GPa, which are the two lowest phases on the enthalpy convex hull for the LaH_{10} system [191]. The study is performed in presence of quantum ionic fluctuations included through the use of the stochastic self consistent harmonic approximation. The obtained results show that the presence of quantum effects simplify the landscape of phase stability and are able to justify the stability of the fcc LaH_{10} phase below 230 GPa. Furthermore, the obtained results are also able to explain the different lowest pressure of stability of the LaH_{10} fcc phase obtained by the experimental groups through the presence of light anisotropy in the diamond anvil cell.

7.2 METHODS FOR THE CALCULATIONS

The first-principles calculations in this study were performed within density functional theory and the generalized gradient approximation (GGA) as parametrized by Perdew, Burke, and Ernzerhof (PBE) [70]. Harmonic phonon frequencies were calculated within density functional perturbation theory making use of the Quantum ESPRESSO code [180, 181]. A rhombohedral lattice was used in the harmonic phonon calculations for the $R\bar{3}m$ phase, respectively with one LaH_{10} formula unit in the unit cell and a 20×20×20 Monkhorst-Pack shifted grid with a Methfessel-Paxton smearing of 0.02 Ry for the self consistent calculations. A base centered monoclinic lattice was used for the harmonic phonon calculations for the $C2$ phase instead, with 2 LaH_{10} formula units per cell and a 19×19×11 Monkhorst-Pack shifted grid with a Methfessel-Paxton smearing of 0.02 Ry again in the self consistent calculations.

The SSCHA calculations were performed at $T = 0$ K on a 2×2×2 supercell in the $R\bar{3}m$ phase and in the 2×2×1 supercell for the $C2$ phase. The SSCHA calculations for both phases contained 88 atoms. The phonon spectra are obtained by Fourier interpolating directly the SSCHA energy Hessian force constants obtained in a 2×2×2 supercell for the $R\bar{3}m$ phase. The phonon spectra was not calculated for the $C2$ phase.

The DFT calculations for the SSCHA supercells were performed on a coarser electron-momentum grid, which would correspond to a 6×6×6 grid in the $R\bar{3}m$ and $C2$ supercells. It was explicitly verified that this coarser mesh yields a fully converged SSCHA gradient with respect to the electron-momentum grid, therefore not affecting the SSCHA minimization. These were calculated as well within DFT at the PBE level with Quantum ESPRESSO. For the final SSCHA populations, about 1000 configurations were used to reduce the stochastic noise. In all these calculations we used ultrasoft pseudopotentials including 11 electrons for the La atoms, a plane-wave cut-off energy of 50 Ry for the kinetic energy and 500 Ry for the charge density.

For the $R\bar{3}m$ phase, the electron-phonon matrix elements were calculated in a 6×6×6 $\mathbf{q}$ point grid and a 40×40×40 $\mathbf{k}$ point grid. These were combined with the SSCHA phonons and polarization vectors obtained by Fourier interpolation to the 6×6×6 $\mathbf{q}$ point grid from the real space force constants coming from the Hessian of $E(\boldsymbol{\mathcal{R}})$ in a 2×2×2 supercell $R\bar{3}m$. The Dirac deltas on the band energies are estimated by substituting them with a Gaussian of 0.004 Ry width.

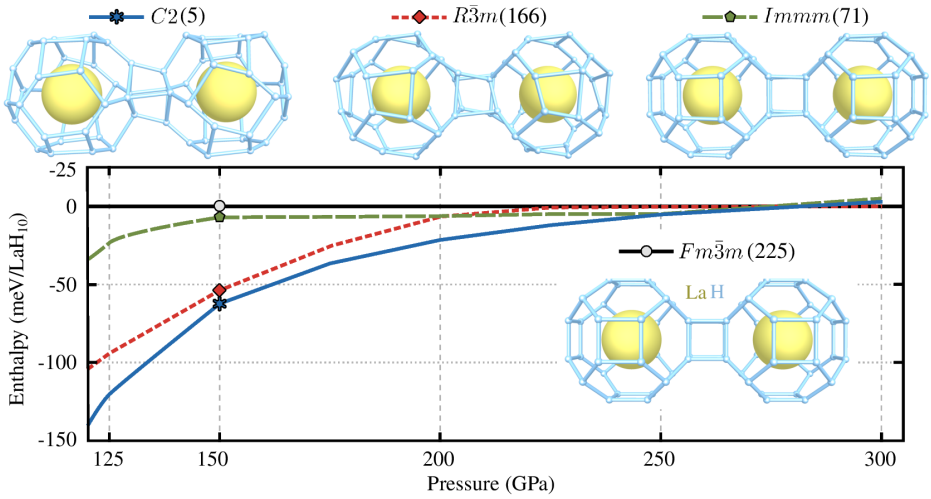

FIGURE 7.1 – The figure shows the enthalpy per LaH_{10} unit as a function of pressure for different structures of LaH_{10} and the various associated structures. The values for the pressures are obtained through the Born-Oppenheimer energy without the inclusion of quantum corrections.

7.3 PHASE STABILITY FOR C2 AND R$\bar{3}m$ LAH_{10}

To start, DFT methods have been used in order to calculate the lowest-enthalpy structures for LaH_{10} as a function of pressure. This was done using state-of-the-art methods for the prediction of crystal structure through the minima hopping method [26, 27]. In this case, the results obtained for the enthalpy are related solely to the Born–Oppenheimer energy and neglect quantum ionic fluctuations. The analysis of the enthalpy reported in figure 7.1 suggests that other phases of LaH_{10}, such as the R$\bar{3}$m, C2 and Immm, are thermodynamically more stable than the fcc phase with Fm$\bar{3}$m symmetry at pressures lower than 250 GPa. Instead, at pressures greater than about 250 GPa, all phases merge to the Fm$\bar{3}$m symmetric phase. The low symmetry phases feature distortion not only in the position of the hydrogen atoms but also in the lanthanum sublattice. Effectively, as can be seen in figure 7.1, the low symmetry phases are distortions of the high symmetry Fm$\bar{3}$m phase. Furthermore, the fact that many structures are predicted emphasizes that the classical Born-Oppenheimer energy surface has a multifunnel structure that is tractable to many different saddle and local minima. Effectively, this suggests that the introduction of the quantum ionic fluctuations could renormalize the energy surface and deeply change the landscape of phase stability.

To investigate this idea, the behavior of the structural stability for the

Fm$\bar{3}$m (C)			Fm$\bar{3}$m (R)			R$\bar{3}$m (R)		
1 La	**4b**	$\left[\frac{1}{2},\frac{1}{2},\frac{1}{2}\right]$	1 La	**4b**	$\left[\frac{1}{2},\frac{1}{2},\frac{1}{2}\right]$	1 La	**3b**	$\left[\frac{1}{2},\frac{1}{2},\frac{1}{2}\right]$
2 H	**8c**	$\left[\frac{1}{2},\frac{1}{2},\frac{1}{2}\right]$ $\left[\frac{3}{4},\frac{3}{4},\frac{3}{4}\right]$	2 H	**8c**	$\left[\frac{1}{4},\frac{1}{4},\frac{1}{4}\right]$ $\left[\frac{3}{4},\frac{3}{4},\frac{3}{4}\right]$	2 H	**6c**	$[\epsilon_a,\epsilon_a,\epsilon_a]$ $[-\epsilon_a,-\epsilon_a,-\epsilon_a]$
8 H	**32f**	$[\epsilon,\epsilon,\epsilon]$ $[-\epsilon,-\epsilon,-\epsilon]$ $[\epsilon,\epsilon,-\epsilon]$ $[\epsilon,-\epsilon,\epsilon]$ $[-\epsilon,\epsilon,\epsilon]$ $[-\epsilon,-\epsilon,\epsilon]$ $[-\epsilon,\epsilon,-\epsilon]$ $[\epsilon,-\epsilon,-\epsilon]$	8 H	**32f**	$[\epsilon,\epsilon,\epsilon]$ $[-\epsilon,-\epsilon,-\epsilon]$ $[-\epsilon,-\epsilon,3\epsilon]$ $[-\epsilon,3\epsilon,-\epsilon]$ $[3\epsilon,-\epsilon,-\epsilon]$ $[\epsilon,\epsilon,-3\epsilon]$ $[\epsilon,-3\epsilon,\epsilon]$ $[-3\epsilon,\epsilon,\epsilon]$	2 H 6 H	**6c** **18h**	$[\epsilon_b,\epsilon_b,\epsilon_b]$ $[-\epsilon_b,-\epsilon_b,-\epsilon_b]$ $[-\epsilon_x,-\epsilon_x,3\epsilon_y]$ $[-\epsilon_x,3\epsilon_y,-\epsilon_x]$ $[3\epsilon_y,-\epsilon_x,-\epsilon_x]$ $[\epsilon_x,\epsilon_x,-3\epsilon_y]$ $[\epsilon_x,-3\epsilon_y,\epsilon_x]$ $[-3\epsilon_y,\epsilon_x,\epsilon_x]$

TABLE 7.1 – The table summarizes the occupied Wyckoff positions for the LaH_{10} with Fm$\bar{3}$m and R$\bar{3}$m structures. The R$\bar{3}$m symmetry structure is presented in its rhombohedral description and the Fm$\bar{3}$m symmetry structure is presented both in its standard cubic (C) and rhombohedral (R) descriptions so to be compared with the lower symmetry phase.

C2 and R$\bar{3}$m phases of LaH_{10} has been analysed in the presence of quantum ionic fluctuations. The latter have been treated through the use of the stochastic self consistent harmonic approximation. Starting from the $R\bar{3}m$ structure, to properly understand the effect of quantum fluctuations over the complex phase stability landscape, it is necessarily to understand how to model the structure and how to put it in relationship to the high symmetry fcc phase with Fm$\bar{3}$m symmetry. Table 7.1 reports the Wyckoff positions for both Fm$\bar{3}$m and R$\bar{3}$m phases. The Wyckoff positions correspond to a description of the atomic coordinates of the atoms using crystal coordinates and highlight sites related by specific symmetry operation. Ultimately the description of a system through Wyckoff positions is able to reduce the number of degrees of freedom for the description of the system.

Each atomic position is given by a triad of numbers in crystal space as $[x,y,z]$. The triad should be understood as an $x\mathbf{a}+y\mathbf{b}+zlater$ atomic position with **a**, **b**, **c** the lattice vectors. For the $R\bar{3}m$ phase in the rhombohedral lattice (R), the three lattice vectors have the same length, and the angle

between them is the same ($\alpha = \beta = \gamma$). The $Fm\bar{3}m$ phase is described both in this rhombohedral description (R) and, for comparison, in the standard cubic conventional lattice (C). In the $Fm\bar{3}m$ phase the lanthanum atom is described by the $4b$ sites, two hydrogen atoms occupy the $8c$ sites, and the remaining eight hydrogen atoms occupy the $32f$ sites. Most of the atomic positions are fixed by symmetry, and overall the $Fm\bar{3}m$ structure can be described by one single free parameter (ϵ) related to the $32f$ site. In the $R\bar{3}m$ phase the lanthanum atom is locked in the $3b$ sites, two pairs of hydrogen atoms occupy the $6c$ sites and the remaining six hydrogen atoms occupy the $18h$ sites. In this case symmetry allows for more freedom and overall the structure of the $R\bar{3}m$ phase can be described by four free parameters (ϵ_a, ϵ_b, ϵ_x and ϵ_y) with the addition of the lattice vector and the angle between them. For the $C2$ structure instead, the symmetry is much lower and does not properly able to provide simplifications in the understating of the structure.

To investigate the renormalization of the energy surface and the change of phase stability. A quantum relaxation of the internal atomic coordinates for both $R\bar{3}m$ and $C2$ phases was performed according to symmetry with the lattice that yields a classical isotropic pressure of 150 GPa and vanishing classical forces that is calculated from $V(\mathbf{R})$. During the relaxation the shape and size of the unit cell was maintained fixed. The parameters of the two phases at the beginning of the relaxation are reported in table 7.2.

The behaviour of the diagonal components of the stress tensor during the internal relaxation for the $R\bar{3}m$ and the $C2$ phases is shown in the right panel of figure 7.3 and the left panel of figure 7.2. At the beginning of the SSCHA relaxation, between step 0 and 1, the introduction of the quantum fluctuations generate an increment in pressure of about 10 GPa. The pressure then develops anisotropy with a relative difference of about 10 GPa between the different components during the relaxation and a substantial variation of the atomic coordinates is generated during the same dynamic. This can be observed in the left panel of figure 7.3 reporting the percentage variation of the free Wycoff sites of the $R\bar{3}m$ phase. The relative variation of the atomic components is of the order of 5% reaching up to 12% for the ϵ_b parameter.

The behavior of the $R\bar{3}m$ phonon spectra and the superconducting properties was then investigated after the internal relaxation and is shown in figure 7.4. The figure reports the phonons obtained after the SSCHA relaxation obtained through the free energy phonons and by setting $\boldsymbol{\mathcal{D}}^{(4)} = 0$, the harmonic phonons obtained before the SSCHA relaxation and the value of the Eliashberg function $\alpha^2 F(\omega)$ together with the electron-phonon coupling parameter λ. In the SSCHA phonons, $\boldsymbol{\mathcal{D}}^{(4)}$ was set to zero since it was observed it to have a negligible contribution. The analysis of the phonon

Space group	Lattice paramters	Wyckoff positions		
$C2$- LaH_{10}	a = 6.154 Å	La	**4c**	[0.492, 0.001, 0.253]
	b = 3.606 Å	H	**4c**	[0.140, 0.246, −0.052]
	c = 7.238 Å	H	**4c**	[0.098, 0.241, 0, 450]
	β = 55.714 °	H	**4c**	[0.360, 0.256, 0.052]
		H	**4c**	[0.402, 0.260, 0.550]
		H	**4c**	[−0.098, 0.001, −0.051]
		H	**4c**	[0.868, 0.001, 0.437]
		H	**4c**	[0.887, 0.001, 0.694]
		H	**4c**	[0.871, 0.000, 0.191]
		H	**4c**	[0.731, 0.000, 0.881]
		H	**4c**	[0.762, 0.001, 0.368]
$R\bar{3}m$ - LaH_{10}	a = 3.545 Å	La	**3b**	[0.500, 0.500, 0.500]
	γ = 62.342 °	H	**6c**	[0.260, 0.260, 0.260]
		H	**6c**	[0.099, 0.099, 0.099]
		H	**18f**	[−0.107, −0.107, 0.361]

TABLE 7.2 – The table reports the cell parameters and the Wyckoff sites and parameters for the structures of the LaH_{10}-$R\bar{3}m$ and the LaH_{10}-$C2$ phases .

spectra reveals that the structure in the presence of quantum fluctuations is stable in this state, where the pressure is anisotropic. At 160 GPa and with a fixed rhombohedral angle of 62.3 ° the superconducting critical temperature T_c is 222 K for the $R\bar{3}m$ phase, about 10% lower then the reported T_c for the $Fm\bar{3}m$ phase [191]. The T_c was calculated with the Allen-Dynes formula of equation (4.60) and with $\mu^* = 0.1$. This value of μ^* was chosen by using the Allen-Dynes formula to reproduce the T_c of the $Fm\bar{3}m$ phase calculated with anisotropic Migdal-Eliashberg and in presence of the non approximated Coulomb interaction of reference [191]. The lower value of T_c for the $R\bar{3}m$ phase suggests that undesired anisotropic stress conditions in the diamond anvil cell can induce phase transitions. It is then probable that T_c measurements with lower values around 200 K correspond to distorted structures induced by anisotropic conditions of pressure. The analysis for the phonon spectra for the $C2$ phase after the SSCHA relaxation of the internal coordinates was not performed.

The SSCHA relaxation for both $R\bar{3}m$ and $C2$ phases was then continued allowing this time both atomic coordinates and the lattice vectors to relax according to symmetry and maintaining the pressure fixed to 160 GPa. The behavior of the diagonal components of the stress tensor for the $C2$ phase is reported in the right panel of figure 7.2 while the behavior of the lenght

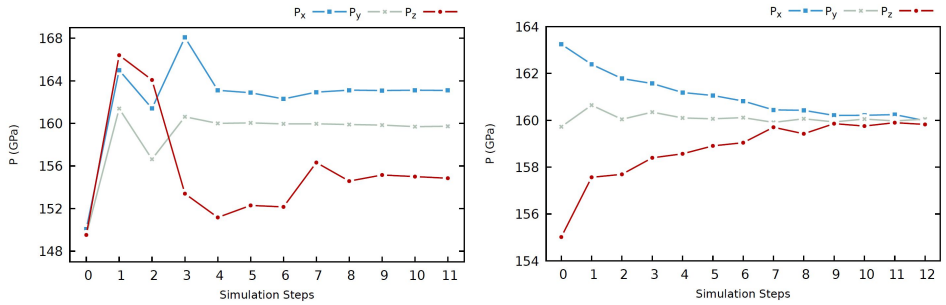

FIGURE 7.2 – The left panel reports the evolution of the quantum pressure for the $C2$-LaH_{10} during the SSCHA relaxation of the internal coordinates. The zeroth step in this panel represents the starting classical pressure before the relaxation. The right panel reports the evolution of the quantum pressure during the total SSCHA relaxaion where both cell and atomic position are left free to vary.

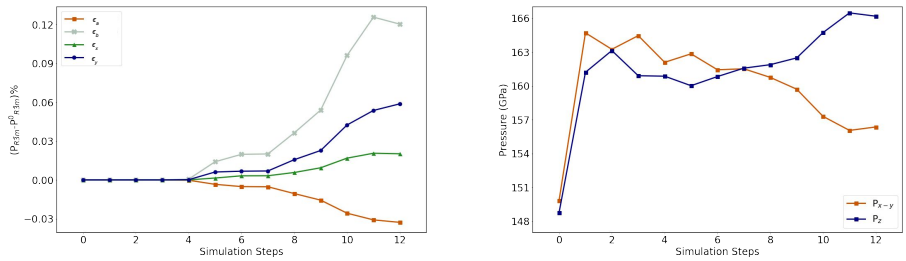

FIGURE 7.3 – The figure shows the relative difference in the displacement of the atomic positions on the left panel and the evolution of the diagonal components of the quantum stress tensor on the right panel for the $R\bar{3}m$-LaH_{10}. In the right panel the pressure at the zeroth step is the classical pressure before of the relaxation.

of the lattice vectors, the angle between them, the pressure and the atomic coordinates for the $R\bar{3}m$ phase are reported in figure 7.5. The systems reach again a state with isotropic pressure after the relaxation. Observing the parameters of the $R\bar{3}m$ phase of figure 7.5 it can be seen that lattice parameter, cell vectors and atomic position evolve toward those expected for the $Fm\bar{3}m$ phase. The angle between the lattice vector reaches 60° while the Wyckoff parameters reported in 7.1 for the $R\bar{3}m$ phase evolve toward those for the $Fm\bar{3}m$ phase in its rhombohedral representation. Specifically, the value of ϵ_a reaches 0.25 while the values of ϵ_b, ϵ_x and ϵ_y converge to the same value of 0.1205 becoming compatible with the $8c$ and $32f$ sites of the $Fm\bar{3}m$ symmetry group. A final symmetry analysis for both $R\bar{3}m$

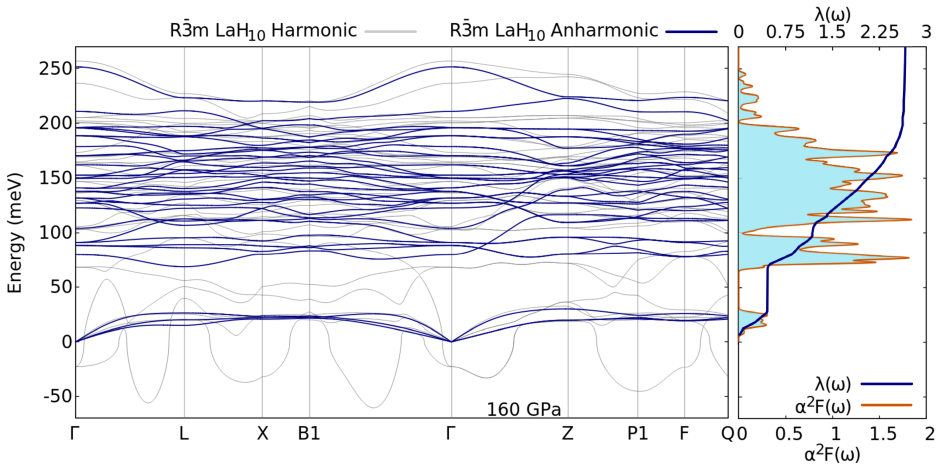

FIGURE 7.4 – The figure reports the phonon spectra for the initial structure of the $R\bar{3}m$-LaH_{10} before the SSCHA relaxation and the phonon spectra for the final structure obtained after the relaxation of the internal atomic coordinates performed through the SSCHA. On the right side are reported the Eliashberg function and the electron phonon coupling parameter for the phonons related to the SSCHA relaxation.

and $C2$ phases revealed their structures after the SSCHA relaxation were converged to the $Fm\bar{3}m$ phase with an accuracy of about 0.024 and 0.014 Å in the atomic positions, respectively.

Ultimately, the results of the relaxation suggest that the quantum energy landscape is much simpler than the classical $V(\mathbf{R})$ landscape and that the ground state of LaH_{10} over the pressure range of interest is the $Fm\bar{3}m$ phase with sodalite-type symmetry. The quantum effects are substantial, reshaping the energy landscape and stabilizing structures by more than 60 meV per LaH_{10}.

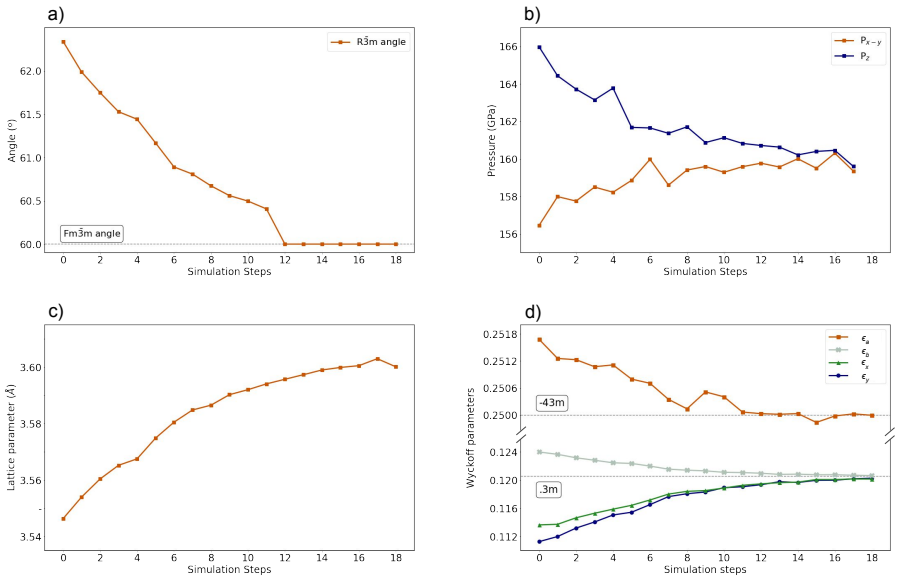

FIGURE 7.5 – The figure shows the evolution of the structural parameters of the $R\bar{3}m$-LaH_{10} during the complete SSCHA relaxation. On the top and bottom left is shown the evolution of the angle between the vectors and the lenght of the vectors of the rhombohedral cell, respectively. On the top and bottom right are shown the different components of the diagonal part of the stress tensor and the variation of the wyckoff free parameters, respectively.

CHAPTER 8

Structural stability and superconductivity of $LaBH_8$

This chapter is dedicated to the study of the effect of quantum ionic fluctuations over the phase stability of the $Fm\bar{3}m$-$LaBH_8$. Quantum fluctuations tend to renormalize the crystal structure increasing the lowest pressure of stability from 40 GPa to 77 GPa. Additionally the value of the superconducting critical temperature is strongly enhanced through the structural renormalization induced by quantum fluctuations.

8.1 Overview

The potential of first-principles calculations based on density-functional theory (DFT) has shown to be crucial in guiding experimental efforts [19, 51, 99]. Many of the experimental discoveries in the past years have been in fact anticipated by DFT calculations [30–32, 34, 195]. Furthermore, making use of DFT-based structural prediction methods, most of the binary combinations of hydrogen and host atoms have been theoretically explored. However, the stability of binary hydrides having a predicted superconducting critical temperature above 100 K has been limited to pressures above 100 GPa, with the exception of RbH_{12}, calculated to be stable at 50 GPa with a T_c of about 115 K [52].

The efforts with first-principles calculations are now shifting towards further expanding the list of predicted compounds attempting to explore the energy landscape of ternary and quaternary hydrides [37–41]. Two of the most prominent results are the prediction of a T_c of about 450 K at 250 GPa for $MgLi_2H_{16}$ [39] and the possible metastability down to 40 GPa of $LaBH_8$ in the $Fm\bar{3}m$ high-symmetry phase. This latter compound exhibits a remarkable T_c of approximately 120 K [40, 43] at 50 GPa. This suggests that with the right ternary combination of atoms it is possible to synthesize phases at high pressures that could remain metastable down to room pressure. Additionally, the same structural motifs of $LaBH_8$, with a similar critical temperature, have also been recently predicted for $BaSiH_8$ and $SrSiH_8$ [41]. This further confirms that high-T_c ternary hydrogen-rich compounds may be (meta)stable at ambient pressure.

In most of the DFT-based calculations for hydrogen-based superconductors at high pressure, however, the ions in the system are treated as classical particles. This means they are considered as a fixed point at the local minima of the $V(\mathbf{R})$ Born-Oppenheimer energy surface and the vibrational phonon frequencies are determined from the second derivatives of $V(\mathbf{R})$ taken at the minimum. The vector $\mathbf{R}$ represents the position of all atoms in the crystal. As anticipated in the theory part, for this specific class of systems composed mainly of light hydrogen atoms, it is important to have in mind that quantum ionic fluctuations cannot be neglected and can significantly alter the structural, phononic, and superconducting properties. This was in fact shown in chapter Chapter 7 on the $C2$ and $R\bar{3}m$ phases of LaH_{10}, where the landscape of phase stability at the lower pressures is completely reshaped by quantum fluctuations. It seems that, as illustrated by the LaH_{10} case, quantum effects tend to stabilize structures with a large electron-phonon coupling and keep them stable at much lower pressures than expected with standard calculations treating the ions classically.

In this chapter we present an investigation of the effect of quantum ionic fluctuations in $LaBH_8$ through *ab initio* DFT calculations and the use of the stochastic self-consistent harmonic approximation (SSCHA) [61–64]. Here, the thermodynamic stability and superconducting properties of this compound are studied with the hope that quantum effects could make $LaBH_8$ metastable even at ambient pressure. The obtained results show that quantum effects and the consequent anharmonicity enhance the superconducting critical temperature, but, contrary to the case of LaH_{10}, tend to destabilize the $Fm\bar{3}m$ crystal structure, making it dynamically unstable below approximately 77 GPa.

8.2 METHODS FOR THE CALCULATIONS

The DFT calculations presented in this chapter are performed with the plane-wave Quantum ESPRESSO [180, 181] package using ultrasoft pseudopotentials with the Perdew-Burke-Ernzerhof [182] parametrization of the exchange-correlation potential including 3 electrons of boron and 11 of lanthanum in the valence. The cutoff for the wavefunctions and density are chosen as 90 Ry and 900 Ry, respectively. The integration over the Brillouin zone in the self-consistent calculations are performed with a first-order Methfessel-Paxton smearing of 0.02 Ry broadening and a 30×30×30 **k**-point grid. The electronic properties such as electron localization function (ELF) [85, 196, 197] and Bader [183] charge are calculated using the Quantum ESPRESSO post processing tools.

The harmonic phonon calculations are performed on a 6×6×6 phonon **q**-point grid making use of density functional perturbation theory (DFPT) [89]. The SSCHA calculations are performed on a 2×2×2 supercell containing 80 atoms, which yielded $\boldsymbol{\mathcal{D}}^{(\bar{F})}(\mathbf{q})$ anharmonic dynamical matrices in a commensurate 2×2×2 **q**-point grid. The difference between the harmonic and anharmonic dynamical matrices are Fourier interpolated to a finer 6×6×6 grid, and, by adding to the interpolated result the harmonic dynamical matrices, $\boldsymbol{\mathcal{D}}^{(\bar{F})}(\mathbf{q})$ are obtained in the 6×6×6 grid. The SSCHA minimization was converged using a 7×7×7 coarser **k**-point grid for the DFT self-consistent calculations in the supercells needed to get the forces for the stochastic minimization of the free energy. The SSCHA was run at 0 K.

The electron-phonon interaction is calculated both in the classical harmonic and quantum anharmonic cases. In both cases a 40×40×40 **k**-point grid was used to sample the electron-phonon matrix elements of equation (3.29), with a Gaussian smearing of 0.008 Ry to approximate the Dirac deltas in the equation, and 6×6×6 **q**-point grid. For the classical harmonic case the electron-phonon interaction is calculated having the atoms sitting at the positions $\mathbf{R}_0$ that minimize $V(\mathbf{R})$, while in the anharmonic case the atoms are placed at the positions $\boldsymbol{\mathcal{R}}_{eq}$ obtained through the SSCHA minimization.

The superconducting critical temperature is calculated by solving the isotropic Migdal-Eliashberg equations with values of μ^* between 0.1 and 0.15, with an energy cutoff of 1.5 eV for the Matsubara frequencies for all pressures, which is around 5-10 times the maximum phonon frequency in the material, respecting the validity of the μ^* approximation for the Coulomb matrix elements [13]. The Eliashberg function is calculated both at the harmonic or anharmonic levels, respectively, by plugging into equation (3.29) the harmonic phonon frequencies and polarization vectors or their

TABLE 8.1 – Values of the hydrogen Wyckoff parameter for the classical structure (x_c), the shortest hydrogen-boron distance (d_c^{H-B}), and the related classical pressure (P_c) at the lattice parameter a. For the same lattice parameters we report the hydrogen Wyckoff parameter (x_q), the shortest hydrogen-boron distance (d_q^{H-B}), and the associated pressure obtained through equation (3.44) (P_q) calculated after the quantum SSCHA structural relaxation.

a(Å)	x_c	d_c^{H-B}(Å)	P_c(GPa)	x_q	d_q^{H-B}(Å)	P_q(GPa)
5.577	0.1459	1.409	50	0.1489	1.438	58
5.427	0.1474	1.386	75	0.1498	1.408	84
5.311	0.1485	1.366	100	0.1506	1.385	110

anharmonic counterparts obtained diagonalizing $\boldsymbol{\mathcal{D}}^{(F)}$.

8.3 STRUCTURAL AND ELECTRONIC PROPERTIES OF $LaBH_8$

The face-centered cubic unit cell of the superconducting $LaBH_8$ shown in figure 8.1 respects a $Fm\bar{3}m$ symmetry, with the boron, lanthanum, and hydrogen atoms located, respectively, at the **4a**, **4b**, and **32f** Wyckoff sites. While the La and B **4a** and **4b** sites are completely fixed by symmetry, the H **32f** site has a free parameter. A representative of the **32f** site can be written as $[x, x, x]$. Thus, the entire structure can be determined by only two free parameters: the lattice parameter a and the x parameter related to the hydrogen **32f** sites.

A classical structural relaxation of the system, in which the x and a parameters are determined from $V(\mathbf{R})$, was performed at 50, 75, and 100 GPa. After the relaxation, the lattice parameter and the hydrogen Wyckoff parameter were found to be, respectively, 5.577 Å and 0.14592 at 50 GPa, 5.427 Å and 0.1474 at 75 GPa, and 5.311 Å and 0.1485 at 100 GPa. The boron-hydrogen shortest distance decreases with increasing pressure, passing from a value of 1.409 Å at 50 GPa to 1.366 Å at 100 GPa. The structural relaxation was then repeated using the SSCHA for the same lattice parameters obtained for the classical results. After the SSCHA relaxation, the x hydrogen coordinates changed from 0.1459 to 0.1489 at $a = 5.577$ Å (classical pressure of 50 GPa), from 0.1474 to 0.1498 at $a = 5.427$ Å (classical pressure of 75 GPa), and from 0.1485 to 0.1506 at $a = 5.311$ Å (classical pressure of 100 GPa). Using equation (3.44) to compute the quantum pressure, it was found that quantum effects add respectively 8 GPa, 9 GPa, and 10 GPa on top of the classical 50 GPa, 75 GPa, and 100 GPa pressures, respectively, which is in line with the pressure exerted by ionic quantum fluctuations in other hydrogen-rich compounds [161, 191], for instance, in LaH_{10} as shown in Chapter 7. Table 8.1 summarizes the differences

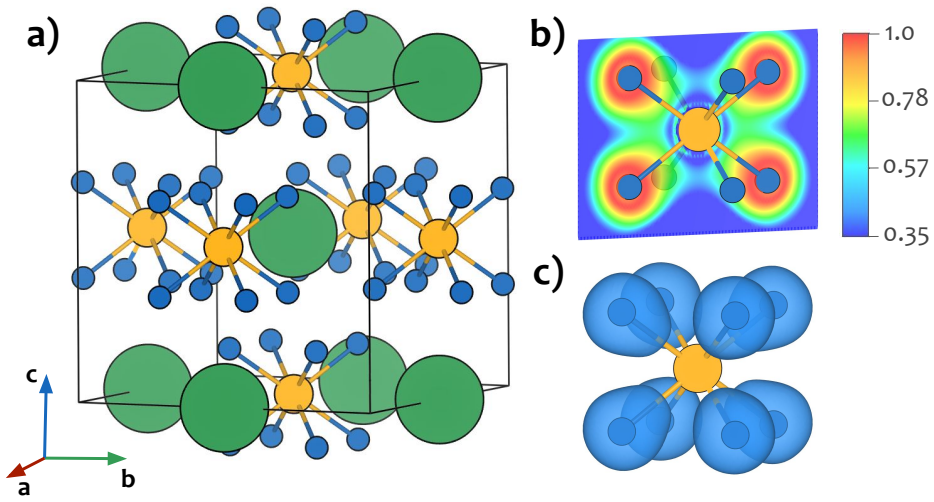

FIGURE 8.1 – (a) Conventional unit cell of $Fm\bar{3}m$-$LaBH_8$. (b) Cross section of the ELF for the BH_8 unit between values of 1 and 0.35. (c) The ELF isosurface of the BH_8 unit at a value of 0.69.

between the quantum and classical pressures and the x parameters for the classical and SSCHA structural relaxations for different lattice parameters. Overall, the introduction of quantum effects through the SSCHA generates an increment in pressure and an expansion of the boron-hydrogen distance for the same lattice parameter of about 2%. This behavior is attributed to the extra space that the quantum atoms occupy with respect to their classical counterparts.

An analysis of the electronic band structure is shown in Fig. 8.2. The calculations were performed for both classical and SSCHA structures corresponding to a lattice parameter of 5.577 Å, which corresponds to a classical pressure of $P_c = 50$ GPa and a quantum pressure of $P_q = 58$ GPa. The results show that the variation of the atomic Wyckoff parameter introduces just small variations of the order of 150 meV in the band structure around the Fermi energy. However, these variations are not significant enough to alter the overall shape of the bands. With respect to the DOS at the Fermi level, quantum effects produce a slight increment of its value. The highest contribution to the DOS comes from hydrogen and lanthanum atoms, which contribute respectively a 67.5% and a 26.4% to the total DOS at the Fermi level in the classical case, values that are slightly adjusted to 65% and 26.4% with the inclusion of ionic quantum effects.

The analysis of the ELF shows how the $LaBH_8$ system is composed by

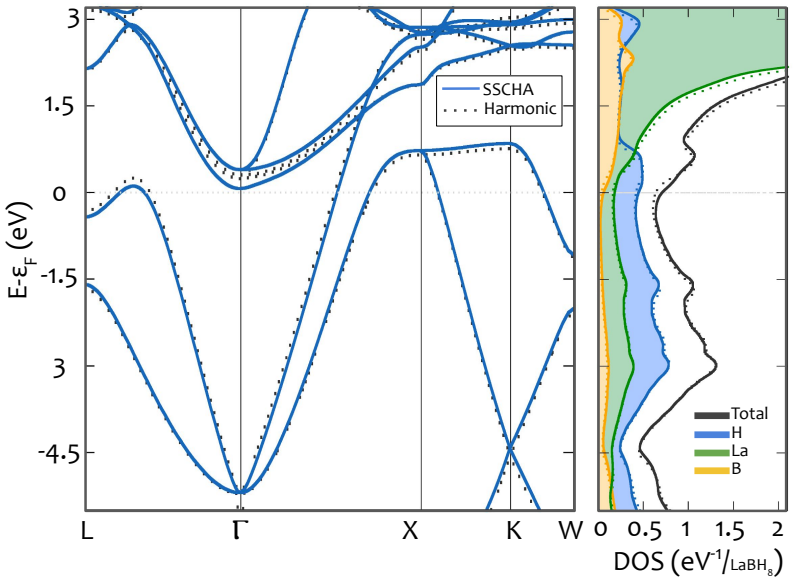

FIGURE 8.2 – (Left panel) Electronic band structure with the atoms at the $\mathbf{R}_0$ classical harmonic sites and at the quantum $\boldsymbol{\mathcal{R}}_{eq}$ sites after the SSCHA relaxation, in both cases with $a = 5.577$ Å. (Right panel) Total DOS and its projections onto different atoms calculated both at the classical harmonic positions (dotted lines) and quantum SSCHA positions (solid lines).

BH_8 units, where the boron atom is covalently bonded with eight hydrogen atoms as shown in figure 8.1. The appearance of the covalent bonds is identified by an elongation of the ELF isosurfaces around the hydrogen atoms towards the boron atom. This specific pattern respects the appearance of covalent bonds for hydrogen atoms [197]. Furthermore, the analysis of the Bader charge shows the La atom donates 1.49 electrons to the BH_8 unit, a feature that suggests the existence of an ionic bond between the La atoms and the BH_8 units.

As a test, the behavior of the networking value presented in Chapter 6 (ϕ) was analyzed for the classical and quantum structures for $a = 5.577$ Å ($P_c = 50$ GPa) and $a = 5.311$ Å ($P_c = 100$ GPa). To recall, the networking value is the highest value of the ELF that creates an isosurface that expands periodically in all the crystal. For the classical and quantum structures at $a = 5.577$ Å, the respective values of ϕ are 0.28 and 0.30. The network is constructed by cores of BH_8 units, as shown in figure 8.1b, that weakly bond with each other. According to the ELF classification in Chapter 5, the bonding between adjacent BH_8 units appears at values of ELF too low to

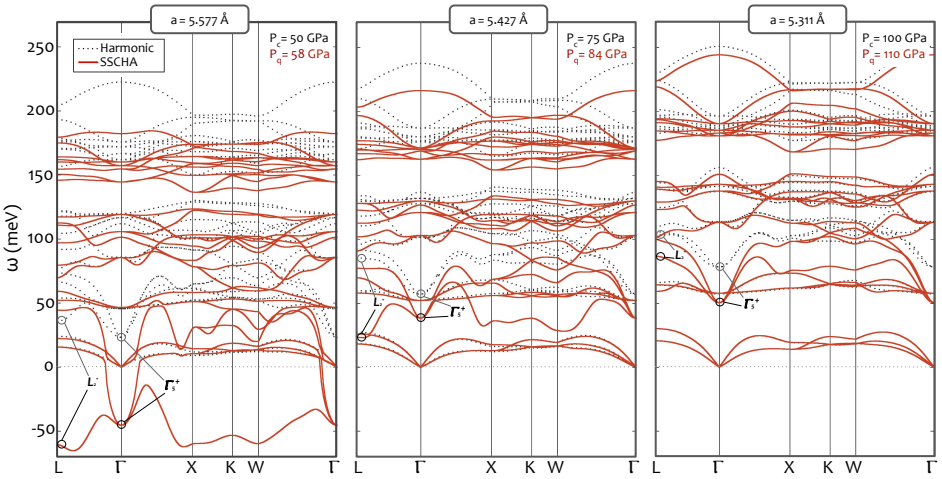

FIGURE 8.3 – Phonon spectra calculated for the lattice parameters reported in Table 8.1 at the harmonic and anharmonic (SSCHA) level. The harmonic phonon energies are calculated with the hydrogen atoms at the $[x_c, x_c, x_c]$ sites. The SSCHA anharmonic phonons are calculated from $\boldsymbol{\mathcal{D}}^{(F)}$ with the hydrogen atoms at the $[x_q, x_q, x_q]$ sites. The introduction of quantum effects increases the pressure for the same lattice parameter.

be considered as a weak covalent hydrogen-hydrogen system, which is the type of bonding that yields the highest T_c's. Combined with the fraction of hydrogen atoms in the stoichiometry (H_f) and the hydrogen fraction of the DOS at the Fermi energy (H_{DOS}), the networking value gives rise to an expected value for the critical temperature of 60 K and 70 K for the classical and quantum case, respectively, according to the $T_c = (750\phi H_f H_{\mathrm{DOS}}^{1/3} - 85)$ K formula. At the smaller lattice parameter $a = 5.311$ Å for the classical and quantum structure we obtained respectively values of $\phi = 0.30$ and $\phi = 0.32$, predicting critical temperatures of 70 K and 80 K, respectively. These results fall inside the dark area of figure 6.1 confirming that the networking value possesses predictive power. The networking value analysis suggests, thus, that quantum fluctuations will enhance the critical temperature in $Fm\bar{3}m$-$LaBH_8$.

8.4 PHONON PROPERTIES AND LATTICE INSTABILITIES OF $LaBH_8$

The phonon spectra calculated at the classical harmonic level with the atoms at the $\mathbf{R}_0$ positions and at the quantum anharmonic level with atoms at the $\boldsymbol{\mathcal{R}}_{eq}$ positions are shown in figure 8.3. The calculations at the highest

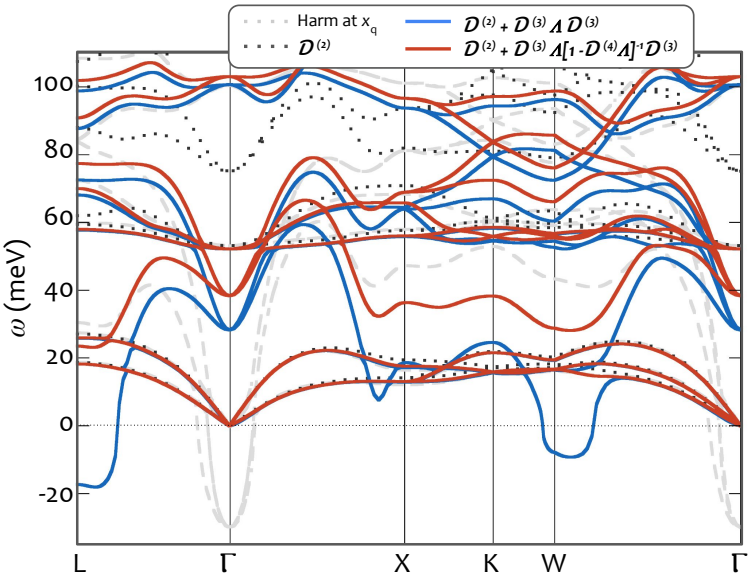

FIGURE 8.4 – Harmonic phonons with $a = 5.427$ Å with the H atoms at the quantum positions $[x_q, x_q, x_q]$, together with the different contributions to the SSCHA free energy Hessian $\boldsymbol{\mathcal{D}}^{(F)}$. The figure shows the spectra only at low energies to illustrate better the effect of the different terms..

pressure with $a = 5.311$ Å show that the spectrum is characterized by three distinctive regions separated with energy gaps. The acoustic modes have a predominant La character. The group of phonon modes in the 50-150 meV energy range have both boron and hydrogen character. The bands with dominant B behavior show a very weak dispersion, approximately at 57 meV. The other modes in this range are dominated by hydrogen bond bending modes. Higher energy bands, above $\sim$ 175 meV, mostly involve hydrogen bond stretching vibrations. At larger lattice parameters, i.e. lower pressure, the H bond-bending modes soften, and a mode with irreducible representation Γ_5^+, also labeled as T_{2g}, becomes unstable below $P_c = 45$ GPa in the harmonic approximation.

The quantum expansion of the BH_8 unit produces dramatic effects on the phonon energies, mainly introducing a large overall softening of all hydrogen-character phonon modes. La and B character modes are, on the contrary, barely affected by quantum anharmonic effects, even if hydrogen bond-bending modes get mixed with the lanthanum acoustic modes at low pressures. The main effect of quantum fluctuations is that the structure becomes unstable at higher pressures than in the classical calculations.

While the classical structure is stable for $a = 5.577$ Å ($P_c = 50$ GPa), $\boldsymbol{\mathcal{D}}^{(F)}$ has large imaginary eigenvalues at different points of the Brillouin zone for the same lattice parameter ($P_q = 58$ GPa). As shown in figure 8.4, it is remarkable that in the calculation of $\boldsymbol{\mathcal{D}}^{(F)}$ the $\boldsymbol{\mathcal{D}}^{(4)}$ term in equation (3.43) has a large impact and cannot be neglected, contrary to what happens in other hydrogen-based superconductors [130, 191, 198]. This is specially true around the pressures at which the instabilities appear. It is also worth mentioning that, even if the harmonic phonons with $a = 5.427$ Å are stable if the H atoms occupy the classical $[x_c, x_c, x_c]$ sites (see Fig. 8.3), the structure is moved to a saddle point of the Born-Oppenheimer energy surface when the H atoms sit instead at the $[x_q, x_q, x_q]$ sites, which is illustrated by the imaginary frequencies obtained at the harmonic level for this position (see Fig. 8.4).

In the calculations including quantum anharmonic effects, $Fm\bar{3}m$-$LaBH_8$ becomes unstable at a pressure of approximately 77 GPa. The instability is led by an optical phonon mode at the L point with L_2^- symmetry, associated with a bond bending oscillation of the H atoms around the boron atom. The Γ_5^+ mode, which describes a rhomboidal-like distortion of the BH_8 unit, becomes unstable soon after at 70 GPa. At lower pressures, the whole branch becomes unstable pointing towards a clear quantum instability of the BH_8 unit. In the work by Di Cataldo *et al.* [40] the classical instability of the Γ_5^+ mode was estimated at 35 GPa, which is consistent with the 45 GPa pressure obtained in this study, and that anharmonic effects only increased this pressure by 5 GPa. In the calculations of this study, however, quantum effects increase the destabilization pressure by 32 GPa. The difference is that in the previous calculation anharmonicity was considered neglecting its effect on the atomic positions and considering exclusively the anharmonic self-interacting terms of the Γ_5^+ mode. Our results show that anharmonicity cannot be treated in such a simplistic model, as the latter cannot describe the impact of anharmonicity on the whole phonon spectrum as well as the ionic positions.

Starting by the structure obtained after the SSCHA relaxation with the lattice parameter 5.577 Å, the distortion patterns introduced by the Γ_5^+ and L_2^- modes were further studied by deforming the atomic structure according to the corresponding eigenvectors. The deformation was performed without changing the shape and size of the unit cell and internal atomic coordinates where deformed until reaching a local energy minimum as shown in figure 8.5. For the case of the triply degenerate Γ_5^+ mode, we show the displacement pattern that yields the lowest-energy local minimum. There are four equivalent L points in the Brillouin zone and each of them has associated a L_2^- mode. The L_2^- mode yielding the lowest energy local minimum is the

one reported in figure 8.5. The deformation of the atomic coordinate obeys the following form:

$$X^{\alpha}_{i,p} = X^{\alpha}_{0i,p} + \delta b^{\alpha}_{\mu i,p}, \tag{8.1}$$

where $X^{\alpha}_{i,p}$ is the atomic position of atom i in the unit cell p along Cartesian direction α, δ is an arbitrary deformation parameter, and $b^{\alpha}_{\mu i,p}$ is a real space polarization vector of the form

$$b^{\alpha}_{\mu i,p} = \sqrt{\frac{M_0}{N_p M_i}} e^{i\mathbf{q}\cdot\mathbf{R}_p} \epsilon^{\alpha}_{\mu i}(\mathbf{q}). \tag{8.2}$$

Here N_p is the number of unit cells commensurate with the wave number $\mathbf{q}$, $\mathbf{R}_p$ is a unit cell lattice vector, and M_0 is a mass renormalization parameter obtained by having the vectors $b^{\alpha}_{\mu i,p}$ satisfy the condition

$$\sum_{i\alpha p} M_i (b^{\alpha}_{\mu i,p})^* b^{\alpha}_{\mu' i,p} = M_0 \delta_{\mu\mu'}. \tag{8.3}$$

After reaching the minimum energy given by the deformation, the structure was further relaxed with a complete classical cell relaxation. The latter was performed by letting both atoms and cell relax with a fixed pressure of 50 GPa. For both distortions it was found the BH_8 unit dissociates into a BH_6 unit. For the distortion pattern that started with the Γ_5^+ mode the two remaining hydrogen atoms sit in an interstitial site, while for the structure distorted initially with the L_2^- mode they merge and form a H_2 molecule. The enthalpy of the starting $Fm\bar{3}m$ classical structure, with $a = 5.577$ and the atoms at positions $x_c = 0.1459$ ($P_c = 50$ GPa), was compared to the enthalpy of the final relaxed structure. It was found that the structure obtained after the relaxation following Γ_5^+ is 0.8 eV/$LaBH_8$ lower in enthalpy, while the structure obtained following L_2^- is 1.2 eV/$LaBH_8$ lower.

The obtained results suggest that at low pressures the high-symmetry $Fm\bar{3}m$ classical structure sits in a very shallow local minimum, which is much higher in energy than other distorted structures. Although the system possesses a high symmetry, the shape of the potential $V(\mathbf{R})$ related to deformations of the BH_8 unit is not at all symmetric, and the ionic quantum fluctuations are enough to take the system out of the local minimum and to destabilize the system towards decomposition. This behavior is quite interesting when compared with the results of Chapter 7. The results of the introduction of quantum fluctuations generate complete opposite effects, even if both structure exhibit the same space group symmetry. The difference between the two lies in the specific of the bonding patterns of the structure and will be further investigated in the next chapter. These results

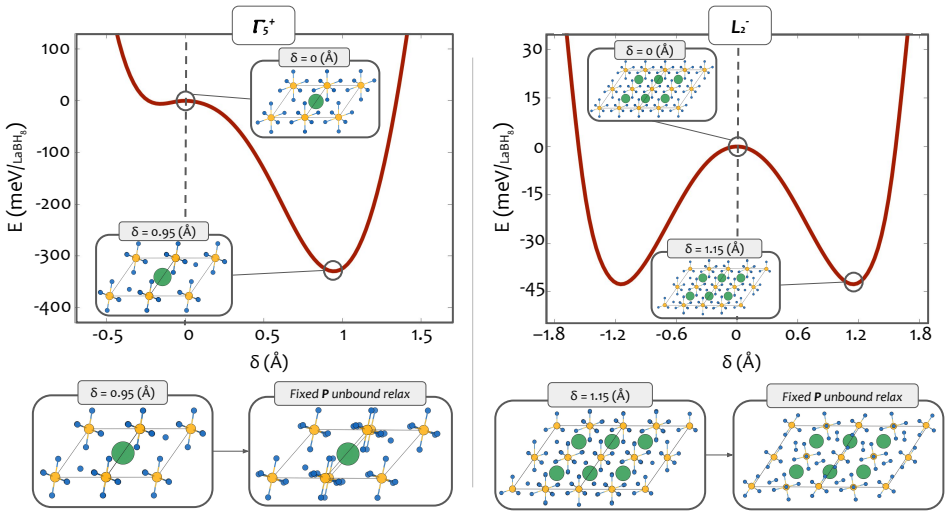

FIGURE 8.5 – Born-Oppenheimer energy variation occurring along the distortion patterns introduced by the Γ_5^+ and the L_2^- modes starting with the H atoms at the $[x_q, x_q, x_q]$ Wyckoff positions obtained after the SSCHA structural relaxation at $a = 5.577$ Å. The $LaBH_8$ unit cells before the distortion, at the minimum of the potential energy curve, and after a classical cell relaxation at fixed $P_c = 50$ GPa are also shown in each case.

highlight the importance of performing quantum structural relaxations in superconducting hydrogen-rich compounds, including in the calculations the kinetic energy of the ions. Generally speaking, it is reasonable to expect that ionic quantum effects will also tend to destabilize other low pressure metastable phases composed by isolated covalent bonded units as in $BaSiH_8$ and $SrSiH_8$.

8.5 SUPERCONDUCTING PROPERTIES OF $LaBH_8$

Despite quantum effects destabilize $Fm\bar{3}m$ at higher pressures than expected classically, the SSCHA calculations suggest it is metastable above 77 GPa (quantum pressure). Thus, it is reasonable to investigate its superconducting properties, monitoring the impact of quantum effects and anharmonicity on them. The results for T_c obtained solving isotropic Migdal-Eliashberg equations are shown in figure 8.6. The isotropic approximation is justified, as previous results [40] show a good agreement between the critical temperature obtained with the isotropic and anisotropic Migdal-Elihasberg equations. Indeed, the results obtained in this study at the classical harmonic level are in rather good agreement with those reported

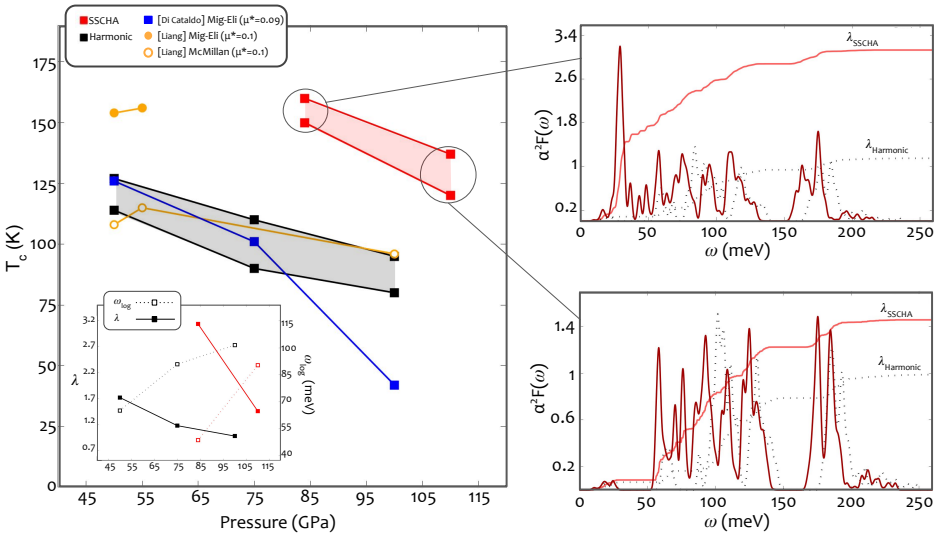

FIGURE 8.6 – Superconducting critical temperatures obtained solving the isotropic Migdal-Eliashberg equations with values of μ^* of 0.1 and 0.15 at the classical harmonic level and quantum anharmonic level, the latter obtained with the SSCHA method. The pressure reported in the graph for the classical result is the classical pressure P_c, while the pressure in the SSCHA results is the quantum pressure P_q. The results are compared to the previous calculations by Di Cataldo *et al.* [40] and Liang *et al.* [43]. The inset shows the pressure dependence of the electron-phonon coupling λ and ω_{log}. The right panels show the $\alpha^2F(\omega)$ function together with the integrated electron-phonon coupling constant $\lambda(\omega) = 2\int_0^\omega d\omega' \alpha^2F(\omega')/\omega'$.

previously [40, 43]. The critical temperature was also calculated with the Allen-Dynes equation (4.60), yielding a value in rather good agreement with the Migdal-Eliashberg result, only 5-15 K lower.

The introduction of the structural and phonon renormalization through the SSCHA has a strong effect on the superconducting properties, contrary to previous estimates in which a negligible impact was claimed [40]. Anharmonicity increases the electron-phonon coupling and reduces the average logarithmic frequency ω_{log}. The increase of λ imposed by quantum anharmonic effects is enough to induce a large enhancement of the predicted T_c. Looking at $\alpha^2F(\omega)$, it is possible to notice that the high value of λ at 84 GPa in the SSCHA is mostly related to the anharmonic softening of the lower optical branches, specifically of the phonon branch containing the Γ_5^+ and L_2^- modes, which make the electron-phonon coupling soar due to the proximity of the system to a structural instability. In general, the overall increment of λ, and consequently T_c, is also due to the quantum weakening of the BH_8 bonds and the consequent softening of the hydrogen-character

phonon modes. This effect is correlated with an overall red-shift of $\alpha^2F(\omega)$.

The reason why in previous calculations [40] a weak anharmonic renormalization of T_c was claimed is because the impact of anharmonicity was only estimated for the Γ_5^+ mode, exclusively considering the interaction of this mode with itself, and because the method used was not able to capture the structural expansion due to quantum fluctuations. In fact, the expansion of the boron-hydrogen bonds pushes the system away from the local minimum of $V(\mathbf{R})$ toward a zone where the potential is much more anharmonic.

CHAPTER 9

General trends for quantum ionic fluctuations

This chapter discusses the effect related to the introduction of quantum ionic fluctuations over the classical phase stability. Here all data of the current literature where quantum fluctuations are treated through the SSCHA are collected. The results obtained highlight that there are two types of effects related to the introduction of quantum fluctuations. Whenever the structure is left unaltered, the systems experiences a reduction in the value of T_c. The contrary is expected whenever quantum ionic fluctuations introduce structural renormalizations.

9.1 Overview

As shown in the two previous chapters, atomic quantum fluctuations around the minima of $V(\mathbf{R})$ cannot be neglected in the case of hydrogen rich compounds, and can significantly alter their structural, phononic, and superconducting properties. The results greatly differ from standard "classical" calculations and, without the inclusion of quantum effects, the computational predictions are not always helpful in guiding experiments.

Through the analysis of the structural stability of the $R\bar{3}m$ and $C2$ phases of LaH_{10}, it was shown that the introduction of quantum ionic fluctuations tend to smoothen the potential surface of the Born-Oppenheimer potential

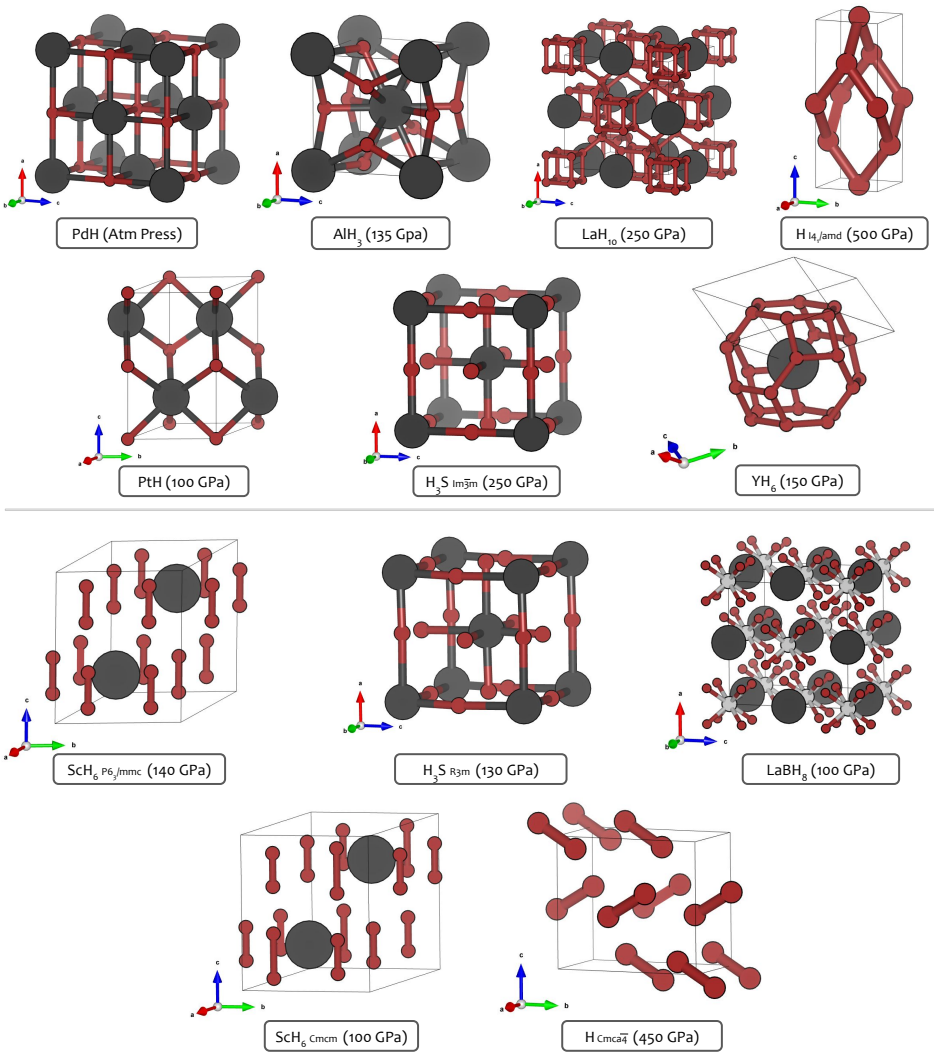

FIGURE 9.1 – The figure shows the unit cell of the structures analysed in this work. The upper panel refers to the structures with highly symmetric bonding patterns for which the structure is not altered by the introduction of quantum effects. The lower panel shows the structures mainly composed by molecular hydrogen, isolated bonded units or distorted phases which are renormalized by the introduction of quantum fluctuations. The black spheres represent the host atoms while red spheres are the hydrogen atoms. In the $LaBH_8$ structure the grey spheres represent the boron atoms.

greatly simplifying the landscape of phase stability. Furthermore, for the LaH_{10} system, quantum fluctuations tend to stabilize the structure and

extend the stability down to lower pressures. All different phases merge into the high symmetric $Fm\bar{3}m$ phase which remains stable down to at least 130 GPa in presence of quantum ionic fluctuations, while in the classical case, the instability appears at 230 GPa. Additionally, comparing the classical and quantum results available in the literature, quantum effects reduce the value of T_c for the $Fm\bar{3}m$ phase. The case of the $LaBH_8$ is instead different. Quantum effects tend to destabilize the system increasing the lowest pressure of stability from 40 to 77 GPa, and introduce structural renormalizations resulting in an enhancement of T_c. Although both LaH_{10} and $LaBH_8$ are part of the same symmetry group, the effects introduced by the quantum ionic fluctuations are fundamentally opposite. One would then wonder if there is or not a set of specific trends to be expected when introducing the effect of quantum fluctuations.

At this point in time, the Stochastic Self Consistent Harmonic Approximation (SSCHA), introduced in Section 3.6, has become a well developed method able to treat in a complete manner the effects of quantum ionic fluctuations. Additionally, the set of compounds analyzed with the inclusion of quantum effects is slowly growing. This allows to attempt deriving general expected trends related to the addition of quantum ionic fluctuations over the conventional structural prediction results.

This chapter is dedicated to an analysis of general trends related to all systems where the quantum ionic fluctuations have been treated through the SSCHA. Here, the general effect that quantum fluctuations introduce, with respect to the harmonic "classical" results, are investigated. This investigation is able to reveal that quantum ionic fluctuations have mainly two effects: whenever their introduction leaves the structure unaltered, the system experiences a reduction in the value of T_c and, contrarily, an increment in T_c is expected whenever the quantum ionic fluctuations introduce structural renormalizations. Furthermore, the analysis suggests the possibility to discern in advance which of the two scenarios is likely to occur through the specific features related to the bonding properties of the systems.

9.2 DATA AND METHODS

The analysis performed here consists in comparing the structural and superconducting properties for classical calculations, where the atoms sit at the local minima of the Born-Oppenheimer energy surface $V(\mathbf{R})$, and the calculations in presence of quantum fluctuations. The comparison was performed for all materials for which SSCHA calculations are available in the literature. One generic pressure per compound was considered. The materials in the analysis include PdH [60, 61] at room pressure; PtH at 100

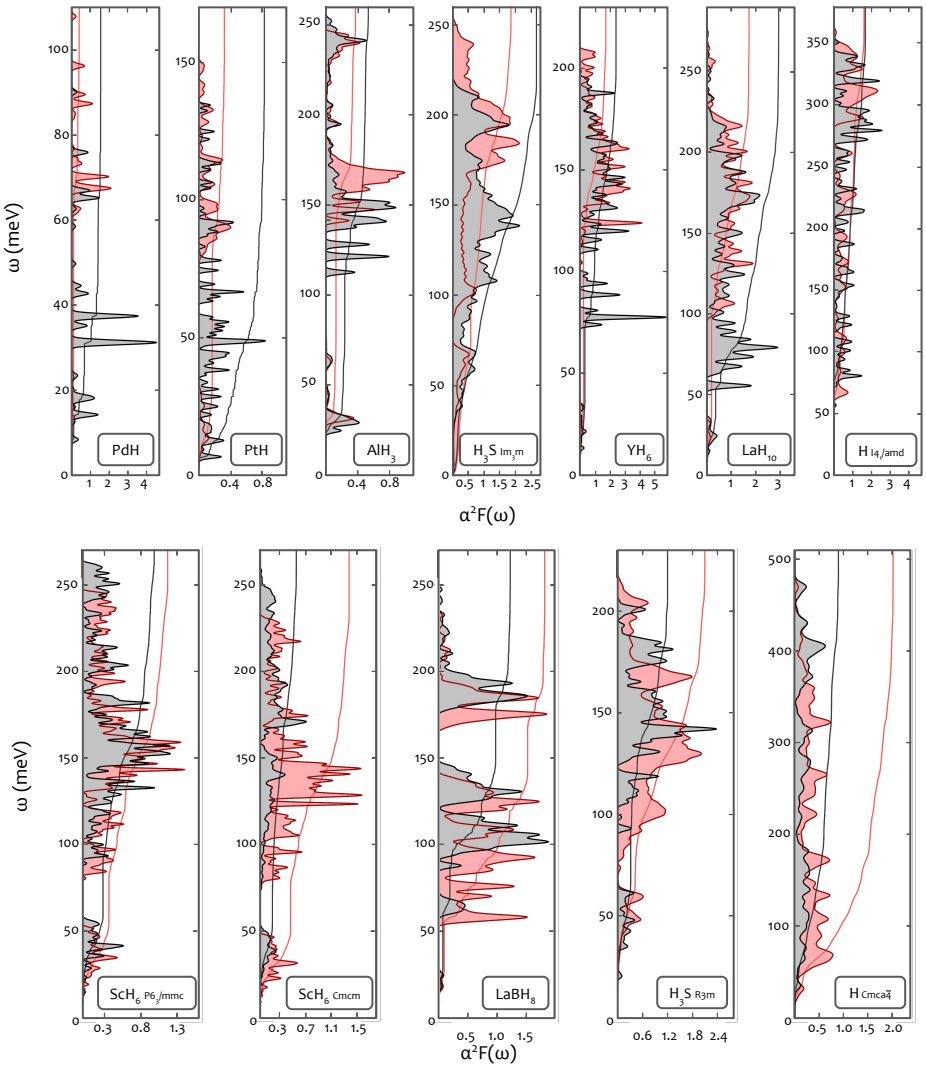

FIGURE 9.2 – The figure shows the Eliashberg function $\alpha^2F(\omega)$ as a function of the energy of the phonon frequency and the value of the electron-phonon coupling parameter λ. In grey and red are respectively the classical calculations and the calculations in presence of quantum fluctuations treated through the SSCHA. The upper panel refers to the systems where quantum fluctuations do not introduce significant structural renormalizations. The lower panel refers instead to those systems where quantum fluctuations strongly alter the crystal structure.

GPa [61]; AlH_3 at 135 GPa [130]; two hydrogen phases, $I4_1/amd$ at 500 Gpa [35], and $Cmca\bar{4}$ at 450 Gpa [179]; YH_6 at 150 GPa [49]; LaH_{10} at 250 GPa [191]; H_3S-$R3m$ at 130 GPa, compared with H_3S-$Im\bar{3}m$ at 130 GPa;

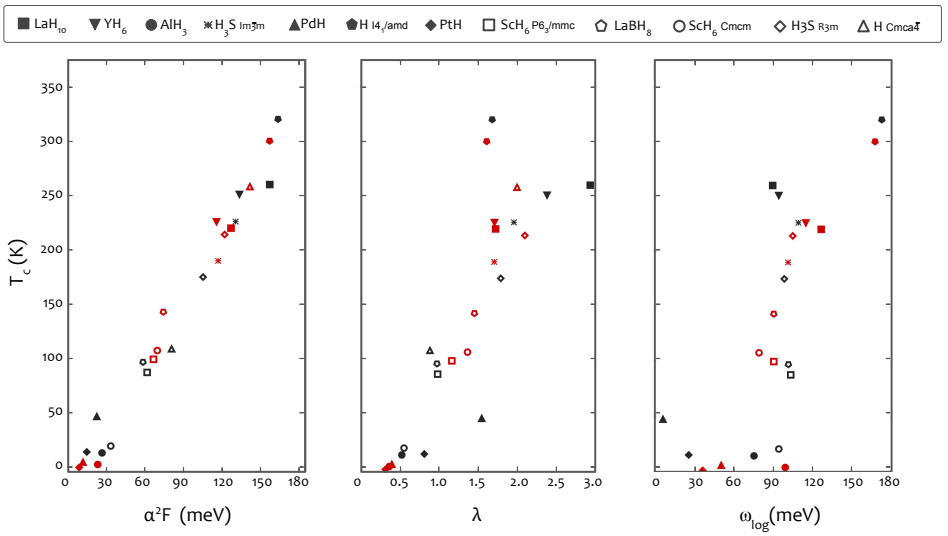

FIGURE 9.3 – The figure shows the value of T_c as a function of the integral of the Eliashberg function, the electron phonon coupling constant λ, and the logarithmic average of the phonon frequency ω_{log}, in the left, middle and right panels, respectively. In black and red are reported respectively the results for the classical calculations and the calculations including quantum fluctuations.

H_3S-$Im\bar{3}m$ at 250 GPa [161, 199]; ScH_6-$Cmcm$ at 100 GPa, compared with ScH_6-$P6_3/mmc$ 100 GPa; and ScH_6-$P6_3/mmc$ 140 GPa; [198] and the results of $LaBH_8$ at 100 Gpa from Chapter 8. The unit cell for all the compounds is reported in figure 9.1. Although for LaH_{10} the presence of a $C2$ and a $R\bar{3}m$ phases was mentioned in Chapter 7, no comparison was performed in here for these two phases with respect to the quantum $Fm\bar{3}m$ phase, since no stable harmonic phonons were found for both the $C2$ and the $R\bar{3}m$.

First the classical calculations related to the structure at the local minima of $V(\mathbf{R})$ were performed at the reference pressure. Subsequently, the SSCHA calculations were performed using as starting point the previously obtained classical structure. A structural relaxation was performed through the SSCHA maintaining the cell fixed to the classical results but allowing the atoms to move freely according to symmetry. Each classical structure was then compared with the structure obtained through the SSCHA relaxation. This procedure results valid because most of the structure in the dataset are highly symmetric and with a cubic cell. Thus the comparison is made between structures with the same volume. This procedure was performed for all systems but ScH_6-$Cmcm$.

The data for the ScH_6-$Cmcm$ phase at 100 GPa was not retrieved from the literature but was obtained performing additional calculations for the

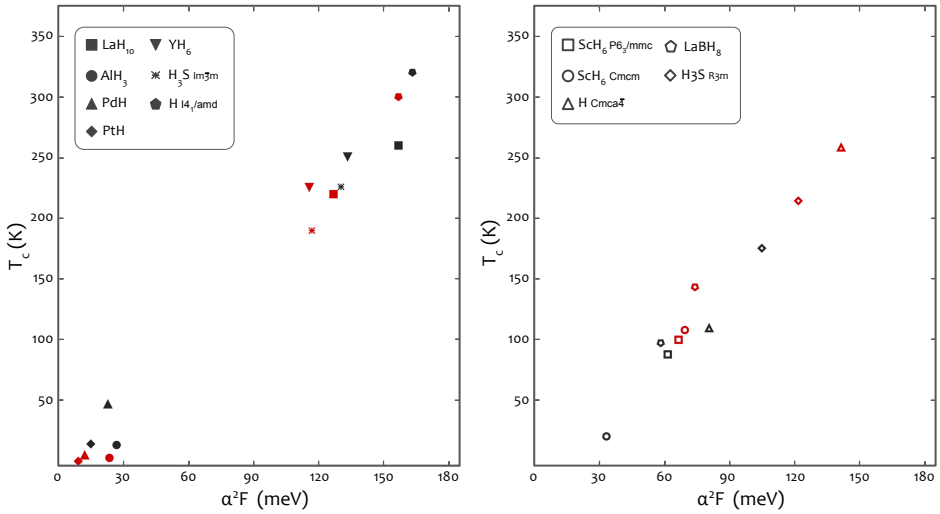

FIGURE 9.4 – The figure shows the value of T_c as a function of the integral of Eliashberg function. In black and red are reported respectively the results for the classical calculations and the calculations including quantum fluctuations. The left panel reports the results for the systems where quantum fluctuations do not introduce significant structural renormalizations. The right panel reports the results for the systems where quantum fluctuations significantly alter the crystal structure.

purpose of this study. The phonon specta for this structure at 100 GPa is shown in Appendix A.3. The starting point for the calculation was obtained considering the phonon spectra of the ScH_6-$P6_3/mmc$ phase at 100 GPa [198]. At this pressure the system becomes unstable in the classical approximation due to the imaginary frequency of a degenerate mode in Γ with symmetry E_{2g}. The structure of the ScH_6-$P6_3/mmc$ phase at 100 GPa was first displaced according to the eigenvectors related to the imaginary Γ mode using equations ((8.1)-(8.3)), with a procedure consistent with the one used in Chapter 8 for the $LaBH_8$ structure. An additional complete structural relaxation, where both atoms and cell parameters were allowed to relax, was later performed starting from the lowest local mimima related to the Γ degenerate mode. The resulting structure after the relaxation is shown in the lower panel of figure 9.1. A symmetry analysis revealed the structure to be part of the $Cmcm$ group with a precision of about 0.004 Å in the atomic coordinates. This structure was then confronted with the SSCHA calculations for the ScH_6-$P6_3/mmc$ phase at a classical pressure of 100 GPa. In this case then, the comparison between the two structures is not performed at the same volume.

The DFT calculations for the ScH_6-*Cmcm* structure are performed with the plane-wave Quantum ESPRESSO [180, 181] package using ultrasoft pseudo-potentials with the Perdew-Burke-Ernzerhof [182] parametrization of the exchange-correlation potential including 11 electrons of scandium in the valence. The cutoff for the wavefunctions and density are chosen as 80 Ry and 800 Ry, respectively. The integration over the Brillouin zone in the self-consistent calculations are performed with a first-order Methfessel-Paxton smearing of 0.02 Ry broadening and a 30×30×23 **k**-point grid. The harmonic phonon calculations are performed on a 6×6×4 phonon **q**-point grid making use of density functional perturbation theory [89]. The electron-phonon interaction is calculated on a 40×40×28 **k**-point grid, with a Gaussian smearing of 0.008 Ry to approximate the Dirac deltas in equation (3.29), and 6×6×4 **q**-point grid. The superconducting critical temperature is calculated by solving the Allen-Dynes equations with values of μ^* between 0.1 and 0.15 consistently with the study performed for the ScH_6-$P6_3/mmc$ phase [198]. The T_c for the system is 20 K and 9 K respectively for μ^* of 0.1 and 0.15 with a value of λ and ω_{log} of 0.558 and 94.14 meV.

9.3 EFFECTS OF QUANTUM FLUCTUATIONS OVER THE COMPOUNDS

The introduction of quantum fluctuations generates a variety of different effects on the structural and superconducting properties of the compounds. For PdH, PtH, AlH_3, atomic hydrogen $I4_1/amd$, and YH_6, due to the high symmetry of the materials where all atoms are locked in place, quantum fluctuations do not introduce structural renormalizations. However, the results show that quantum fluctuations tend to renormalize the phonon spectra and, for PdH, PtH, AlH_3, and YH_6, there is a blue shift of the phonon spectra which is more pronounced for the lower optical branches. The lower optical branches carrying a substantial part of the electron phonon interaction for these compounds. This can be more clearly seen in figure 9.2 reporting the values of the Eliashberg function $\alpha^2F(\omega)$ and the electron phonon coupling constant λ. Transitioning from the classical to quantum results, the value of T_c for these compounds decreases from 47 to 5 K for PdH, from 14.5 to 0.4 K for PtH, from 13.7 to 3 K for AlH_3, and from 251 to 226 for YH_6. For the atomic hydrogen $I4_1/amd$ quantum fluctuations produce a softening of the acoustic phonon branches but still lift the optical phonon branches. For this systems there seems not to be substantial variation in the value of λ, as can be seen from figure 9.2, and the value of the T_c varies from 320 to 300 K with the introduction of quantum fluctuations.

In the classical case, the H_3S structure exhibits an $Im\bar{3}m$ symmetry

above 175 GPa, transitioning to a distorted $R3m$ phase below that pressure. Both structures are shown in figure 9.1. The introduction of quantum fluctuations extend the stability of the $Im\bar{3}m$ phase to 103 GPa [161]. Comparing the $Im\bar{3}m$ phase in the classical and quantum cases at 250 GPa, the introduction of quantum fluctuations does not alter the structure due to the high symmetry of the system, forcing all atoms to be locked in place. The transition between the classical $R3m$, and the quantum $Im\bar{3}m$ phases at 130 GPa symmetrizes the hydrogen-sulphur bond increasing its distance from 1.46 to 1.56 Å. For the $Im\bar{3}m$ phase at 250 GPa, the introduction of quantum fluctuations creates a blue shift of the phonon spectra moving the contribution of $\alpha^2F(\omega)$ coming from these frequencies to higher values. In turn, this reduces the value of λ as can be seen in figure 9.2 and decreases the value of T_c from 226 K in the classical case to 190 K in the quantum case. In the transition between the classical R3m phase and the more symmetrical $Im\bar{3}m$ phase at 130 GPa, the structural variations induced by quantum effects soften the phonon specra, shifting the contributions to $\alpha^2F(\omega)$ at lower frequencies. This, in contrast with the high pressure case, produces an increment in λ which increases the T_c from 175 to 214 K from the classical to the quantum case.

For LaH_{10} the introduction of quantum fluctuations is able to alter the atomic positions. As shown in Chapter 7, the structure of LaH_{10} is not completely fixed by symmetry, but it can be described by a single free parameter related to the 32f Wyckoff site occupied by the hydrogen atoms. After the SSCHA relaxation however, it was observed that the variation in the hydrogen atomic positions are negligible. Ultimately, for this structure quantum fluctuations are not able to introduce significant structural renormalizations. Similarly to the compounds previously described, quantum fluctuations introduce a blue shift of the phonon spectra with consequent reduction of $\alpha^2F(\omega)$ and λ, as it can bee seen in figure 9.2. For this compound the value of T_c is reduced from 260 to 220 K with the introduction of quantum fluctuations.

The ScH_6 and molecular hydrogen $Cmca\bar{4}$ structures shown in figure 9.1 are composed by dislocated molecular hydrogen units which are then weakly bonded between each other. For the ScH_6-$P6_3/mmc$ phase at 140 GPa, the length of the hydrogen molecules varies from 1.02 to 1.07 Å with the introduction of quantum effects, while, for the molecular hydrogen $Cmca\bar{4}$ phase, the variation is from 0.78218 to 0.83236 Å. At 100 GPa the classical ScH_6-$P6_3/mmc$ phase undergoes a transition toward a distorted $Cmcm$ phase. The latter can be seen in figure 9.1 and retains many similarities to the ScH_6-$P6_3/mmc$. In the ScH_6-$Cmcm$ phase there is a breaking of the symmetry in the length of the various pairs of molecular hydrogen. The introduction of quantum fluctuations however, restores this symmetry and

recovers the ScH_6-$P6_3/mmc$ phase which is sustained till lower pressures. At 100 GPa, the length of the various pairs of molecular hydrogen for the classical ScH_6-$Cmcm$ phase is 1.28, 0.95 and 0.95 Å, which, with the introduction of quantum fluctuations, merge to 1.08 Å. For all these systems, the increment in the inter-atomic distances weakens the bonds between atoms and introduces a red shift of the phonon spectra, as can be seen in 9.2. These variations produce an overall increment of the value of $\alpha^2F(\omega)$, and consequently λ, which are particularly substantial for the transition between the ScH_6 Cmcm and $P6_3/mmc$ phases, and the molecular hydrogen $Cmca\bar{4}$ phase. Consequently, there is an increment in T_c from 20 to 108 K for the transition from ScH_6 $Cmcm$ to $P6_3/mmc$ phases, from 88 to 99 K for the internal structural variations in the ScH_6-$P6_3/mmc$ phase at 140 GPa, and from 109 to 258 K for the molecular hydrogen $Cmca\bar{4}$.

Finally, in the case of $LaBH_8$, which has already been described at length in Chapter 8, quantum fluctuations produce an increment of the boron-hydrogen bonding distance. As a result, there is a general red shift of the phonon spectra which produces an increment of the T_c from 97 to 143 at 100 GPa. However, there is also an increment of the lower pressure of stability from 40 GPa in the classical case to 77 GPa in presence of quantum fluctuation.

9.4 TRENDS FOR QUANTUM IONIC FLUCTUATIONS

Looking at figure 9.2, it can be noticed that the introduction of quantum fluctuations does not only produce a variation of the Eliashberg function $\alpha^2F(\omega)$ due to the shift of the phonons, but also introduces a variation in the total magnitude of its value. To better investigate this idea, attention was invested over the total integral of the Eliashberg function calculated as

$$\alpha^2F = \int_0^\infty \alpha^2F(\omega)d\omega. \tag{9.1}$$

This was done in order to understand the various differences introduced by the quantum ionic fluctuations in the systems. Figure 9.3 shows the value of T_c as a function of α^2F for both classical and quantum calculations of all the compounds previously presented. Surprisingly, the latter exhibits an extraordinary correlation with the former, especially when compared with λ and ω_{log} presented in the same figure. This suggests α^2F to be a good observable for this analysis, since it does not depend by the choice of μ^* in contrast to T_c, and it can capture the effects that the variations of the phonon spectra, due to quantum fluctuations, induce over the superconducting critical temperature.

Through the use of this quantity, the different kind of behaviors previously described can be divided in two classes. The first class is related to those systems for which quantum fluctuations do not alter the crystal structure. This is the case of PdH, PtH, AlH_3, H_3S-$Im\bar{3}m$ at 250 GPa, YH_6, atomic hydrogen $I4_1/amd$ and interestingly also LaH_{10}. The left panel of figure 9.4 shows the variations between the classical and quantum values of T_c as a function of α^2F. The figures suggest that the value of T_c is not only affected by the variation in energy of the phonon frequency, but that the changes in T_c come accompanied with a strong renormalization of the total integral of α^2F. Overall, these results show that the renormalization to the electron phonon coupling due to quantum fluctuations is significant, and suggest that in the cases in which the crystal structure is not altered by the "extra" space occupied by the atoms, the value of T_c will always decrease. For these systems, the "extra" space, arising from the quantum fluctuations, tends to stabilize the structure, and it leads to a blue shift of the phonon spectra. This feature is pronounced for the lower optical branches. The fact that LaH_{10} at 260 GPa is also part of this class suggests that the absence of structural renormalizations is not just due to the high symmetry of the atomic positions, but is more related to the symmetric properties of the Born-Oppenheimer potential $V(\mathbf{R})$. These highly symmetric states are achieved through very symmetric bonding patterns, as can be observed in the upper panel of figure 9.1.

The second class contains all systems for which the atomic structure is instead modified by the introduction of quantum fluctuations. This is the case for the molecular hydrogen $Cmca\bar{4}$, ScH_6-$P6_3/mmc$ at 140 GPa, the transition between ScH_6-$Cmcm$ and ScH_6-$P6_3/mmc$ at 100 GPa, the transition between H_3S-$R3m$ and H_3S-$Im\bar{3}m$ at 130 GPa, and $LaBH_8$. The values of T_c as a function of α^2F for both classical and quantum structure of this class are shown in the right panel of figure 9.4. The results show that the increment in the electron-phonon coupling introduced by quantum effects is absolutely non negligible. Overall, the value of T_c increases in all those systems in which quantum fluctuations introduce a renormalization of the crystal structure. In these cases, the systems move away from the local minima of $V(\mathbf{R})$ and sit in zones where the anharmonic contributions are more significant. This justifies the electron-phonon coupling seen in the right panel of figure 9.4. In addition, the renormalization of the structure causes a softening of the inter-atomic bonds that lead to an overall red shift of the phonon spectra. This effect leads to a further increment of the electron-phonon coupling. Interestingly, all these systems are composed by hydrogen molecules as in the case of ScH_6 or hydrogen $Cmca\bar{4}$, slight deformed high symmetry crystals as H_3S-$R3m$, or bonded units which are isolated from one another as in the case of $LaBH_8$.

In order to investigate if there is a correlation between the magnitude of the increment of $\alpha^2 F$ and the variation of the atomic positions, the behavior of the percentage variation in $\alpha^2 F$ as a function of the mean atomic displacement (ΔX) between classical and quantum calculations was investigated. In this case, ΔX is calculated as

$$\Delta X = \sum_{a}^{N_A} \frac{|\, \mathbf{X}_a^q - \mathbf{X}_a^c \,|}{N_A}, \tag{9.2}$$

where N_A represents the number of atoms in the unit cell, $\mathbf{X}_a^c$ is the position of the atoms at the local minimum of $V(\mathbf{R})$ and $\mathbf{X}_a^q$ represent the atomic positions after the SSCHA relaxation in presence of quantum fluctuations. The results of this analysis are reported in figure 9.5, and highlight that even if the variations in ΔX are small, they introduce extreme variations in the value of $\alpha^2 F$. Furthermore, this effect increases with the increment of ΔX. These different behaviour between the two classes allows in foresight to distinguish which effect will the introduction of quantum fluctuations have on T_c.

As final note it is important to mention that the current available calculation suggest that the introduction of quantum fluctuations do not necessarily extend the range of stability for the compounds to lower pressures. Although the stability of the system is sustained to lower pressures, thanks to the introduction of quantum fluctuations, for most of the compounds in this study, the case of $LaBH_8$, where quantum fluctuations destabilize the system at a pressure 77 GPa, which is higher then the classical case, disproves the presence of a consistent pattern. The relative metastability of the compound with respect to other phases may play a crucial role in order to understand whether or not quantum fluctuations are capable to sustain the structural stability down to lower pressures. Quantum fluctuations tend to smoothen the surface of the Born-Oppenheimer potential as seen in the case of LaH_{10}, and therefore allow the system to escape shallow energy traps. This suggest that the introduction of quantum effect will destabilize the system at higher pressures if different close minima of $V(\mathbf{R})$ are too far apart in energy and separated by shallow energy humps. Contrarily, if different phases sit close in energy, the introduction of quantum effects will allow the system to tunnel between the different phases. As a result, this will create a mixed equilibrium state as in the case of LaH_{10} [191] and H_3S [161] that will be sustained to lower pressure until the separation between the two metastable phases becomes too high or the system dissociates. Here comes an interesting compromise: by choosing isolated molecules interlaced by chemical precompressing atoms, one could hope that at moderate and low pressures the introductions of quantum effects will expand the

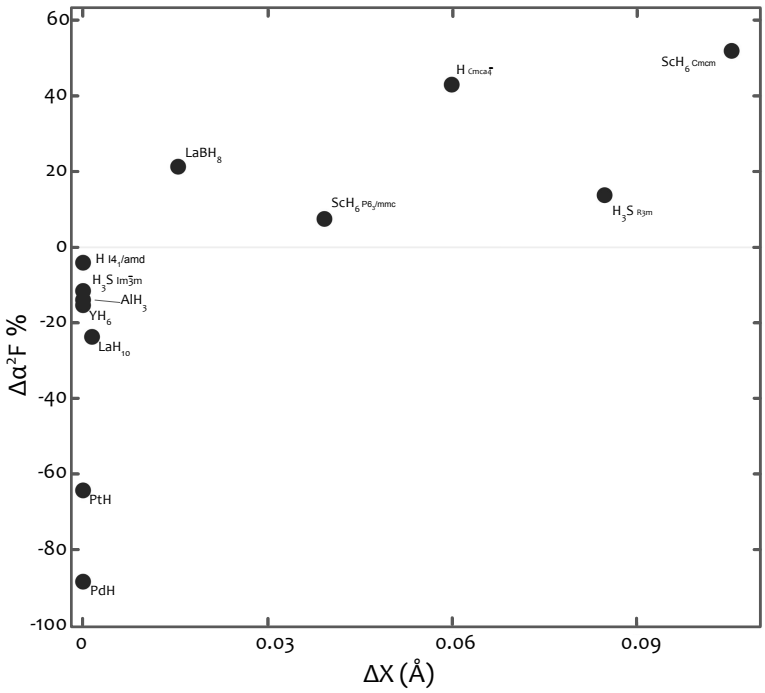

FIGURE 9.5 – The figure shows the percentage variation of the integral of $\alpha^2F(\omega)$ between quantum and classical calculations in function of the mean atomic displacement of equation (9.2). The data reported in the figure is related to all the system for which crystal symmetry allow the structure to be renormalized by quantum fluctuations.

length of the bonds increasing T_c. However, this comes at the cost of a possible decomposition to higher pressures. In contrast, systems with highly symmetric bonding patterns might have their pressure range extended to lower values thanks to quantum effects, but as a consequence, the value of their T_c will be decreased.

CHAPTER 10

Conclusions

This thesis exposes an extended analysis related to the properties of hydrogen rich superconductors. The analysis ranges from the general investigation of their electronic and structural trends to the effect of quantum ionic fluctuations over the phase stability and superconductivity.

Part II presents a classification of the structural, bonding and electronic properties for a large set of theoretically predicted hydrogen rich superconductors. In this analysis, the systems are divided into different families based on the specifics of their local bonding properties. The analysis highlights with clarity that the highest critical temperatures are achieved by systems possessing a high number of hydrogen atoms, high density of states, and dislocated weak covalent bonds. The highest critical temperatures appear between groups 1 to 5 of the periodic table, where bonds are mainly driven by covalent hydrogen-hydrogen interactions, and 13 to 16, where covalent bonds are predominantly between hydrogen and host atoms. A further analysis of the delocalization properties for the same set of hydrogen rich materials, performed with the use of the electron localization function, revealed that these systems show localized electrons, but with a high probability of being coupled. This led to the identification of the the networking value ϕ. This variable proves to be able to capture effectively how sensitive the electronic cloud is on average to lattice vibrations, and exhibits a good correlation with the critical temperature T_c. The networking value ϕ offers a simple way of screening hydrogen-based superconductors since it simply requires the analysis of ELF isosurfaces to be computed. The latter can be easily obtained post-processing DFT ground state calculations.

Furthermore, the networking value opens new avenues for the discovery of new hydrogen rich systems. The introduction of automated codes for the calculation of the networking value, combined with structural prediction methods, will speed up structural prediction by avoiding the calculation of the phonon properties of these compounds, and will allow to chose with foresight for which compounds it is worth to deepen the computational effort. Structural prediction methods could also be employed in order to search for structures that can maximize the ability of networking between atoms, according to the definition proposed with the networking value. Additionally, with the ever growing list of new predictions, linear regression methods could be used on an expanded dataset in order to sharpen the accuracy of prediction of the networking value, or perhaps used to identify more complex type of networking patterns to improve its definition.

Part III presents instead a general investigation of the effects of quantum ionic fluctuations over the phase stability and superconductivity of hydrogen rich compounds at high pressures. The investigation was performed using the stochastic self consistent harmonic approximation (SSCHA). The SSCHA allows a complete treatment of the quantum ionic fluctuations with the inclusion of the full Born-Oppenheimer potential surface, with the only approximation related to Gaussian ionic wave functions. Particular attention is invested over the properties of LaH_{10} and $LaBH_8$. In regard to LaH_{10}, it is shown how quantum effects are of capital importance in determining the ground state structure of the compound. They greatly simplify the landscape of structural stability, as shown by the natural evolution of the $R\bar{3}m$ and $C2$ phases towards the highly symmetric $Fm\bar{3}m$ phase. Furthermore, the stability of the $Fm\bar{3}m$ phase is sustained to much lower pressures with respect to the one obtained through classical Born-Oppenheimer results. For the $LaBH_8$ instead, it is shown that quantum fluctuations renormalize the distance of the hydrogen-boron bonds critically affecting the phase stability and superconducting properties. In this case, however, quantum fluctuations produce the opposite effect when compared with LaH_{10}. They destabilize the $Fm\bar{3}m$-$LaBH_8$ structure at much higher pressures while notably increasing the value of the critical temperature. The differences between the behavior of quantum effects on the two compounds sparked interest in performing a further generalized analysis on how the introduction of quantum fluctuations alter the result of the classical Born-Oppenheimer calculations. This is done by taking into consideration all systems for which quantum fluctuations have been treated through the SSCHA in the current state of literature. The obtained results show the presence of two main effects. On one hand quantum fluctuations introduce a renormalization of the crystal structure whenever the systems are composed by isolated bonded units with the possibility of expansion, slightly distorted structures

close to symmetrizaton, or structures with localized hydrogen-hydrogen bonds. These structural renormalizations ultimately lead to an increment in the value of the critical temperature. On the other hand, the critical temperature is expected to decrease whenever quantum fluctuations do not introduce structural renormalizations due to the high symmetry of the crystal, or due to a highly connected network of bonds. On one side, there is the hope that quantum fluctuations can sustain hydrogen based superconductors, with highly symmetric bonding patterns, down to low and close to ambient pressures. On the other side, quantum fluctuations could introduce structural modifications to systems at low pressures that can enhance their electron-phonon interaction and consequently boost the critical temperature predicted at low if not ambient pressure.

In conclusion the work performed in this thesis sheds light over the general properties of hydrogen based superconductors and hints at the flaws in the standard theoretical methods by illustrating how quantum fluctuations are indispensable to accurately describe the structural and superconducting properties. The knowledge acquired through this work sets clear guidelines related to atomic, structural and networking properties for good superconductivity in hydrogen rich compounds while provides computational useful tools to assist the calculations of the next years, contributing to the journey towards the north start of room temperature and room pressure superconductivity.

IV

Appendices

APPENDIX A

Appendix

A.1 Data tables

Table A.1 – Table reporting item number used in the manuscript, chemical formula, space group, superconducting critical temperature as predicted, pressure at which it has has been predicted, hydrogen fraction H_f, and the reference from which the T_c value has been extracted. The empty cells refer to missing values from the literature or to the impossibility to perform calculations.

Item	Chemical formula	Space group	T_c (K)	Pressure (GPa)	H_f	Reference
0	LiH_2	$P4/mbm$	0	150	0.667	[100]
1	LiH_6	$R\bar{3}m$	38.34	150	0.857	[100]
2	LiH_8	$I422$	31.04	100	0.889	[100]
3	KH_6	$C2/c$	69.8	166	0.857	[101]
4	BeH_2	$Cmcm$	44.1	250	0.667	[102]
5	BeH_2	$P4/nmm$	62	400	0.667	[102]
6	MgH_6	$Im\bar{3}m$	271	400	0.857	[103]
7	CaH_6	$Im\bar{3}m$	235	150	0.857	[104]
8	SrH_6	$R\bar{3}m$	156	250	0.857	[99]
9	BaH_2	$R\bar{3}m$	0	60	0.667	[106]
10	BaH_6	$P4/mmm$	38	70	0.857	[106]
11	ScH_3	–	19.3	18	0.750	[107]
12	LaH_3	$Cmcm$	22.5	11	0.750	[107]
13	YH_3	–	40	17	0.750	[107]

14	ScH_2	–	32.9	80	0.667	[108]
15	YH_4	$I4/mmm$	95	120	0.800	[109]
16	YH_6	$Im\bar{3}m$	264	120	0.857	[109]
17	ScH_4	$I4/mmm$	98	200	0.800	[110]
18	ScH_6	$Im\bar{3}m$	169	350	0.857	[111]
19	PrH_9	$F\bar{4}3m$	0	100	0.900	[34]
20	CeH_{10}	$Fm\bar{3}m$	168	94	0.909	[112]
21	CeH_9	$P6_3/mmc$	50	100	0.900	[34]
22	LaH_9	Cc	30	50	0.900	[34]
23	LaH_6	$R\bar{3}c$	170	100	0.857	[34]
24	YH_9	$P6_3/mmc$	250	150	0.900	[34]
25	ScH_9	$P6_3/mmc$	180	400	0.900	[34]
27	YH_{10}	$Fm\bar{3}m$	326	250	0.909	[32, 34]
28	LaH_4	$I4/mmm$	10	300	0.800	[32]
29	LaH_8	$C2/m$	131	300	0.889	[32]
30	LaH_{10}	$Fm\bar{3}m$	274	150	0.909	[32]
31	ScH_9	$I4_1md$	163	300	0.900	[111]
32	ScH_{10}	$Cmcm$	120	250	0.909	[111]
33	ScH_{12}	$Immm$	141	350	0.923	[111]
34	ScH_7	$Cmcm$	169	300	0.875	[111]
35	ScH_3	$P6_3/mmc$	1	400	0.750	[111]
36	ScH_2	$P6/mmm$	4	300	0.667	[111]
37	ScH_6	$P6_3/mmc$	119	130	0.857	[99]
38	$TiD_{0.74}$	–	4.43	30	0.425	[113]
39	TiH_2	$Fm\bar{3}m$	7	0	0.667	[114]
40	TiH_2	$I4/mmm$	0	0	0.667	[114]
41	ZrH	$Cmcm$	11	120	0.500	[115]
42	HfH_2	$I4/mmm$	0	0	0.667	[116]
43	HfH_2	$Cmma$	8	180	0.667	[116]
44	HfH_2	$P2_1/m$	12	260	0.667	[116]
45	NbH_2	$P6_3mc$	0.5	60	0.667	[117]
46	VH_2	$Fm\bar{3}m$	0.5	0	0.667	[117]
47	NbH_2	$Fm\bar{3}m$	1.5	0	0.667	[117]
48	NbH_2	$Pnma$	4	60	0.667	[117]
49	NbH_4	$I4/mmm$	47	300	0.800	[118]
50	TaH_2	$Pnma$	7.1	200	0.667	[119]
51	TaH_4	$R\bar{3}m$	31	250	0.800	[119]
52	TaH_6	$Fdd2$	135.8	300	0.857	[119]
53	CrH	$P6_3/mmc$	10.6	0	0.500	[120]
54	CrH_3	$P6_3/mmc$	37.1	81	0.750	[120]
55	TcH_2	$I4/mmm$	10.64	200	0.667	[121]
56	TcH_2	$Cmcm$	8.61	300	0.667	[121]

57	TcH_3	$P4_2/mmc$	9.94	300	0.750	[121]
58	FeH_6	$Cmmm$	42.9	150	0.857	[122]
59	FeH_5	$I4/mmm$	45.8	150	0.833	[122]
60	FeH_5	$I4/mmm$	51	130	0.833	[123]
61	RuH	$Fm\bar{3}m$	0.41	100	0.500	[124]
62	RuH_3	$Pm\bar{3}m$	3.57	100	0.750	[124]
63	RuH_3	$Pm\bar{3}n$	1.25	200	0.750	[124]
64	OsH	$Fm\bar{3}m$	2.1	100	0.500	[125]
65	CoH	$Fm\bar{3}m$	0.11	5	0.500	[126]
66	RhH	$Fm\bar{3}m$	2.5	4	0.500	[99]
67	IrH	$Fm\bar{3}m$	7	80	0.500	[99]
68	PdH	–	9	0	0.500	[45]
69	PdD	–	11	0	0.500	[45]
70	PdH	$Fm\bar{3}m$	5	0	0.500	[61]
71	PdD	$Fm\bar{3}m$	6.5	0	0.500	[61]
72	PdT	$Fm\bar{3}m$	6.9	0	0.500	[61]
73	PtH	$Fm\bar{3}m$	15	100	0.500	[61]
74	PtH	$P6_3/mmc$	25	80	0.500	[61]
75	AuH	$Fm\bar{3}m$	21	220	0.500	[99]
76	BH	$P6/mmm$	21.4	175	0.500	[127]
77	BH_3	$Pbcn$	125	360	0.750	[128]
78	AlH_3	$Pm\bar{3}n$	11.5	73	0.750	[47, 129]
79	$AlH_3(H_2)$	$P2_1/m$	146	250	0.750	[130]
80	GaH_3	$Pm\bar{3}n$	102	120	0.750	[131]
81	InH_5	$P2_1/m$	27.1	150	0.833	[132]
82	InH_3	$R\bar{3}$	40.5	200	0.750	[132]
83	SiH_4	$C2/c$	55	125	0.800	[133]
84	SiH_4	$P6/mmm$	74	120	0.800	[134]
85	SiH_4	$Pmna$	166	202	0.800	[135]
86	SiH_4	$C2/c$	30	300	0.800	[136]
87	SiH_4	$P2_1/c$	35	400	0.800	[136]
88	SiH_4	$C2/m$	110	610	0.800	[136]
89	SiH_4	$P\bar{3}$	35.1	300	0.800	[136]
90	SiH_4	$Cmca$	20	150	0.800	[137]
91	SiH_4	$Pbcn$	16.5	190	0.800	[138]
92	SiH_4H_2	$Cmca$	107	250	0.857	[139]
93	Si_2H_6	$P\bar{1}$	80	200	0.750	[140]
94	Si_2H_6	$Pm\bar{3}m$	153	275	0.750	[140]
95	Si_2H_6	$C2/c$	42	300	0.750	[140]
96	Si_2H_6	$Cmcm$	25	100	0.750	[141]
97	GeH_4	$C2/c$	64	220	0.800	[142]
98	GeH_4	$Cmmm$	47	20	0.800	[143]

99	GeH_4	$Ama2$	57	250	0.800	[144]
100	GeH_4	$C2/c$	84	500	0.800	[144]
101	$GeH_4(H_2)2$	$P2_1/c$	90	250	0.889	[145]
102	GeH_3	$Cccm$	80	300	0.857	[146]
103	GeH_4	$C2/m$	67	280	0.800	[147]
104	$Ge3H_{11}$	$I\bar{4}m2$	43	285	0.786	[147]
105	GeH_3	$P4_2/mmc$	90	180	0.750	[148]
106	GeH_3	$Pm\bar{3}m$	140	180	0.750	[148]
107	SnH_8	$I\bar{4}m2$	72	250	0.889	[149]
108	SnH_4	$Ama2$	22	120	0.800	[150]
109	SnH_4	$P6_3/mmc$	62	200	0.800	[150]
110	SnH_4	$P6/mmm$	80	120	0.800	[151]
111	SnH_4	$C2/m$	95	600	0.800	[152]
112	SnH_4	$I4/mmm$	91	220	0.800	[153]
113	SnH_{12}	$C2/m$	93	250	0.923	[153]
114	SnH_{14}	$C2/m$	97	300	0.933	[153]
115	$PbH_4(H_2)2$	$C2/m$	107	230	0.889	[153]
116	PH_3	0	100	226	0.750	[200]
117	PH	$I4/mmm$	81	250	0.500	[154]
118	PH_2	$I4/mmm$	86	260	0.667	[154, 155]
119	PH_4	$C2/m$	1.9	80	0.800	[156]
120	PH_2	$Cmmm$	29.5	80	0.667	[157]
121	AsH	$Cmcm$	21.2	300	0.500	[158]
122	AsH_8	$C2/c$	151.4	450	0.889	[158]
123	SbH	$Pnma$	14.6	175	0.500	[158]
124	SbH_3	$Pmmn$	25.9	300	0.750	[158]
125	SbH_4	$P6_3/mmc$	102.2	150	0.800	[158]
126	BiH_2	$Pnma$	39	125	0.667	[159]
127	BiH_3	$I4_1/amd$	65	270	0.750	[159]
128	SbH_3	$Pnma$	68	170	0.750	[159]
129	BiH	$P6_3/mmc$	30	250	0.500	[201]
130	BiH_2	$P2_1/m$	65	300	0.667	[201]
131	BiH_4	$Pmmm$	93	150	0.800	[201]
132	BiH_5	$C2/m$	119	300	0.833	[201]
133	BiH_6	$P\bar{1}$	113	300	0.857	[201]
134	H_2S	$Cmca$	82	160	0.500	[160]
135	H_2S	$P\bar{1}$	60	158	0.500	[160]
136	$(H_2S)2H_2$	$Im\bar{3}m$	204	200	0.750	[30]
137	$(H_2S)2H_2$	$R\bar{3}m$	166	130	0.750	[30]
138	H_3S	$Im\bar{3}m$	225	150	0.750	[161]
139	H_3S	$R\bar{3}m$	214	170	0.750	[162]
140	H_4S_3	$Pnma$	2.1	140	0.571	[163]

141	H_5S_2	$P\bar{1}$	79	130	0.714	[164]
142	D_3S	$Im\bar{3}m$	188	200	0.750	[165]
143	$H_3S_{0.925}P_{0.075}$	$Im\bar{3}m$	280	250	0.750	[166]
144	$H_3S_{0.9}P_{0.1}$	$Im\bar{3}m$	240	200	0.750	[166]
145	$H_3S_{0.96}Si_{0.04}$	$Im\bar{3}m$	275	250	0.750	[166]
146	HSe_2	$C2/m$	5	300	0.333	[167]
147	HSe	$P4/nmm$	42	300	0.500	[167]
148	H_3Se	$Im\bar{3}m$	116	200	0.750	[167]
149	HSe	$P2_1/c$	23	300	0.500	[167]
150	H_4Te	$P6/mmm$	104	170	0.800	[168]
151	H_5Te_2	$C2/m$	58	200	0.714	[168]
152	HTe	$P4/nmm$	28	150	0.500	[168]
153	H_4Te	$R\bar{3}m$	76	270	0.800	[168]
154	HTe	$P6_3/mmc$	44.2	300	0.500	[168]
155	PoH_4	$C2/c$	53.6	250	0.800	[169]
156	PoH	$P6_3/mmc$	0.65	300	0.500	[169]
157	PoH_2	$Pnma$	0	200	0.667	[169]
158	PoH_6	$C2/m$	4.68	200	0.857	[169]
159	HBr	$P2_1/m$	51	200	0.500	[170]
160	HCl	$P2_1/m$	40	360	0.500	[170]
161	HBr	$C2/m$	27	150	0.500	[171]
162	HCl	$C2/m$	20	250	0.500	[172]
163	H_2I	$Cmcm$	8	100	0.667	[173]
164	H_4I	$P6/mmm$	12.5	300	0.800	[174]
165	H_2I	$Pnma$	5.3	100	0.667	[174]
166	H_2I	$R\bar{3}m$	33	240	0.667	[174]
167	XeH	$Immm$	28	100	0.500	[175]
168	XeH_2	$Cmcm$	26	400	0.667	[175]
169	MgH_2	$P6_3/mmc$	23	180	0.667	[176]
170	MgH_4	$Cmcm$	37	100	0.800	[176]
171	MgH_{12}	$R\bar{3}$	60	140	0.923	[176]
172	PH_3	$C2/m$	71	260	0.750	[177, 178]
173	PH_2	$C2/m$	95	260	0.667	[177, 178]
174	H_2Br	$Cmcm$	12.1	240	0.667	[202]
175	H_4Br	$P6_3/mmc$	2.4	240	0.800	[202]
176	H	$I4_1/amd$	318	500	1.000	[35]
177	H	$Cmca\bar{4}$	109	450	1.000	[179]

TABLE A.2 – Table reporting the item index, chemical formula, networking value ϕ, dominant bonding family assigned, and shortest H-H distance for all the compounds. The empty cells refer to missing values from the literature or to the impossibility to perform calculations .

Item	Chemical formula	*Networking value* ϕ	Dominant bonding family	H-H Distance (Å)
0	LiH_2	0.24	Molecular	0.759
1	LiH_6	0.37	Molecular	0.803
2	LiH_8	0.15	Molecular	0.8235
3	KH_6	0.19	Molecular	0.887
4	BeH_2	0.35	Ionic	1.421
5	BeH_2	0.4	Ionic	1.345
6	MgH_6	0.63	Weak H Interactions	1.093
7	CaH_6	0.62	Weak H Interactions	1.237
8	SrH_6	0.33	Weak H Interactions	1.033
9	BaH_2	-	-	-
10	BaH_6	-	-	-
11	ScH_3	-	-	-
12	LaH_3	-	-	-
13	YH_3	-	-	-
14	ScH_2	0.33	Ionic	2.091
15	YH_4	0.43	Weak H Interactions	1.352
16	YH_6	0.58	Weak H Interactions	1.301
17	ScH_4	0.48	Weak H Interactions	1.198
18	ScH_6	0.6	Weak H Interactions	1.112
19	PrH_9	0.49	Weak H Interactions	0.944
20	CeH_{10}	0.51	Weak H Interactions	0.963
21	CeH_9	0.51	Weak H Interactions	0.909
22	LaH_9	0.13	Molecular	0.550
23	LaH_6	-	-	0.944
24	YH_9	0.57	Weak H Interactions	1.045
25	ScH_9	0.65	Weak H Interactions	0.983
27	YH_{10}	0.58	Weak H Interactions	1.047
28	LaH_4	-	-	1.189
29	LaH_8	0.52	Weak H Interactions	0.890
30	LaH_{10}	0.52	Weak H Interactions	0.840
31	ScH_9	0.59	Molecular	0.848
32	ScH_{10}	0.33	Molecular	0.866
33	ScH_{12}	0.33	Molecular	0.909
34	ScH_7	0.49	Molecular	0.960
35	ScH_3	-	-	-

36	ScH_2	-	-	-
37	ScH_6	0.26	Molecular	1.022
38	$TiD_{0.74}$	-	-	-
39	TiH_2	0.29	Ionic	2.210
40	TiH_2	0.38	Ionic	1.628
41	ZrH	0.32	Ionic	2.753
42	HfH_2	0.23	Ionic	2.149
43	HfH_2	0.23	Molecular	0.765
44	HfH_2	0.27	Isolated	1.359
45	NbH_2	0.29	Electride	2.009
46	VH_2	0.3	Ionic	2.105
47	NbH_2	0.27	Ionic	2.277
48	NbH_2	0.36	Electride	1.833
49	NbH_4	0.27	Weak H Interactions	1.209
50	TaH_2	0.41	Electride	1.728
51	TaH_4	0.27	Isolated	1.313
52	TaH_6	0.38	Weak H Interactions	1.085
53	CrH	0.4	Electride	2.171
54	CrH_3	0.35	Isolated	1.615
55	TcH_2	-	-	1.700
56	TcH_2	-	-	1.241
57	TcH_3	0.31	Isolated	1.299
58	FeH_6	0.36	Molecular	0.733
59	FeH_5	0.17	Weak H Interactions	1.300
60	FeH_5	-	-	-
61	RuH	0.28	Isolated	2.626
62	RuH_3	0.29	Isolated	1.807
63	RuH_3	0.29	Isolated	1.542
64	OsH	0.33	Ionic	2.676
65	CoH	0.27	Metallic	2.570
66	R_HH	-	-	-
67	IrH	-	-	-
68	PdH	0.19	Isolated	2.911
69	PdD	-	-	-
70	PdH	0.19	Isolated	2.911
71	PdD	-	-	-
72	PdT	-	-	-
73	PtH	0.27	Isolated	2.723
74	PtH	0.27	Ionic	2.563
75	AuH	0.27	Isolated	2.649
76	BH	0.51	Covalent	-
77	BH_3	0.56	Covalent	1.024

78	AlH_3	0.36	Covalent	1.593
79	$AlH_3(H_2)$	-	-	0.842
80	GaH_3	0.37	Covalent	1.531
81	InH_5	0.27	Molecular	0.770
82	InH_3	0.28	Molecular	0.884
83	SiH_4	0.27	Covalent	1.435
84	SiH_4	0.51	Covalent	1.081
85	SiH_4	-	-	-
86	SiH_4	-	-	-
87	SiH_4	0.45	Covalent	1.043
88	SiH_4	0.49	Covalent	1.009
89	SiH_4	0.49	Molecular	0.750
90	SiH_4	-	-	-
91	SiH_4	0.32	Covalent	1.372
92	SiH_4H_2	-	-	-
93	Si_2H_6	0.48	Covalent	1.247
94	Si_2H_6	0.58	Electride	1.592
95	Si_2H_6	0.48	Molecular	0.592
96	Si_2H_6	-	-	-
97	GeH_4	0.39	Molecular	0.878
98	GeH_4	-	-	-
99	GeH_4	0.34	Molecular	0.803
100	GeH_4	0.4	Covalent	0.973
101	$GeH_4(H_2)2$	0.37	Molecular	0.845
102	GeH_3	-	-	-
103	GeH_4	0.33	Covalent	1.057
104	$Ge3H_{11}$	0.31	Covalent	1.287
105	GeH_3	0.31	Covalent	1.360
106	GeH_3	0.32	Covalent	1.553
107	SnH_8	0.24	Molecular	0.860
108	SnH_4	0.22	Molecular	0.792
109	SnH_4	0.24	Molecular	0.816
110	SnH_4	-	-	-
111	SnH_4	0.29	Molecular	0.807
112	SnH_4	-	-	-
113	SnH_{12}	0.34	Molecular	0.754
114	SnH_{14}	0.37	Molecular	0.783
115	$PbH_4(H_2)2$	0.27	Molecular	0.789
116	PH_3	-	-	-
117	PH	-	-	-
118	PH_2	-	-	-
119	PH_4	0.19	Molecular	0.740

120	PH_2	0.15	Molecular	0.741
121	AsH	0.45	Covalent	1.580
122	AsH_8	0.39	Molecular	0.813
123	SbH	0.35	Covalent	1.905
124	SbH_3	0.27	Weak H Interactions	0.882
125	SbH_4	0.29	Molecular	0.842
126	BiH_2	0.32	Molecular	0.805
127	BiH_3	0.31	Weak H Interactions	0.924
128	SbH_3	0.35	Molecular	0.878
129	BiH	0.29	Isolated	3.033
130	BiH_2	0.31	Molecular	0.812
131	BiH_4	0.29	Molecular	0.834
132	BiH_5	-	-	-
133	BiH_6	0.37	Molecular	0.905
134	H_2S	-	-	-
135	H_2S	-	-	-
136	$(H_2S)2H_2$	0.69	Covalent	1.493
137	$(H_2S)2H_2$	-	-	-
138	H_3S	0.7	Covalent	1.532
139	H_3S	-	-	-
140	H_4S_3	0.44	Covalent	1.554
141	H_5S_2	0.56	Covalent	1.543
142	D_3S	-	-	-
143	$H_3S_{0.925}P_{0.075}$	-	-	-
144	$H_3S_{0.9}P_{0.1}$	-	-	-
145	$H_3S_{0.96}Si_{0.04}$	-	-	-
146	HSe_2	0.44	Covalent	1.762
147	HSe	0.52	Covalent	2.133
148	H_3Se	0.53	Covalent	1.571
149	HSe	0.52	Covalent	1.277
150	H_4Te	0.4	Molecular	0.844
151	H_5Te_2	0.41	Weak H Interactions	0.916
152	HTe	0.41	Covalent	2.465
153	H_4Te	0.35	Molecular	0.832
154	HTe	0.37	Molecular	0.834
155	PoH_4	0.34	Molecular	0.813
156	PoH	0.34	Ionic	2.335
157	PoH_2	0.35	Molecular	0.792
158	PoH_6	0.36	Molecular	0.797
159	HBr	0.37	Covalent	1.411
160	HCl	0.37	Covalent	1.266
161	HBr	0.38	Covalent	1.492

162	HCl	0.38	Covalent	1.403
163	H_2I	0.36	Molecular	0.792
164	H_4I	0.45	Molecular	0.799
165	H_2I	0.36	Molecular	0.797
166	H_2I	0.35	Molecular	0.797
167	XeH	-	-	-
168	XeH_2	-	-	-
169	MgH_2	0.33	Ionic	1.763
170	MgH_4	0.26	Molecular	0.776
171	MgH_{12}	0.36	Molecular	0.819
172	PH_3	-	-	-
173	PH_2	0.39	Covalent	1.4022
174	H_2Br	-	-	-
175	H_4Br	-	-	-
176	H	0.64	Weak H Interactions	0.985
177	H	0.35	Molecular	0.779

TABLE A.3 – Table reporting the item index, chemical formula, total DOS per electron, hydrogen contribution to the DOS per hydrogen atom, and hydrogen fraction of the DOS at the Fermi energy. The empty cells refer to missing values from the literature or to the impossibility to perform calculations.

Item	Chemical formula	Total DOS (eV^{-1})	Hydrogen DOS (eV^{-1})	Hydrogen DOS fraction
0	LiH_2	0.00298	0.00709	0.94924
1	LiH_6	0.02220	0.02933	0.88063
2	LiH_8	0.03063	0.039	0.92588
3	KH_6	0.05004	0.1429	0.87854
4	BeH_2	0.01675	0.02111	0.42005
5	BeH_2	0.01743	0.02091	0.39974
6	MgH_6	0.02064	0.0408	0.74105
7	CaH_6	0.01872	0.0456	0.91338
8	SrH_6	0.01656	0.038	0.86045
9	BaH_2	-	-	-
10	BaH_6	-	-	-
11	ScH_3	-	-	-
12	LaH_3	-	-	-
13	YH_3	-	-	-
14	ScH_2	0.03600	0.00638	0.02726
15	YH_4	0.03105	0.04555	0.39112
16	YH_6	0.04132	0.053	0.45269
17	ScH_4	0.03179	0.0356	0.29856
18	ScH_6	0.03896	0.0356	0.32246
19	PrH_9	0.01967	0.01129	0.16150
20	CeH_{10}	0.01466	0.01309	0.27900
21	CeH_9	0.02029	0.02036	0.29135
22	LaH_9	0.03072	0.01651	0.16123
23	LaH_6	-	-	-
24	YH_9	0.02762	0.04033	0.65701
25	ScH_9	0.02564	0.03135	0.55013
27	YH_{10}	0.03547	0.04992	0.67017
28	LaH_4	-	-	-
29	LaH_8	0.01605	0.02265	0.38922
30	LaH_{10}	0.02601	0.04064	0.50395
31	ScH_9	0.02952	0.03491	0.53215
32	ScH_{10}	0.02176	0.02453	0.53668
33	ScH_{12}	0.02376	0.02673	0.58697
34	ScH_7	0.02505	0.03605	0.55962
35	ScH_3	-	-	-

36	ScH_2	-	-	-
37	ScH_6	0.02758	0.0336	0.42992
38	$TiD_{0.74}$	-	-	-
39	TiH_2	0.17927	0.00066	0.00053
40	TiH_2	0.05533	0.01472	0.03800
41	ZrH	0.07636	0.01206	0.01214
42	HfH_2	0.01242	0.00186	0.00787
43	HfH_2	0.01072	0.02352	0.11542
44	HfH_2	0.00907	0.01225	0.07105
45	NbH_2	0.03424	0.00216	0.00844
46	VH_2	0.08699	0.00352	0.00539
47	NbH_2	0.06102	0.00306	0.00668
48	NbH_2	0.06066	0.00522	0.01147
49	NbH_4	0.04581	0.021	0.10784
50	TaH_2	0.02064	0.0091	0.03040
51	TaH_4	0.01307	0.02355	0.23240
52	TaH_6	0.01519	0.0403	0.48226
53	CrH	0.06706	0.0064	0.00636
54	CrH_3	0.07060	0.0282	0.07048
55	TcH_2	-	-	-
56	TcH_2	-	-	-
57	TcH_3	0.03144	0.0138	0.07314
58	FeH_6	0.02460	0.01662	0.18419
59	FeH_5	0.02408	0.00616	0.06091
60	FeH_5	-	-	-
61	RuH	0.04832	0.0133	0.01618
62	RuH_3	0.04596	0.024	0.08244
63	RuH_3	0.02571	0.022	0.13508
64	OsH	0.02037	0.00498	0.00788
65	CoH	0.24733	0.02135	0.00479
66	R_HH	-	-	-
67	IrH	-	-	-
68	PdH	0.02481	0.0745	0.15803
69	PdD	-	-	-
70	PdH	0.02481	0.0745	0.15803
71	PdD	-	-	-
72	PdT	-	-	-
73	PtH	0.01163	0.0562	0.14640
74	PtH	0.01735	0.047	0.08208
75	AuH	0.02019	0.01531	0.02230
76	BH	0.02755	0.03	0.27223
77	BH_3	0.02614	0.028	0.53550

78	AlH_3	0.03379	0.0458	0.67764
79	$AlH_3(H_2)$	-	-	-
80	GaH_3	0.01841	0.0208	0.56491
81	InH_5	0.02133	0.02644	0.34432
82	InH_3	0.02221	0.03366	0.28419
83	SiH_4	0.03007	0.0359	0.59684
84	SiH_4	0.05725	0.0464	0.40524
85	SiH_4	-	-	-
86	SiH_4	-	-	-
87	SiH_4	0.02126	0.02338	0.54972
88	SiH_4	0.03087	0.02732	0.44245
89	SiH_4	0.03394	0.01705	0.25117
90	SiH_4	-	-	-
91	SiH_4	0.0195	0.0243	0.62307
92	SiH_4H_2	-	-	-
93	Si_2H_6	0.03554	0.0297	0.35811
94	Si_2H_6	0.04522	0.0392	0.37144
95	Si_2H_6	0.04734	0.03976	0.35998
96	Si_2H_6	-	-	-
97	GeH_4	0.01901	0.0314	0.36688
98	GeH_4	-	-	-
99	GeH_4	0.01805	0.03362	0.41384
100	GeH_4	0.01439	0.03255	0.50236
101	$GeH_4(H_2)2$	0.01920	0.0279	0.52831
102	GeH_3	-	-	-
103	GeH_4	0.01449	0.02803	0.42974
104	$Ge3H_{11}$	0.01079	0.02473	0.47560
105	GeH_3	0.02187	0.03453	0.27853
106	GeH_3	0.03444	0.0484	0.24793
107	SnH_8	0.01736	0.02607	0.54617
108	SnH_4	0.01782	0.0241	0.30038
109	SnH_4	0.0223	0.0372	0.37070
110	SnH_4	-	-	-
111	SnH_4	0.01920	0.0331	0.38303
112	SnH_4	-	-	-
113	SnH_{12}	0.02066	0.02871	0.64144
114	SnH_{14}	0.02083	0.02999	0.71983
115	$PbH_4(H_2)2$	0.02688	0.03232	0.43717
116	PH_3	-	-	-
117	PH	-	-	-
118	PH_2	-	-	-
119	PH_4	0.02710	0.01734	0.28436

120	PH_2	0.03010	0.01784	0.16935
121	AsH	0.01920	0.052	0.16926
122	AsH_8	0.02111	0.03243	0.53430
123	SbH	0.02155	0.0482	0.13976
124	SbH_3	0.01877	0.037	0.62715
125	SbH_4	0.03026	0.0465	0.32348
126	BiH_2	0.02709	0.0446	0.19364
127	BiH_3	0.02584	0.0537	0.34636
128	SbH_3	0.02447	0.0408	0.27787
129	BiH	0.02447	0.09	0.22987
130	BiH_2	0.02626	0.0485	0.21725
131	BiH_4	0.02858	0.0402	0.29603
132	BiH_5	-	-	-
133	BiH_6	0.02549	0.04146	0.46471
134	H_2S	-	-	-
135	H_2S	-	-	-
136	$(H_2S)2H_2$	0.06064	0.0867	0.47654
137	$(H_2S)2H_2$	-	-	-
138	H_3S	0.05348	0.0782	0.48732
139	H_3S	-	-	-
140	H_4S_3	0.01120	0.01403	0.22762
141	H_5S_2	0.03182	0.0442	0.40847
142	D_3S	-	-	-
143	$H_3S_{0.925}P_{0.075}$	-	-	-
144	$H_3S_{0.9}P_{0.1}$	-	-	-
145	$H_3S_{0.96}Si_{0.04}$	-	-	-
146	HSe_2	0.01736	0.0819	0.14294
147	HSe	0.02240	0.0544	0.14283
148	H_3Se	0.02796	0.0857	0.48394
149	HSe	0.01874	0.0494	0.15501
150	H_4Te	0.03724	0.0464	0.24914
151	H_5Te_2	0.02416	0.04592	0.25675
152	HTe	0.02680	0.065	0.14264
153	H_4Te	0.02674	0.0381	0.28495
154	HTe	0.03070	0.0424	0.27614
155	PoH_4	0.02522	0.0359	0.28468
156	PoH	0.02491	0.0864	0.20401
157	PoH_2	0.02682	0.0405	0.16772
158	PoH_6	0.03239	0.03846	0.32384
159	HBr	0.01632	0.052	0.17697
160	HCl	0.01352	0.0432	0.17748
161	HBr	0.01836	0.0454	0.13735

162	HCl	0.03575	0.0388	0.13565
163	H_2I	0.02955	0.0269	0.09580
164	H_4I	0.01606	0.0262	0.31063
165	H_2I	0.02681	0.0298	0.11697
166	H_2I	0.02684	0.042	0.16466
167	XeH	-	-	-
168	XeH_2	-	-	-
169	MgH_2	0.00801	0.01701	0.35378
170	MgH_4	0.00576	0.01346	0.66683
171	MgH_{12}	0.01311	0.0221	0.91945
172	PH_3	-	-	-
173	PH_2	0.04305	0.061	0.40477
174	H_2Br	-	-	-
175	H_4Br	-	-	-
176	H	0.03300	0.033	1
177	H	0.01878	0.01878	1

A.2 EXAMPLES OF NETWORKS

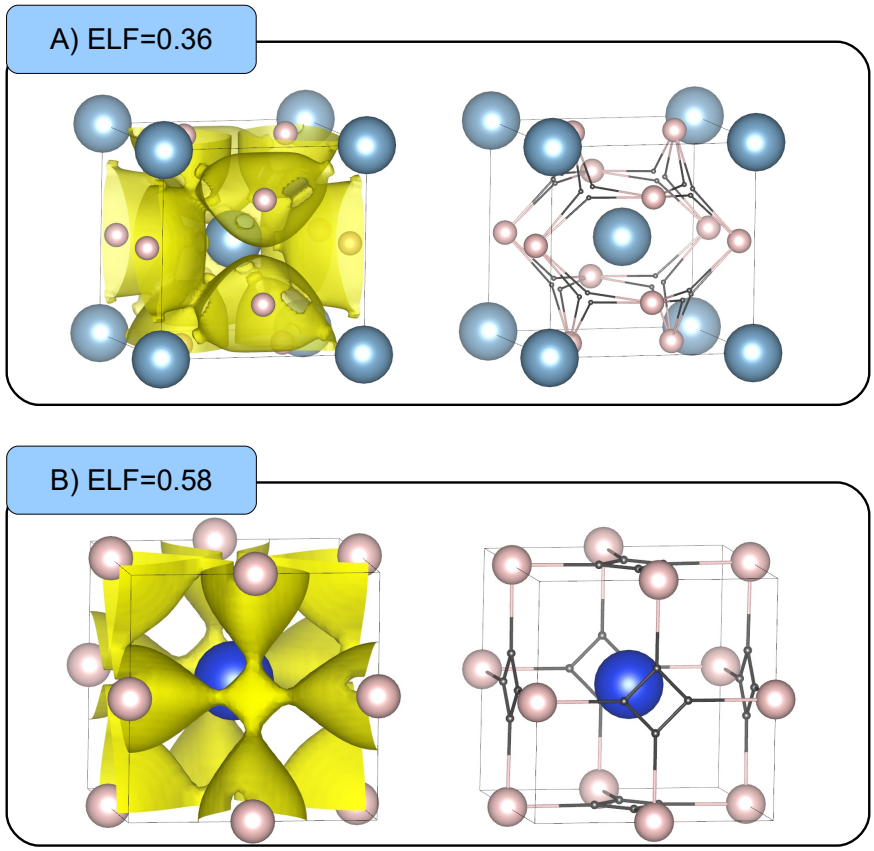

FIGURE A.1 – The figure shows an example of a network arising from covalent bonds as in A) for AlH_3 (78), with $\phi = 0.36$, and an example of a network arising from an electride bonding pattern as in B) for Si_2H_6 (94), with $\phi = 0.58$.

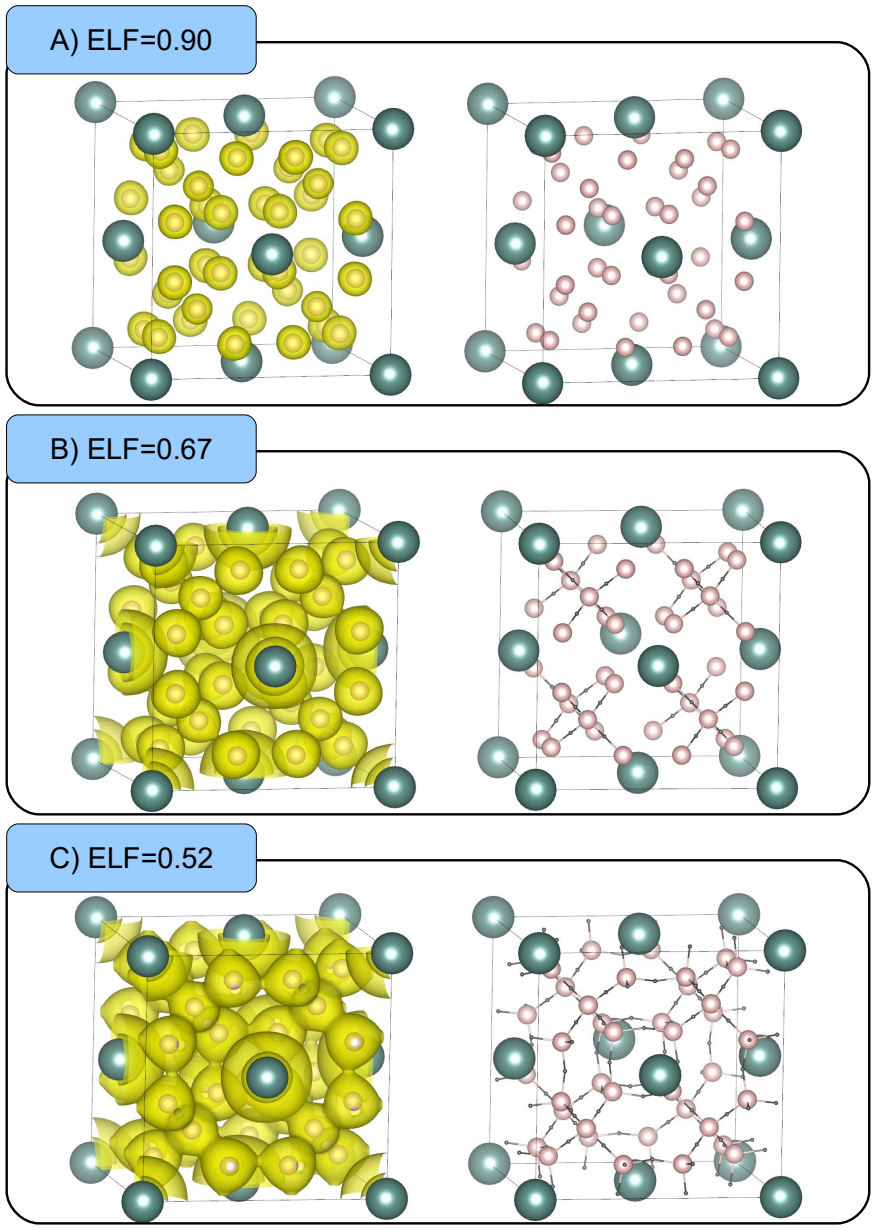

FIGURE A.2 – The figure shows the steps for the construction of the network for LaH_{10} (30). On the left side the ELF isosurfaces are visualized, while on the right side the network patterns are shown. The latter are identified through the selection of the saddle points (small black dots) related to the same and higher value of ELF with respect to the ELF threshold in the blue box. In step A) no bond is formed. In step B) few isolated bonding patterns appear. In step C) the highest 3D network spanning through the entire cell is created. The resulting network is constructed by all the hydrogen atoms.

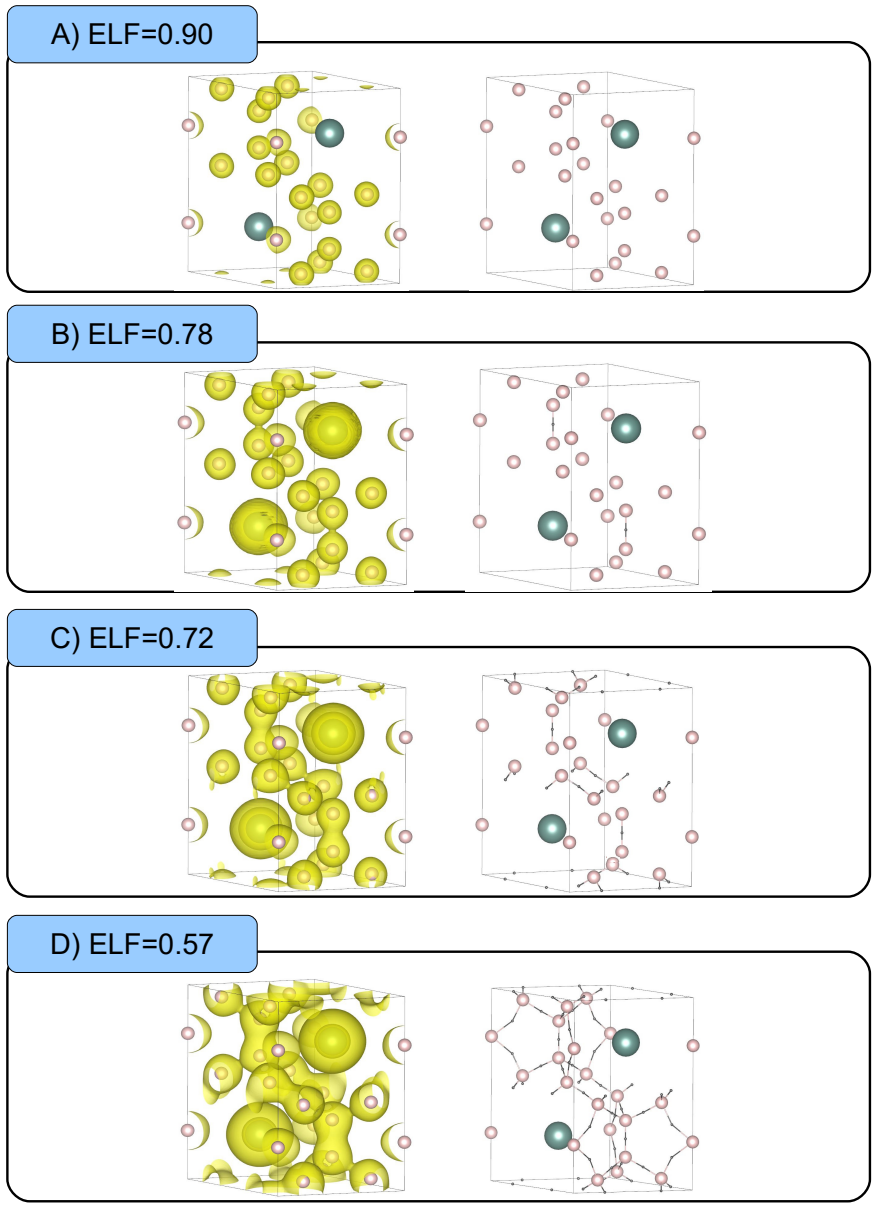

FIGURE A.3 – **Example of construction of Network 2.** The figure shows the steps for the construction of the network for YH_9 (24). On the left side the ELF isosurfaces are visualized, while on the right side the network patterns identified through the selection of the saddle points (small black dots) are visualizaed. The latter are related to the same and higher value of ELF with respect to the ELF threshold in the blue box. In step A) no bond is formed. In step B) and C) few isolated bonding patterns appear. In step D) the highest 3D network spanning through the entire cell is created. The resulting network is constructed by a subset of hydrogen atoms.

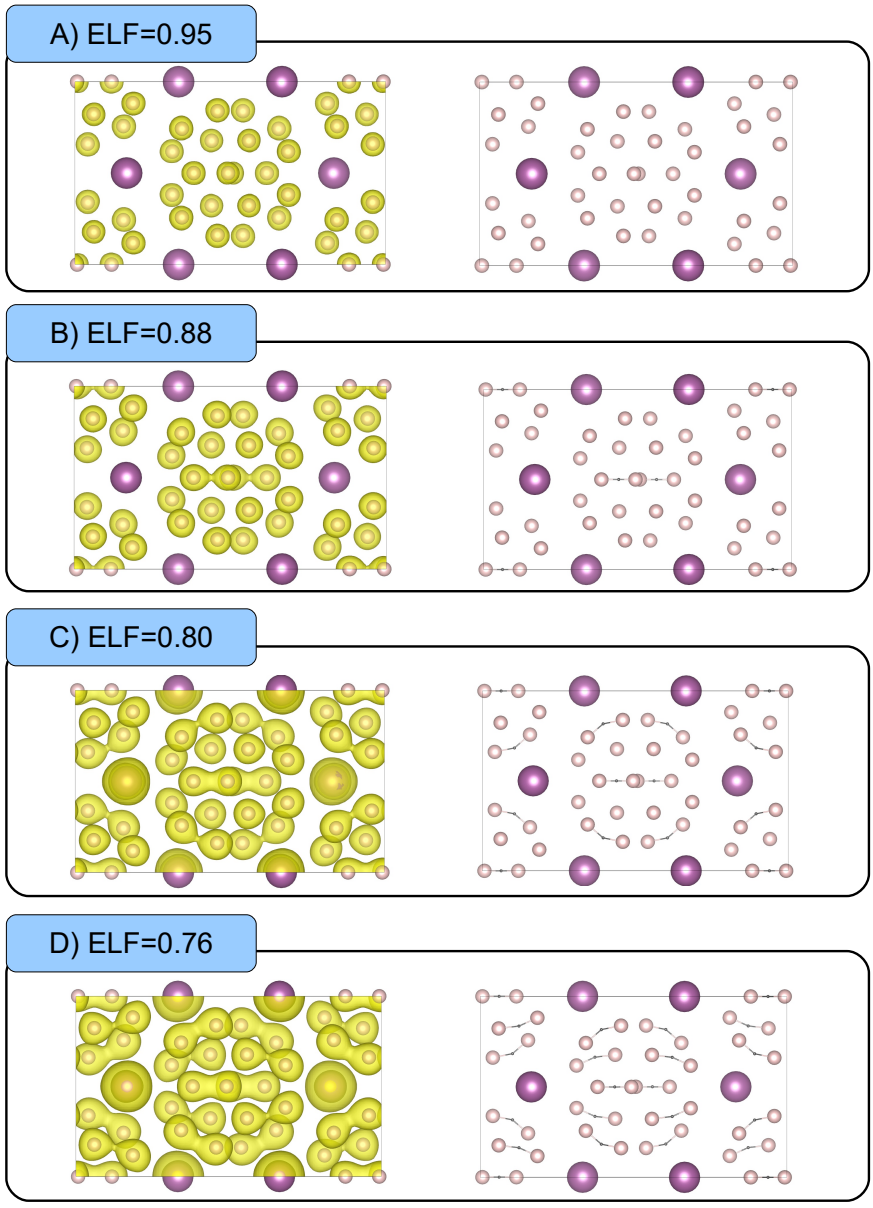
A) ELF=0.95
B) ELF=0.88
C) ELF=0.80
D) ELF=0.76

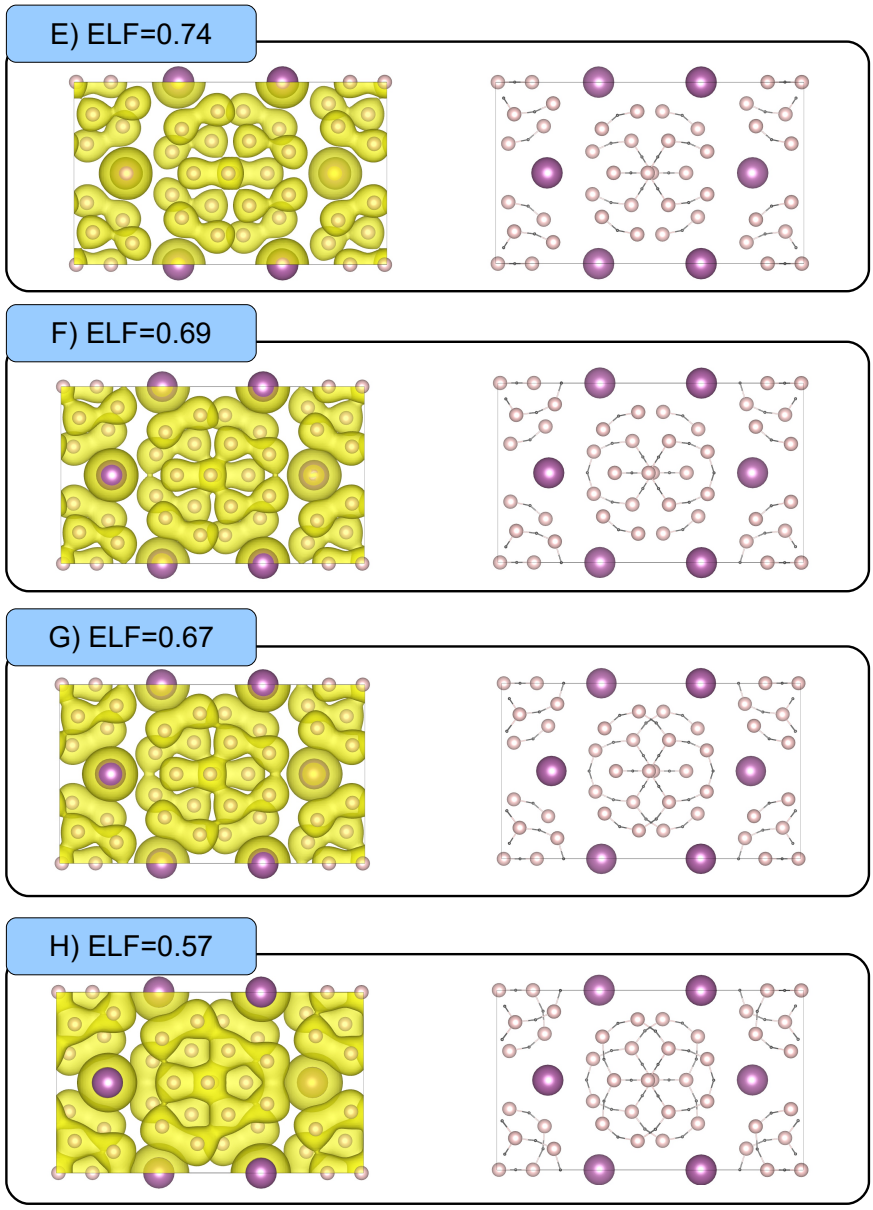
E) ELF=0.74
F) ELF=0.69
G) ELF=0.67
H) ELF=0.57

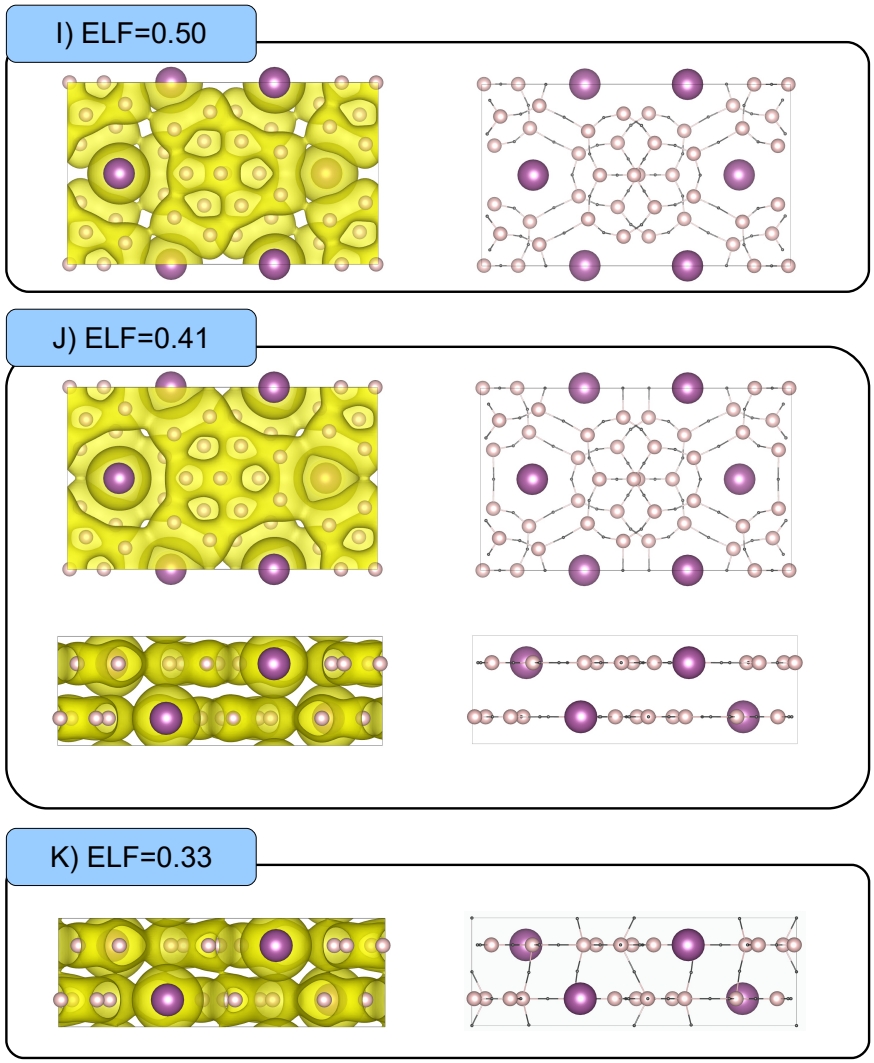

FIGURE A.4 – The figure shows the steps for the construction of the network for ScH_{10} (32). On the left side the ELF isosurfaces are visualized, while on the right side the network patterns identified through the selection of the saddle points (small black dots) are shown. The latter are related to the same and higher value of ELF with respect to the ELF threshold in the blue box. From steps A) to J) is shown the progressive formation of the interatomic bonds leading to the creation of the network. In step J) can be seen that until for ELF>0.41 the formed network is 2D. In step K) the interplane ELF connection appears creating the 3D structure necessary for the determination of the *networking value* (ϕ). The resulting network includes all the hydrogen atoms.

A.3 ScH_6-*Cmcm* PHONONS

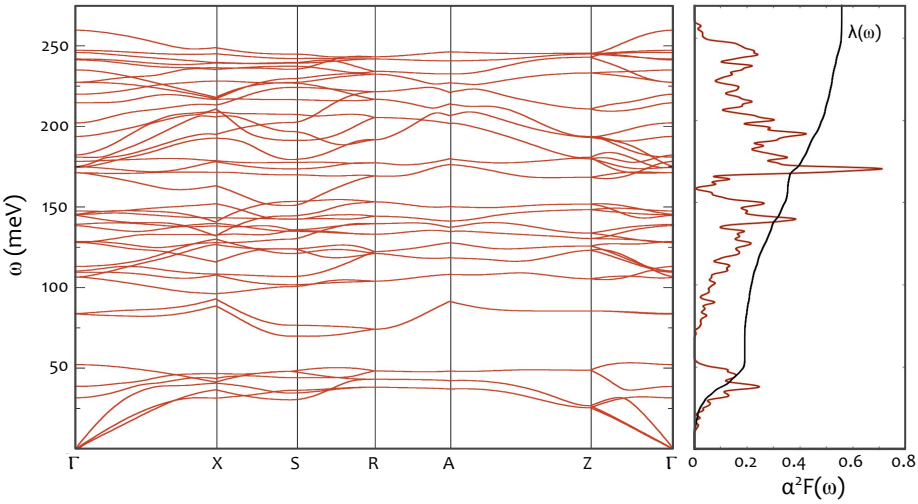

FIGURE A.5 – The figure shows the phonon spectra for the ScH_6-Cmcm phase at 100 GPa on the left, and the value of $\alpha^2F(\omega)$ and the electron phonon coupling parameter $\lambda(\omega)$ for the same pressure on the right.

Publications

The work presented here thesis was published with the following titles:

- *Impact of ionic quantum fluctuations on the thermodynamic stability and superconductivity of $LaBH_8$.*
  Francesco Belli and Ion Errea.
  Physical Review B 106 (13), 134509 (2022).

- *Quantum anharmonic enhancement of superconductivity in $P6_3/mmc$ ScH_6 at high pressures: A first-principles study.*
  Pugeng Hou, Francesco Belli, Raffaello Bianco and Ion Errea.
  Journal of Applied Physics 130 (17), 175902 (2021)

- *Strong anharmonic and quantum effects in $Pm\bar{3}m$-AlH_3 under high pressure: A first-principles study.*
  Pugeng Hou, Francesco Belli, Raffaello Bianco and Ion Errea.
  Physical Review B 103 (13), 134305 (2021)

- *Strong correlation between electronic bonding network and critical temperature in hydrogen-based superconductors.*
  Francesco Belli, Trinidad Novoa, Julia Contreras-García and Ion Errea.
  Nature communications 12 (1), 1-11 (2021)

- *Quantum crystal structure in the 250-kelvin superconducting lanthanum hydride.*
  Ion Errea, Francesco Belli, Lorenzo Monacelli, Antonio Sanna, Takashi Koretsune, Terumasa Tadano, Raffaello Bianco, Matteo Calandra, Ryotaro Arita, Francesco Mauri and José A. Flores-Livas.
  Nature 578 (7793), 66-69 (2020)

Acknowledgements

In retrospective, the past four years have been a journey I am happy to have embarked on. It has been a time full of challenges, opportunities, and changes which eventually culminated in the writing of this Thesis. In this regard, it is important to mention that the realization of this manuscript would have not been possible with me alone, but that it required the help and support of many people around me.

To start, I need to thank Ion Errea for hiring me in the Ph.D. program, and for guiding me during its course. Thanks to have had the patience to teach me, to listen my insanity and to have had the insight to mold it into actual real science. You have been an excellent supervisor and I could have not hoped for anything better.

A special thanks goes to all the members of the group. To Unai, a somewhat of a big Ph.D. brother, who helped me to kick start my Ph.D. and first taught me how to use the SSCHA. To Đorđe, Yue-Wen, Diego and Raffaello, thanks for the interesting discussions about science, and a special thanks to Josu, and Martin for the suggestions and feedback you gave me during the course of the Ph.D., and while I was writing this Thesis. A thanks goes as well to Pugeng for taking care of me and the rest of the group for the year he spent with us in San Sebastian. Finally to Antonella, a warm thank you for sharing the Ph.D. journey with me. We had a fun time and we learnt much together. I hope you too will finish soon and that everything will go well for you in the future!

It feels also important to also acknowledge José Flores Lívas for teaching me much while inspiring me with his ability of making incredible images and presentations, and as well to Julia Contreras García for her kindness and her teaching while hosting me for a short time in Paris.

Of course no real Ph.D. is such without a copious amount of coffee, and coffee break buddies. In this regard, it is important to thank Joseba for his game changer decision of acquiring a coffee machine for the office room, and for the relentless daily banter. A thanks as well to Trinidad, Stefano,

Giulia, Tomas and Mounika for being those I shared the most coffee with. You have been amazing friends during these years. I wish you all the best wherever you will be in the world in the years to come. On this note, a special thanks to Mounika who let me understand the special importance of the acknowledgements and motivated me to write this part.

On a more bureaucratic sense, a thanks goes to Ane Iturriza for helping me sort the bureaucracy during the Ph.D., and to have had the Saint rated patience to keep smiling a me, even after me not learning how to properly managing to hand in the right forms after four years. And of course, a thanks goes to the UPV/EHU, the CFM, and the European Research Council for having hosted and financed my Ph.D. Thanks as well to the computer centers of Marenostrum, Irene, and Atlas without which it would have been impossible to obtain the content of this Thesis.

A thanks goes also to Daniel Arismendi for his support, and for the good not so much smart not so much working times during the pandemic. Thanks as well to Pablo and Davide who were kind enough to stay close and help during the rough times of this last year. Things would have been much harder without you two. Furthermore, I could not forget my long time gaming buddies Kelinn, Desienna, Moonbreaker, Quynh, and Squidray. Thanks from your trusted Fel-candies dealer for have been beside me for all these years, in the real and the virtual worlds. Thanks for the banter, to have helped me through the toughest times, for the suggestions, and for all the good times.

Thanks as well to my family. Thanks for having believed in me, to have supported me and to have showed me I could accomplish this much. You are the people without which I would not be able to be where I am today. And finally, although not for importance, thanks to you, Claudia. You have been an important part of my life for all these years. Thanks for being at my side despite my flaws and thanks to have done all you could to support me, and help me grow. Thank you for your patience, your understanding, your care, and for the good and the bad times. I know you went through some rough times, but remember that, even in San Sebastian, the sun always come back to shine. I love you very much.

Bibliography

[1] BJ Xiao et al. "EAST plasma control system". In: *Fusion engineering and design* 83.2-3 (2008), pp. 181–187.

[2] Pascal Tixador et al. "Superconducting magnetic energy storage: Status and perspective". In: *IEEE/CSC & ESAS European superconductivity news forum*. Vol. 3. 2008.

[3] Hyung-Woo Lee, Ki-Chan Kim, and Ju Lee. "Review of maglev train technologies". In: *IEEE Transactions on Magnetics* 42.7 (2006), pp. 1917–1925.

[4] Frank Arute et al. "Quantum supremacy using a programmable superconducting processor". In: *Nature* 574.7779 (2019), pp. 505–510.

[5] Jay M Gambetta, Jerry M Chow, and Matthias Steffen. "Building logical qubits in a superconducting quantum computing system". In: *npj quantum information* 3.1 (2017), pp. 1–7.

[6] L. N. Cooper J. Bardeen and J. R. Schrieffer. "Theory of Superconductivity". In: *Phys. Rev.* 108 (1175 1957).

[7] J. R. Schrieffer. "Theory of Superconductivity". In: *Advanced book classics* Chapter 2 (1999), pp. 28–34.

[8] Gregor Wentzel. "Meissner effect". In: *Physical Review* 111.6 (1958), p. 1488.

[9] Heike KAMERLINGH ONNES. "The superconductivity of mercury". In: *Comm. Phys. Lab. Univ. Leiden* 122 (1911), pp. 122–124.

[10] J George Bednorz and K Alex Müller. "Possible high T_c superconductivity in the Ba-La-Cu-O system". In: *Zeitschrift für Physik B Condensed Matter* 64.2 (1986), pp. 189–193.

[11] L. N. Cooper. "Bound Electron Pairs in a Degenerate Fermi Gas". In: *Phys. Rev.* 104 (1189 1956).

[12] Jules De Launay. "The isotope effect in superconductivity". In: *Physical Review* 93.4 (1954), p. 661.

[13] E. R. Margine and F. Giustino. "Anisotropic Migdal-Eliashberg theory using Wannier functions". In: *Phys. Rev. B* 87 (024505 2013).

[14] N. W. Ashcroft. "Metallic Hydrogen: A High-Temperature Superconductor?" In: *Phys. Rev. Lett.* 21 (26 1968), pp. 1748–1749.

[15] NW Ashcroft. "Hydrogen dominant metallic alloys: high temperature superconductors?" In: *Physical Review Letters* 92.18 (2004), p. 187002.

[16] Jun Nagamatsu et al. "Superconductivity at 39 K in magnesium diboride". In: *nature* 410.6824 (2001), pp. 63–64.

[17] CE Weir et al. "Infrared studies in the 1-to 15-micron region to 30,000 atmospheres". In: *Journal of research of the National Bureau of Standards. Section A, Physics and chemistry* 63.1 (1959), p. 55.

[18] HK Mao. "High-pressure physics: sustained static generation of 1.36 to 1.72 megabars". In: *Science* 200.4346 (1978), pp. 1145–1147.

[19] José A Flores-Livas et al. "A perspective on conventional high-temperature superconductors at high pressure: Methods and materials". In: *Phys. Rep.* 856 (1 2020).

[20] Natalia Dubrovinskaia et al. "Terapascal static pressure generation with ultrahigh yield strength nanodiamond". In: *Science advances* 2.7 (2016), e1600341.

[21] Reinhard Boehler and Koen De Hantsetters. "New anvil designs in diamond-cells". In: *High Pressure Research* 24.3 (2004), pp. 391–396.

[22] AP Drozdov et al. "Conventional superconductivity at 203 kelvin at high pressures in the sulfur hydride system". In: *Nature* 525.7567 (2015), pp. 73–76.

[23] Maddury Somayazulu et al. "Evidence for superconductivity above 260 K in lanthanum superhydride at megabar pressures". In: *Physical review letters* 122.2 (2019), p. 027001.

[24] AP Drozdov et al. "Superconductivity at 250 K in lanthanum hydride under high pressures". In: *Nature* 569.7757 (2019), pp. 528–531.

[25] Richard M Martin. *Electronic structure: basic theory and practical methods*. Cambridge university press, 2020.

[26] S. Goedecker. "Minima hopping: An efficient search method for the global minimum of the potential energy surface of complex molecular systems". In: *J. Chem. Phys.* 120 (9911 2004).

[27] Maximilian Amsler and Stefan Goedecker. "Crystal structure prediction using the minima hopping method". In: *The Journal of chemical physics* 133.22 (2010), p. 224104.

[28] Colin W Glass, Artem R Oganov, and Nikolaus Hansen. "USPEX - Evolutionary crystal structure prediction". In: *Computer physics communications* 175.11-12 (2006), pp. 713–720.

[29] Chris J Pickard and RJ Needs. "Ab initio random structure searching". In: *Journal of Physics: Condensed Matter* 23.5 (2011), p. 053201.

[30] Defang Duan et al. "Pressure-induced metallization of dense $(H_2S)2H_2$ with high-T_c superconductivity". In: *Scientific reports* 4.1 (2014), pp. 1–6.

[31] Defang Duan et al. "Pressure-induced decomposition of solid hydrogen sulfide". In: *Physical Review B* 91.18 (2015), p. 180502.

[32] Hanyu Liu et al. "Potential high-T_c superconducting lanthanum and yttrium hydrides at high pressure". In: *Proceedings of the National Academy of Sciences* 114 (2017), pp. 6990–6995.

[33] Zachary M Geballe et al. "Synthesis and stability of lanthanum superhydrides". In: *Angewandte Chemie* 130.3 (2018), pp. 696–700.

[34] Feng Peng et al. "Hydrogen clathrate structures in rare earth hydrides at high pressures: possible route to room-temperature superconductivity". In: *Physical review letters* 119.10 (2017), p. 107001.

[35] Miguel Borinaga et al. "Anharmonic effects in atomic hydrogen: Superconductivity and lattice dynamical stability". In: *Phys. Rev. B* 93 (174308 2016).

[36] Christoph Heil et al. "Superconductivity in sodalite-like yttrium hydride clathrates". In: *Physical Review B* 99.22 (2019), p. 220502.

[37] Christian Kokail, Wolfgang Von Der Linden, and Lilia Boeri. "Prediction of high-T_c conventional superconductivity in the ternary lithium borohydride system". In: *Physical Review Materials* 1.7 (2017), p. 074803.

[38] Santanu Saha et al. "High-temperature conventional superconductivity in the boron-carbon system: Material trends". In: *Physical Review B* 102.2 (2020), p. 024519.

[39] Ying Sun et al. "Route to a superconducting phase above room temperature in electron-doped hydride compounds under high pressure". In: *Physical review letters* 123.9 (2019), p. 097001.

[40] Simone Di Cataldo, Wolfgang von der Linden, and Lilia Boeri. "First-principles search of hot superconductivity in La-XH ternary hydrides". In: *npj Computational Materials* 8.1 (2022), pp. 1–8.

[41] Roman Lucrezi et al. "In-silico synthesis of novel lowest-pressure high-T_c ternary superhydrides". In: *arXiv. org e-Print archive* 2112 (2021).

[42] Simone Di Cataldo et al. "$LaBH_8$: Towards high-T_c low-pressure superconductivity in ternary superhydrides". In: *Physical Review B* 104.2 (2021), p. L020511.

[43] Xiaowei Liang et al. "Prediction of high-T_c superconductivity in ternary lanthanum borohydrides". In: *Physical Review B* 104.13 (2021), p. 134501.

[44] CB Satterthwaite and IL Toepke. "Superconductivity of hydrides and deuterides of thorium". In: *Physical Review Letters* 25.11 (1970), p. 741.

[45] B. Stritzker and W. Buckel. "Superconductivity in the palladium-hydrogen and the palladium-deuterium systems". In: *Zeitschrift für Physik A Hadrons and nuclei* 257 (1972), pp. 1–8.

[46] Di Zhou et al. "Superconducting praseodymium superhydrides". In: *Science advances* 6.9 (2020), eaax6849.

[47] Igor Goncharenko et al. "Pressure-induced hydrogen-dominant metallic state in aluminum hydride". In: *Phys. Rev. Lett.* 100 (045504 2008).

[48] Panpan Kong et al. "Superconductivity up to 243 K in the yttrium-hydrogen system under high pressure". In: *Nature communications* 12.1 (2021), pp. 1–9.

[49] Ivan A Troyan et al. "Anomalous high-temperature superconductivity in YH_6". In: *Advanced Materials* 33.15 (2021), p. 2006832.

[50] Tiange Bi et al. "The search for superconductivity in high pressure hydrides". In: *arXiv preprint arXiv:1806.00163* (2018).

[51] I. Errea C. J. Pickard and M. I. Eremets. "Superconducting Hydrides Under Pressure". In: *Annu. Rev. Condens. Matter Phys.* 11 (57 2020).

[52] R. J. Needs M. J. Hutcheon A. M. Shipley. "Predicting novel superconducting hydrides using machine learning approaches". In: *Phys. Rev. B* 101 (144505 2020).

[53] K. Shimizu T. Ishikawa T. Miyake. "Materials informatics based on evolutionary algorithms: Application to search for superconducting hydrogen compounds". In: *Phys. Rev. B* 100 (174506 2019).

[54] Valentin Stanev et al. "Machine learning modeling of superconducting critical temperature". In: *npj Comput. Mater* 4 (29 2018).

[55] Santanu Saha et al. "Mapping Superconductivity in High-Pressure Hydrides: The *Superhydra* Project". In: *arXiv preprint arXiv:2205.02554* (2022).

[56] Dmitrii V Semenok et al. "On distribution of superconductivity in metal hydrides". In: *Current Opinion in Solid State and Materials Science* 24.2 (2020), p. 100808.

[57] AF Goncharov et al. "Compression of ice to 210 gigapascals: Infrared evidence for a symmetric hydrogen-bonded phase". In: *Science* 273.5272 (1996), pp. 218–220.

[58] Paul Loubeyre et al. "Modulated phases and proton centring in ice observed by X-ray diffraction up to 170 GPa". In: *Nature* 397.6719 (1999), pp. 503–506.

[59] Magali Benoit, Dominik Marx, and Michele Parrinello. "Tunnelling and zero-point motion in high-pressure ice". In: *Nature* 392.6673 (1998), pp. 258–261.

[60] Ion Errea, Matteo Calandra, and Francesco Mauri. "First-principles theory of anharmonicity and the inverse isotope effect in superconducting palladium-hydride compounds". In: *Phys. Rev. Lett.* 111 (177002 2013).

[61] Ion Errea, Matteo Calandra, and Francesco Mauri. "Anharmonic free energies and phonon dispersions from the stochastic self-consistent harmonic approximation: Application to platinum and palladium hydrides". In: *Physical Review B* 89.6 (2014), p. 064302.

[62] Lorenzo Monacelli et al. "The stochastic self-consistent harmonic approximation: calculating vibrational properties of materials with full quantum and anharmonic effects". In: *J. Phys. Cond. Matt.* 33 (363001 2021).

[63] Raffaello Bianco et al. "Second-order structural phase transition, free energy curvature, and temperature-dependent anharmonic phonons in the self-consistent harmonic approximation: theory and stochastic implementation". In: *Phys. Rev. V* 96 (014111 2017).

[64] Lorenzo Monacelli et al. "Pressure and stress tensor of complex anharmonic crystals within the stochastic self-consistent harmonic approximation". In: *Physical Review B* 98.2 (2018), p. 024106.

[65] R. Oppenheimer M. Born. "Quantum theory of the molecules". In: *Ann. d. Physik* 84 (1927), pp. 457–484.

[66] K. Huang M. Born. "Dynamic theory of crystal lattices". In: *Oxford University Press* (1954).

[67] Yu.M. Kagan E.G. Brovman. "Phonons in non-transition metals". In: *Dynamical Properties of Solids* Vol 1 (1974), pp. 191–301.

[68] Richard M. Martin. "Electronic structure: Basic theory and practical methods". In: *Cambridge University Press* Chapter 6 (2004), p. 122.

[69] D. M. Ceperley and B. J. Alder. "Ground state of the electron gas by a stochastic method". In: *1980* 45 (566).

[70] John P. Perdew. "Accurate Density Functional for the Energy: Real-Space Cutoff of the Gradient Expansion for the Exchange Hole". In: *Phys. Rev. Lett.* 55 (1665 1985).

[71] Larry A. Curtiss. "Assessment of Gaussian-2 and density functional theories for the computation of enthalpies of formation". In: *J. Chem. Phys.* 106 (1063 1997).

[72] Timothy J. Giese and Darrin M. Yorka. "Density-functional expansion methods: Evaluation of LDA, GGA, and meta-GGA functionals and different integral approximations". In: *J Chem Phys.* 133 (244107 2010).

[73] Pedro Borlido et al. "Exchange-correlation functionals for band gaps of solids: benchmark, reparametrization and machine learning". In: *npj Computational Materials* 6.1 (2020), pp. 1–17.

[74] C. Chiang D. A. Hamann M. Shchlüter. "Norm-conserving pseudopotentials". In: *Phys. Rev. Lett.* 43 (1979), pp. 1494–1497.

[75] P.E Bloöch. "Generalized separable potentials for electronic-structure calculations". In: *Phys. Rev. B* 41 (1990), pp. 5414–5416.

[76] D. Vanderbilt. "Soft self-consistent pseudopotentials in a generalized eigenvalue formalism". In: *Phys. Rev. B* 41 (7892 1990).

[77] P.E Bloöch. "Projector augmented-wave method". In: *Phys. Rev. B* 50 (1994), pp. 17953–17979.

[78] D. Joubert G. Kresse. "From ultrasoft pseudopotentials to the projector augmented-wave method". In: *Phys. Rev. B* 59 (1999), pp. 1758–1775.

[79] NAW Holzwarth et al. "Comparison of the projector augmented-wave, pseudopotential and linearized augmented-plane-wave formalism for density.functional calculations of solids". In: *Phys. Rev. B* 55 (1997), pp. 2005–2017.

[80] Hendrik J Monkhorst and James D Pack. "Special points for Brillouin-zone integrations". In: *Physical review B* 13.12 (1976), p. 5188.

[81] MPAT Methfessel and AT Paxton. "High-precision sampling for Brillouin-zone integration in metals". In: *Physical Review B* 40.6 (1989), p. 3616.

[82] W. H. Freeman. "Notes on General Chemistry (2nd ed.), Chapter 3.5, Many-electron atoms: Fermi holes and Fermi heaps." In: *Dan Dill* (Chapter 3.5 2006).

[83] A. D. Becke. "Hartree-Fock Exchange Energy of an Inhomogeneous Electron Gas". In: *Int. J. of Q. Chem.* 23 (1983), pp. 1915–1922.

[84] A. D. Becke. "Local exchage-correalation approximations and first-row molecular dissociation energies". In: *Int. J. of Q Chem.* 27 (1985), pp. 585–594.

[85] Andreas Savin et al. "ELF: The electron localization function". In: *Angewandte Chemie International Edition in English* 36.17 (1997), pp. 1808–1832.

[86] F. Giustino. "Electron-phonon interactions from first principles". In: *Rev. Mod. Phys.* 89 (015003 2017).

[87] B.Monserrat J. H. Lloyd-Williams. "Lattice dynamics and electron-phonon coupling calculations using nondiagonal supercells". In: *Phys. Rev. B* 92 (184301 2015).

[88] Richard M. Martin. "Electronic structure: Basic theory and practical methods". In: *Cambridge University Press* Chapter 19 (2004), pp. 394–399.

[89] Stefano Baroni et al. "Phonons and related crystal properties from density-functional perturbation theory". In: *Rev. Mod. Phys.* 73 (2001), pp. 515–562.

[90] G. J. Ackland I. B. Magdau. "Identification of high pressure phases III and IV in hydrogen: simulating Raman spectra using molecular dynamics". In: *Rev. Rev. B* 87 (174110 2013).

[91] O. M. Ceperley. "Path integrals in the theory of condensed helium". In: *Rev. Mod. Phys.* 867 (1995), pp. 279–355.

[92] Raffaello Bianco et al. "High-pressure phase diagram of hydrogen and deuterium sulfides from first principles: Structural and vibrational properties including quantum and anharmonic effects". In: *Physical Review B* 97.21 (2018), p. 214101.

[93] Gabriele Giuliani and Giovanni Vignale. *Quantum theory of the electron liquid*. Cambridge university press, 2005.

[94] Felix Bloch. "Über die quantenmechanik der elektronen in kristallgittern". In: *Zeitschrift für physik* 52.7 (1929), pp. 555–600.

[95] Herbert Fröhlich, Hans Pelzer, and Sigurd Zienau. "XX. Properties of slow electrons in polar materials". In: *The London, Edinburgh, and Dublin Philosophical Magazine and Journal of Science* 41.314 (1950), pp. 221–242.

[96] W. L. McMillan. "Transition Temperature of Strong-Coupled Superconductors". In: *Phys. Rev.* 167 (1968), pp. 331–344.

[97] R. Dynes. "McMillan's equation and the Tc of superconductors". In: *Solid State Comm.* 10 (1972), pp. 615–618.

[98] R. C. Dynes P. B. Allen. "Transition temperature of strong-coupled superconductors reanalyzed". In: *Phys. Rev. B* 12 (1975), pp. 905–922.

[99] Tiange Bi et al. "The Search for Superconductivity in High Pressure Hydrides". In: *Reference Module in Chemistry, Molecular Sciences and Chemical Engineering*. Elsevier, 2019.

[100] Yu Xie et al. "Superconductivity of lithium-doped hydrogen under high pressure". In: *Acta Crystallographica Section C* 70 (2014), pp. 104–111.

[101] Dawei Zhou et al. "Ab initio study revealing a layered structure in hydrogen-rich KH_6 under high pressure". In: *Phys. Rev. B* 86 (014118 2012).

[102] Shuyin Yu et al. "Exploration of stable compounds, crystal structures, and superconductivity in the Be-H system". In: *AIP Advances* 4 (107118 2014).

[103] Xiaolei Feng et al. "Compressed sodalite-like MgH_6 as a potential high-temperature superconductor". In: *RSC Adv.* 5 (2015), pp. 59292–59296.

[104] Hui Wang et al. "Superconductive sodalite-like clathrate calcium hydride at high pressures". In: *Proceedings of the National Academy of Sciences* (2012), pp. 6463–6466.

[105] Yanchao Wang et al. "Structural morphologies of high-pressure polymorphs of strontium hydrides". In: *Phys. Chem. Chem. Phys.* 17 (2015), pp. 19379–19385.

[106] James Hooper et al. "Polyhydrides of the alkaline earth metals: A look at the extremes under pressure". In: *The Journal of Physical Chemistry C* 117 (2013), pp. 2982–2992.

[107] Duck Young Kim et al. "General trend for pressurized superconducting hydrogen-dense materials". In: *Proceedings of the National Academy of Sciences* 107 (2010), pp. 2793–2796.

[108] Yong-Kai Wei et al. "Pressure induced superconductivity and electronic structure properties of scandium hydrides using first principles calculations". In: *RSC Adv.* 6 (2016), pp. 81534–81541.

[109] Yinwei Li et al. "Pressure-stabilized superconductive yttrium hydrides". In: *Scientific Reports* 5 (9948 2015).

[110] Shifeng Qian et al. "Theoretical study of stability and superconductivity of ScH_n ($n = 4 - 8$) at high pressure". In: *Phys. Rev. B* 96 (094513 2017).

[111] Xiaoqiu Ye et al. "High hydrides of scandium under pressure: potential superconductors". In: *J. Phys. Chem. C* 122 (2018), pp. 6298–6309.

[112] Bin Li et al. "Predicted high-temperature superconductivity in cerium hydrides at high pressures". In: *Journal of Applied Physics* 126 (235901 2019).

[113] IO Bashkin et al. "Superconductivity in the Ti-d system under pressure". In: *Physics of the Solid State* 40 (1998), pp. 1950–1952.

[114] Kavungal Veedu Shanavas, L Lindsay, and David S Parker. "Electronic structure and electron-phonon coupling in TiH_2". In: *Scientific Reports* 6 (28102 2016).

[115] Xiao-Feng Li, Zi-Yu Hu, and Bing Huang. "Phase diagram and superconductivity of compressed zirconium hydrides". In: *Phys. Chem. Chem. Phys.* 19 (2017), pp. 3538–3543.

[116] Yunxian Liu et al. "First-principles study on the structural and electronic properties of metallic HfH_2 under pressure". In: *Scientific Reports* 5 (11381 2015).

[117] Changbo Chen et al. "Pressure induced phase transition in MH_2 (M = V, Nb)". In: *J. Chem. Phys* 140 (114703 2014).

[118] Guoying Gao et al. "Theoretical study of the ground-state structures and properties of niobium hydrides under pressure". In: *Phys. Rev. B* 88 (184104 2013).

[119] Quan Zhuang et al. "Pressure-stabilized superconductive ionic tantalum hydrides". In: *Inorganic chemistry* 56 (2017), pp. 3901–3908.

[120] Shuyin Yu et al. "Pressure-driven formation and stabilization of superconductive chromium hydrides". In: *Scientific Reports* 5 (17764 2015).

[121] Xiaofeng Li, Hanyu Liu, and Feng Peng. "Crystal structures and superconductivity of technetium hydrides under pressure". In: *Phys. Chem. Chem. Phys.* 18 (2016), pp. 28791–28796.

[122] Alexander G Kvashnin et al. "Iron superhydrides FeH_5 and FeH_6: stability, electronic properties, and superconductivity". In: *J. Phys. Chem. C* 122 (2018), pp. 4731–4736.

[123] Arnab Majumdar et al. "Superconductivity in FeH_5". In: *Phys. Rev. B* 96 (201107 2017).

[124] Yunxian Liu et al. "Stability and properties of the Ru-H system at high pressure". In: *Phys. Chem. Chem. Phys.* 18 (2016), pp. 1516–1520.

[125] Yunxian Liu et al. "Structures and properties of osmium hydrides under pressure from first principle calculation". In: *J. Phys. Chem. C* 119 (2015), pp. 15905–15911.

[126] Liyuan Wang et al. "High-pressure formation of cobalt polyhydrides: A first-principle study". In: *Inorganic Chemistry* 57 (2018), pp. 181–186.

[127] Chao-Hao Hu et al. "Pressure-induced stabilization and insulator-superconductor transition of BH". In: *Phys. Rev. Lett.* 110 (165504 2013).

[128] Kazutaka Abe and N.W. Ashcroft. "Crystalline diborane at high pressures". In: *Phys. Rev. B* 84 (104118 2011).

[129] Yong-Kai Wei et al. "Elastic, superconducting, and thermodynamic properties of the cubic metallic phase of AlH_3 via first-principles calculations". In: *Journal of Applied Physics* 114 (114905 2013).

[130] Pugeng Hou et al. "High pressure structures and superconductivity of $AlH_3(H_2)$ predicted by first principles". In: *RSC advances* 5.7 (2015), pp. 5096–5101.

[131] Guoying Gao et al. "Metallic and superconducting gallane under high pressure". In: *Physical Review B* 84.6 (2011), p. 064118.

[132] Yunxian Liu et al. "Pressure-induced structures and properties in indium hydrides". In: *Inorganic chemistry* 54.20 (2015), pp. 9924–9928.

[133] Y Yao et al. "Superconductivity in high-pressure SiH_4". In: *EPL (Europhysics Letters)* 78.3 (2007), p. 37003.

[134] JS Tse, Y Yao, and K Tanaka. "Novel superconductivity in metallic SnH_4 under high pressure". In: *Physical Review Letters* 98.11 (2007), p. 117004.

[135] Ji Feng et al. "Structures and potential superconductivity in SiH_4 at high pressure: En route to "metallic hydrogen"". In: *Physical Review Letters* 96.1 (2006), p. 017006.

[136] Huadi Zhang et al. "High-temperature superconductivity in compressed solid silane". In: *Scientific reports* 5.1 (2015), pp. 1–7.

[137] Xiao-Jia Chen et al. "Superconducting behavior in compressed solid SiH_4 with a layered structure". In: *Physical review letters* 101.7 (2008), p. 077002.

[138] Miguel Martinez-Canales et al. "Novel structures and superconductivity of silane under pressure". In: *Physical review letters* 102.8 (2009), p. 087005.

[139] Yinwei Li et al. "Superconductivity at 100 K in dense $SiH_4(H_2)2$ predicted by first principles". In: *Proceedings of the National Academy of Sciences* 107.36 (2010), pp. 15708–15711.

[140] Xilian Jin et al. "Superconducting high-pressure phases of disilane". In: *Proceedings of the National Academy of Sciences* 107.22 (2010), pp. 9969–9973.

[141] José A Flores-Livas et al. "High-pressure structures of disilane and their superconducting properties". In: *Physical review letters* 108.11 (2012), p. 117004.

[142] Guoying Gao et al. "Superconducting high pressure phase of germane". In: *Physical review letters* 101.10 (2008), p. 107002.

[143] Chao Zhang et al. "Superconductivity in hydrogen-rich material: GeH_4". In: *Journal of superconductivity and novel magnetism* 23.5 (2010), pp. 717–719.

[144] Huadi Zhang et al. "Investigation of stable germane structures under high-pressure". In: *Physical Chemistry Chemical Physics* 17.41 (2015), pp. 27630–27635.

[145] Guohua Zhong et al. "Structural, electronic, dynamical, and superconducting properties in dense $GeH_4(H_2)2$". In: *The Journal of Physical Chemistry C* 116.8 (2012), pp. 5225–5234.

[146] PuGeng Hou et al. "Ab initio study of germanium-hydride compounds under high pressure". In: *RSC advances* 5.25 (2015), pp. 19432–19438.

[147] M Mahdi Davari Esfahani et al. "Superconductivity and unexpected chemistry of germanium hydrides under pressure". In: *Physical Review B* 95.13 (2017), p. 134506.

[148] Kazutaka Abe and NW Ashcroft. "Quantum disproportionation: The high hydrides at elevated pressures". In: *Physical Review B* 88.17 (2013), p. 174110.

[149] Huadi Zhang et al. "A novel stable hydrogen-rich SnH_8 under high pressure". In: *RSC advances* 5.130 (2015), pp. 107637–107641.

[150] Guoying Gao et al. "High-pressure crystal structures and superconductivity of Stannane (SnH_4)". In: *Proceedings of the National Academy of Sciences* 107.4 (2010), pp. 1317–1320.

[151] JS Tse, Y Yao, and K Tanaka. "Novel superconductivity in metallic SnH_4 under high pressure". In: *Physical Review Letters* 98.11 (2007), p. 117004.

[152] Huadi Zhang et al. "Pressure-induced phase transition of SnH_4: a new layered structure". In: *RSC advances* 6.13 (2016), pp. 10456–10461.

[153] M Mahdi Davari Esfahani et al. "Superconductivity of novel tin hydrides (Sn_nH_m) under pressure". In: *Scientific reports* 6.1 (2016), pp. 1–7.

[154] José A Flores-Livas et al. "Superconductivity in metastable phases of phosphorus-hydride compounds under high pressure". In: *Physical Review B* 93.2 (2016), p. 020508.

[155] Hanyu Liu et al. "Crystal structure and superconductivity of PH_3 at high pressures". In: *The Journal of Physical Chemistry C* 120.6 (2016), pp. 3458–3461.

[156] Tiange Bi et al. "Superconducting phases of phosphorus hydride under pressure: stabilization by mobile molecular hydrogen". In: *Angewandte Chemie* 129.34 (2017), pp. 10326–10329.

[157] Tiange Bi et al. "Superconducting phases of phosphorus hydride under pressure: stabilization by mobile molecular hydrogen". In: *Angewandte Chemie* 129.34 (2017), pp. 10326–10329.

[158] Yuhao Fu et al. "High-pressure phase stability and superconductivity of pnictogen hydrides and chemical trends for compressed hydrides". In: *Chemistry of Materials* 28.6 (2016), pp. 1746–1755.

[159] Kazutaka Abe and NW Ashcroft. "Stabilization and highly metallic properties of heavy group-V hydrides at high pressures". In: *Physical Review B* 92.22 (2015), p. 224109.

[160] Yinwei Li et al. "The metallization and superconductivity of dense hydrogen sulfide". In: *The Journal of chemical physics* 140.17 (2014), p. 174712.

[161] Ion Errea et al. "Quantum hydrogen-bond symmetrization in the superconducting hydrogen sulfide system". In: *Nature* 532.7597 (2016), pp. 81–84.

[162] Ryosuke Akashi et al. "First-principles study of the pressure and crystal-structure dependences of the superconducting transition temperature in compressed sulfur hydrides". In: *Physical Review B* 91.22 (2015), p. 224513.

[163] Yinwei Li et al. "Dissociation products and structures of solid H_2S at strong compression". In: *Physical Review B* 93.2 (2016), p. 020103.

[164] Takahiro Ishikawa et al. "Superconducting H_5S_2 phase in sulfur-hydrogen system under high-pressure". In: *Scientific reports* 6.1 (2016), pp. 1–8.

[165] José A Flores-Livas, Antonio Sanna, and EKU Gross. "High temperature superconductivity in sulfur and selenium hydrides at high pressure". In: *The European Physical Journal B* 89.3 (2016), pp. 1–6.

[166] Yanfeng Ge, Fan Zhang, and Yugui Yao. "First-principles demonstration of superconductivity at 280 K in hydrogen sulfide with low phosphorus substitution". In: *Physical Review B* 93.22 (2016), p. 224513.

[167] Shoutao Zhang et al. "Phase diagram and high-temperature superconductivity of compressed selenium hydrides". In: *Scientific reports* 5.1 (2015), pp. 1–8.

[168] Xin Zhong et al. "Tellurium hydrides at high pressures: High-temperature superconductors". In: *Physical review letters* 116.5 (2016), p. 057002.

[169] Yunxian Liu et al. "Prediction of stoichiometric poh n compounds: crystal structures and properties". In: *RSC advances* 5.125 (2015), pp. 103445–103450.

[170] Defang Duan et al. "Hydrogen bond symmetrization and superconducting phase of HBr and HCl under high pressure: An ab initio study". In: *The Journal of chemical physics* 133.7 (2010), p. 074509.

[171] Siyu Lu et al. "Prediction of novel crystal structures and superconductivity of compressed HBr". In: *RSC Advances* 5.57 (2015), pp. 45812–45816.

[172] Changbo Chen et al. "Novel superconducting phases of HCl and HBr under high pressure: an ab initio study". In: *The Journal of Physical Chemistry C* 119.30 (2015), pp. 17039–17043.

[173] Andrew Shamp and Eva Zurek. "Superconducting high-pressure phases composed of hydrogen and iodine". In: *The journal of physical chemistry letters* 6.20 (2015), pp. 4067–4072.

[174] Defang Duan et al. "Enhancement of T_c in the atomic phase of iodine-doped hydrogen at high pressures". In: *Physical Chemistry Chemical Physics* 17.48 (2015), pp. 32335–32340.

[175] Xiaozhen Yan et al. "Structure, stability, and superconductivity of new Xe–H compounds under high pressure". In: *The Journal of chemical physics* 143.12 (2015), p. 124310.

[176] David C Lonie et al. "Metallization of magnesium polyhydrides under pressure". In: *Physical Review B* 87.5 (2013), p. 054107.

[177] José A Flores-Livas et al. "Superconductivity in metastable phases of phosphorus-hydride compounds under high pressure". In: *Physical Review B* 93.2 (2016), p. 020508.

[178] Andrew Shamp et al. "Decomposition products of phosphine under pressure: PH_2 stable and superconducting?" In: *Journal of the American Chemical Society* 138.6 (2016), pp. 1884–1892.

[179] Miguel Borinaga et al. "Anharmonic enhancement of superconductivity in metallic molecular $Cmca\bar{4}$ hydrogen at high pressure: a first-principles study". In: *Journal of Physics: Condensed Matter* 28.49 (2016), p. 494001.

[180] Paolo Giannozzi et al. "QUANTUM ESPRESSO: a modular and open-source software project for quantum simulations of materials". In: *Journal of physics: Condensed matter* 21.39 (2009), p. 395502.

[181] Paolo Giannozzi et al. "Advanced capabilities for materials modelling with Quantum ESPRESSO". In: *Journal of physics: Condensed matter* 29.46 (2017), p. 465901.

[182] John P Perdew, Kieron Burke, and Matthias Ernzerhof. "Generalized gradient approximation made simple". In: *Physical review letters* 77.18 (1996), p. 3865.

[183] R. F. W. Bader. "Atoms in Molecules: A Quantum Theory". In: *Oxford University Press* (1990).

[184] Shichang Yao et al. "Formation mechanism of chemically precompressed hydrogen clathrates in metal superhydrides". In: *Inorganic Chemistry* 60.17 (2021), pp. 12934–12940.

[185] Seho Yi et al. "Stability and bonding nature of clathrate H cages in a near-room-temperature superconductor LaH_10". In: *Physical Review Materials* 5.2 (2021), p. 024801.

[186] Martin Rahm et al. "Squeezing all elements in the periodic table: electron configuration and electronegativity of the atoms under compression". In: *Journal of the American Chemical Society* 141.26 (2019), pp. 10253–10271.

[187] Hui Wang et al. "Hydrogen-rich superconductors at high pressures". In: *Wiley Interdisciplinary Reviews: Computational Molecular Science* 8.1 (2018), e1330.

[188] Lilia Boeri. "Understanding novel superconductors with ab initio calculations". In: *Handbook of Materials Modeling: Applications: Current and Emerging Materials* (2020), pp. 73–112.

[189] Mehmet Dogan, Sehoon Oh, and Marvin L Cohen. "High temperature superconductivity in the candidate phases of solid hydrogen". In: *Journal of Physics: Condensed Matter* 34.15 (2022), 15LT01.

[190] Feliciano Giustino, Marvin L Cohen, and Steven G Louie. "Electron-phonon interaction using Wannier functions". In: *Physical Review B* 76.16 (2007), p. 165108.

[191] Ion Errea et al. "Quantum crystal structure in the 250 kelvin superconducting lanthanum hydride". In: *Nature* 578.7793 (2020), pp. 66–69.

[192] Dan Sun et al. "High-temperature superconductivity on the verge of a structural instability in lanthanum superhydride". In: *Nature Communications* 12.1 (2021), pp. 1–7.

[193] Hanyu Liu et al. "Dynamics and superconductivity in compressed lanthanum superhydride". In: *Physical Review B* 98.10 (2018), p. 100102.

[194] Magali Benoit, Dominik Marx, and Michele Parrinello. "Tunnelling and zero-point motion in high-pressure ice". In: *Nature* 392.6673 (1998), pp. 258–261.

[195] Hanyu Liu et al. "Crystal structure and superconductivity of PH3 at high pressures". In: *The Journal of Physical Chemistry C* 120.6 (2016), pp. 3458–3461.

[196] Axel D Becke and Kenneth E Edgecombe. "A simple measure of electron localization in atomic and molecular systems". In: *The Journal of chemical physics* 92.9 (1990), pp. 5397–5403.

[197] Gernot Frenking and Sason Shaik. *The chemical bond: fundamental aspects of chemical bonding*. John Wiley & Sons, 2014.

[198] Pugeng Hou et al. "Quantum anharmonic enhancement of superconductivity in $P6_3/mmc$ ScH6 at high pressures: A first-principles study". In: *Journal of Applied Physics* 130.17 (2021), p. 175902.

[199] Ion Errea et al. "High-pressure hydrogen sulfide from first principles: A strongly anharmonic phonon-mediated superconductor". In: *Physical review letters* 114.15 (2015), p. 157004.

[200] AP Drozdov, MI Eremets, and IA Troyan. "Superconductivity above 100 K in PH3 at high pressures". In: *arXiv preprint arXiv: 1508.06224* (2015).

[201] Yanbin Ma et al. "High-pressure structures and superconductivity of bismuth hydrides". In: *arXiv preprint arXiv:1511.05291* (2015).

[202] Defang Duan et al. "Decomposition of solid hydrogen bromide at high pressure". In: *arXiv preprint arXiv:1504.01196* (2015).